The University of Osaka
Institutional Knowledge Archive

Title	Mission Design, Orbit Deployment, and Imaging Control of Satellite Constellation for Earth Observation
Author(s)	井本, 悠太
Citation	大阪大学, 2025, 博士論文
Version Type	VoR
URL	https://doi.org/10.18910/101639
rights	
Note	

The University of Osaka Institutional Knowledge Archive : OUKA

https://ir.library.osaka-u.ac.jp/

The University of Osaka

Doctoral Dissertation

Mission Design, Orbit Deployment, and Imaging Control of Satellite Constellation for Earth Observation

Yuta Imoto

January 2025

Graduate School of Engineering
Osaka University

Contents

Nomenclature

a : Semi-major axis
e : Eccentricity
i : Inclination
Ω : Right ascension of ascending node (RAAN)
ω : Argument of perigee
f : True anomaly
M Mean anomaly
$\mathcal{F}_B$: Satellite body frame
$\mathcal{F}_I$: Earth centered inertial frame
$\mathcal{F}_E$: Earth centered rotating frame
h_{sat} Satellite altitude
$\boldsymbol{J}$: Satellite inertia tensor
J_2 Coefficient describing Earth's oblateness
R_E : Mean equatorial radius of the Earth
$\boldsymbol{r}_s$: Satellite position vector in $\mathcal{F}_I$
β : CMG skew angle
θ_k : Gimbal angle of kth CMG
$\dot{\theta}_{\max}$: Maximum gimbal rate
$\ddot{\theta}_{\max}$: Maximum gimbal acceleration
μ Gravitational parameter of the Earth
ω_e Earth's angular velocity of rotation
$\boldsymbol{\omega}_s$: Satellite angular velocity

Vector $\boldsymbol{v}$ in coordinate $\mathcal{F}_X$ $(X \in \{I, E, B\})$ is expressed as $[\boldsymbol{v}]_X$. Let $\theta = f + \omega$ be an argument of latitude. In addition, the following variables are set:

$$n = \sqrt{\frac{\mu}{a^3}},$$

$$\eta = \sqrt{1 - e^2},$$

$$p = a(1 - e^2).$$

Chapter 1

Introduction

1.1 Satellite constellation: achievement of sustainable Earth management system

Today, satellite systems support society in a wide variety of ways. Stable Internet access provided by satellites is the basis for economic activity and social infrastructure. In addition, an Earth observation system that can quickly and accurately collect information on a global scale is required to acquire information and rescue people in case of a disaster. Moreover, the improvement of information gathering and monitoring capabilities is also an important issue today. Satellite systems can contribute to this point. Using satellite systems, real-time monitoring activities can be achieved. This will enable the reinforcement of national defense capabilities and counterterrorism measures. As the above examples show, it is not too much to say that today's society is made up of satellite systems.

To achieve sustainable Earth management systems, there are some problems with single-satellite missions. The first one is mission continuity. It is difficult to continuously monitor the target with one satellite, especially when placed in low Earth orbit. For observation or communication missions, this problem is critical. The second one is the satellite coverage. It is difficult for a single satellite to observe the entire Earth. Therefore, there are places where information cannot be obtained, or communication services cannot be provided. The third problem is real-time performance. For example, consider a situation in which one satellite is doing an observation mission in low Earth orbit. Suppose a disaster occurs in Japan when a satellite is flying over Brazil. In that case, it takes more than 40 minutes for the satellite to pass over Japan and start observation and sending data. This example shows that a single satellite system cannot provide the necessary information quickly in an emergency like a natural disaster.

To get over these problems, satellite constellations are becoming more and more popular today. They are large-scale systems with multiple satellites. Recent technological developments have made satellites smaller, lighter, and less expensive. Accordingly, space missions are shifting from missions with a single large satellite to large-scale constellations with multiple small satellites [1]. If the orbit of each satellite and the number of them are appropriately set, global coverage, where the entire Earth is always covered, can be achieved. Then, in the case of communication missions, a continuous internet connection can be obtained. Also, observation missions can be conducted immediately in an emergency, and necessary support can be provided quickly. One example is Planet Labs's Flock constellation [2]. This constellation achieves global coverage of the entire Earth with many small 3U-sized satellites. In addition to mission continuity, satellite coverage, and real-time performance, satellite constellations also have benefits in terms of system reliability. In the case of a single satellite mission, the mission stops when the satellite fails. On the contrary, in the case of a satellite constellation, other satellites can support the mission of a failed satellite. Therefore, satellite constellations can improve the reliability of the whole system. They ensure data reliability and enable stable missions over the long term. Like this, the use of the satellite constellation can achieve sustainable Earth management systems.

1.2 Research background

1.2.1 Optimal constellation design

In Earth observation missions, the most significant benefit of using satellite constellations is to improve the frequency of revisiting and observation opportunities. It enables us to make observations more frequently, collect information quickly in an emergency with observation satellites, and continuously provide internet services and position information with communication satellites. However, in the orbit determination of satellite constellations, we must consider not only multiple design parameters for multiple satellites but also some factors peculiar to satellite constellations, for example, revisit time, nadir tracking, and global coverage [3]. Therefore, a new orbit design method for satellite constellations is needed.

In previous studies of satellite constellation determination, there have been studies that analyzed satellite revisit time and distribution from geometrical configurations of satellite constellations [4, 5], and studies evaluated the revisit frequency and the imageable range of satellite constellations from the shape of satellite nadir trajectories (ground tracks) [6, 7]. In addition, Ge [8] obtained a navigation satellite constellation in low Earth orbit (LEO) from Precise Point Positioning (PPP) analysis, and Huang [9] proposed an optimal LEO and medium Earth orbit (MEO) constellation determination method that achieves global coverage for communication and positioning satellites. To simplify design problems, many of these constellation design methods evaluate mission performance with a relatively simple coverage shape, for example, round or rectangle. These geometrically simple coverage evaluations are helpful for communication and positioning missions. Therefore, many previous researches on satellite constellations [10, 11] mainly focus on these missions.

As for the Earth observation satellite constellation, Li [12] proposed a constellation design and evaluation method for Earth observation satellites, and Chao [13] proposed an optimal constellation design method using multi-step optimization. In addition, Razoumny [14, 15, 16, 17, 18] proposed the route theory method for designing the optimal satellite constellation. Route theory describes the constellation design problem in analytical form by mathematically modeling the satellite coverage. This method has the advantage of achieving the optimal design for an arbitrary satellite constellation. From these studies, it can be said that the optimal constellation design method for general satellite observation missions has been established. However, these studies all model the satellite coverage with a simple shape, such as a rectangle. Thus, design approaches that accommodate special mission requirements, such as the unique coverage geometry or the uneven placement of imaging targets, must still be considered.

One of the most popular observation tools is Synthetic Aperture Radar (SAR), and a SAR mission suitable for satellite constellations is the Interferometric Synthetic Aperture Radar (InSAR) [19]. InSAR is an observation method that detects minute changes in the Earth's surface by conducting multiple radar observations at the same location and measuring the phase difference between the reflected waves. This observation method is helpful because it can precisely observe changes in the Earth's surface caused by crustal movement [20]. However, SAR observations cannot take images in the nadir and front-back directions. Hence, geometrically simple coverage models such as rectangles and circles cannot be used in the mission design process of SAR satellites. In addition, particularly in InSAR, images should be captured from the same point at different times. When designing a satellite constellation for SAR (especially for InSAR) observation missions, these requirements must be considered. Although Zhang's research [21] for SAR observation missions concerned with specific coverage requirements for SAR observations, it evaluates orbit performance by investigating the limited number of candidate orbits, and no optimality is guaranteed. Therefore, it is necessary to establish an optimal design method for the Earth observation satellite constellation, considering mission requirements and observation conditions.

1.2.2 Constellation deployment control

Considering the launch cost, some satellites in the constellation are generally launched simultaneously into the same orbit. Therefore, research on orbit trajectory design and orbit control is essential to deploy satellites into the desired constellation configuration after launch appropriately.

One approach for this purpose is optimization-based deployment maneuver design. As in previous studies on optimization-based constellation deployment, Liu [22] proposed an optimal maneuver design method using Simulated Annealing. Pasquale [23] introduced a multi-objective trajectory optimization method, and Crisp [24] designed a large-scale, integrated deployment maneuver based on trade-off relations of the entire satellite system. However, these studies assume the fuel consumption during the orbit transition. Thus, it is difficult to adopt these methods for nano- or micro-satellites. Fuel consumption is one of the biggest problems for small satellites, particularly for nano- and micro-satellites. To extend mission lifetimes, it is necessary to conduct the constellation deployment maneuver without fuel consumption. One method for achieving fuel-free orbit deployment in Low Earth Orbit (LEO) is the use of the differential drag proposed by Leonard in 1979 [25, 26]. In this method, each satellite executes different attitude maneuvers to control the effect of the atmospheric drag. Then, each satellite takes a different orbit trajectory. To realize the desired constellation, it is essential to appropriately design attitude maneuvers and the resulting orbit transitions for each satellite. Concerning the deployment maneuver design with the differential drag, Li [27] designed a drag-based constellation deployment maneuver using the optimization method. In addition, Sin [28] also proposed a drag-based optimal maneuver design method using Simulated Annealing. However, one problem with the optimization-based maneuver design is the long computation time. Therefore, these methods cannot be used in on-board calculations for real-time orbit control during the deployment.

Pontani [29, 30] proposed a constellation deployment method using nonlinear control as one approach to achieving orbit deployment without complex optimization calculations. Another approach is using analytical solutions for the trajectories of the required attitude maneuver and the resulting orbit trajectories. Shang [31] analytically expressed satellite deployment maneuvers within the same orbital plane. However, these studies assume the use of thrusters for orbit deployment. Based on these considerations, an analytical solution for constellation deployment without fuel consumption using differential drag has been formulated [32]. Nevertheless, that research only considers conditions immediately after launch and cannot be used for the recalculations during deployment. Thus, the orbit control method for the drag-based constellation deployment using the analytical maneuver model has yet to be proposed.

1.2.3 Optimal mission scheduling

The actual mission operation is considered after the mission design and initial operation phases. Optimal observation scheduling of the satellite during the mission period is necessary to implement the actual mission efficiently. This chapter establishes a mission scheduling method for an Earth observation satellite flying in a given orbit to perform more observations efficiently.

Defining mission performance evaluation indicators and performing optimization under the necessary constraints is a common way to achieve optimal mission scheduling. In previous studies, some addressed maximizing the total weight of assigned tasks [33, 34, 35], and Spangelo [36] considered maximizing data download. Research was also conducted on optimization, considering multiple evaluation functions, such as the average image quality and the total weight [37, 38]. Kim [39] considered the optimization for multiple satellites' rapid observation of target areas. A lot of optimization methods are used for satellite mission scheduling according to the problem settings and objective functions, for example, genetic algorithm [37, 38, 39], taboo search [34], and ant colony optimization [33, 35]. When considering these mission scheduling problems, the maneuver time calculation is a severe problem. Since the satellite's attitude kinematics are nonlinear, complex computation is needed to calculate the attitude maneuver time. The computation time should be reduced because thousands of iterations are performed in optimization algorithms. As in previous studies of the maneuver time calculation, an approximated tabulation technique [40] and a data fitting method [41] were proposed. However, these researches do not consider the actual motion of the satellite's attitude control actuators. Reaction wheels and Control Moment Gyros (CMGs) are mainly used as attitude control actuators. In this research, CMGs are considered. The advantage of CMGs is their large torque. If CMGs are installed on satellites, faster attitude maneuvers can be achieved, and more targets can be observed during the mission period. From above, an optimal imaging mission scheduling method by a satellite equipped with a pyramid configuration CMG system as attitude control actuators is needed.

In the scheduling process, it is necessary to calculate the attitude maneuvering law using the CMGs. The previous maneuver calculation method with nonlinear optimization [42] requires several seconds for computation. If this method is applied in the mission scheduling optimization process, it takes too long time to finish the optimization since thousands of calculations are required. Kawajiri [43] used the maximum angular momentum calculated by the interior-point method as an attitude maneuver calculation method with a low computational cost. However, that research considers only large attitude changes of tens of degrees and is not applicable to the small attitude changes required for Earth observation. From above, a low-cost maneuver calculation method for a satellite with pyramid configuration CMGs for arbitrary attitude maneuvers is also needed.

1.3 Thesis overview

This thesis comprehensively discusses all phases of the satellite constellation mission from the mission design to actual operation. Chapters 2, 3, and 4 focus on the pre-launch mission design, initial operation after launch, and actual mission operation, respectively. The organization of this thesis is shown in Fig. 1.1. Chapter 2 considers the optimal orbit design problem of the constellation. Based on the given mission requirements, orbits should

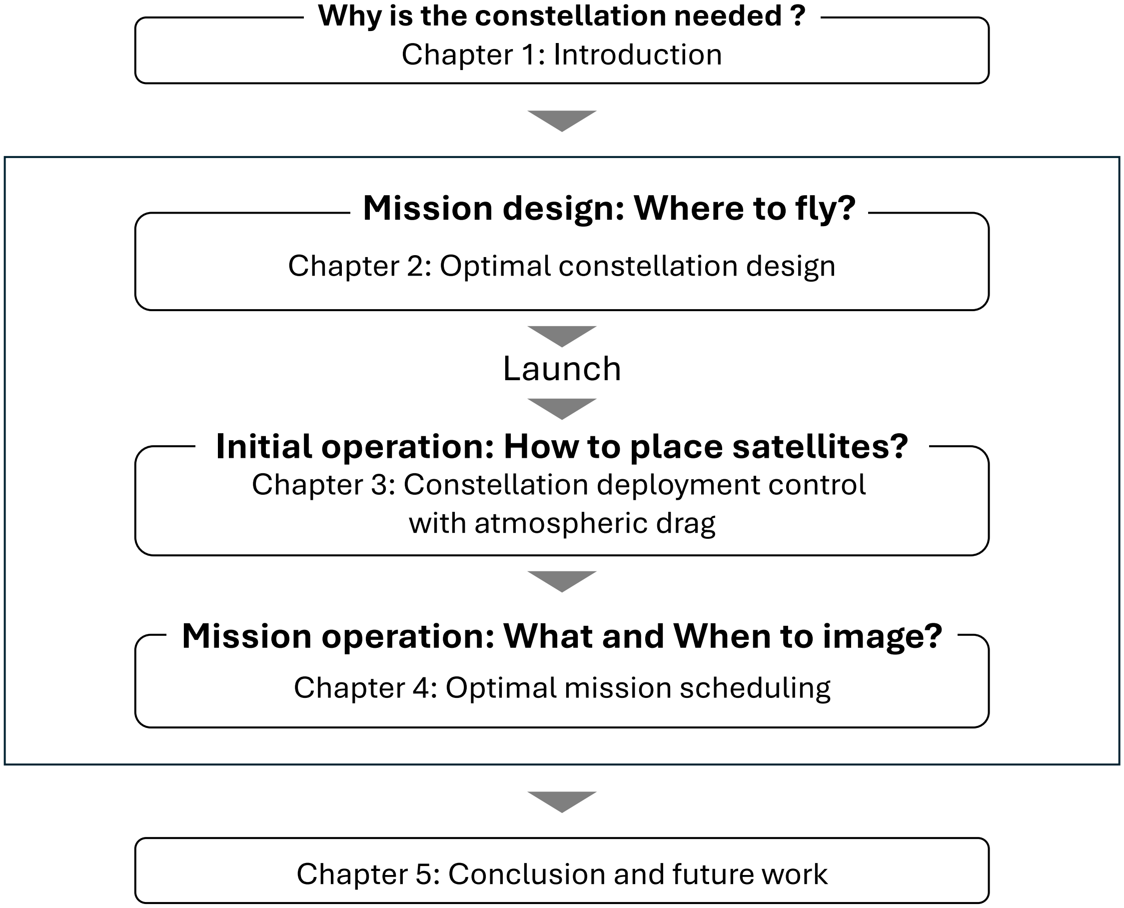

Figure 1.1: Organization of thesis.

be planned appropriately to execute the mission more efficiently. Once the orbit design is completed, Chapter 3 considers the initial operations immediately after launch. In order to perform the mission, launched satellites must be deployed to the correct constellation configuration. Hence, this chapter proposes a constellation deployment control method using atmospheric drag. Chapter 4 proposes a mission scheduling method for an Earth observation satellite. The optimal mission scheduling problem for the satellite is formulated as the attitude maneuver schedule optimization problem, considering the satellite condition, imaging requirements, and actuator behavior. The low-cost attitude maneuver computation law to execute the observation mission with CMGs is also proposed in this chapter. Finally, Chapter 5 summarizes the thesis. This research will contribute to achieving the human's sustainable Earth management system by solving technical problems in each phase of the satellite constellation mission. The details of each chapter are shown below.

Chapter 2: Optimal constellation design

Based on the background in section 1.2.1, this chapter focuses on the optimal constellation design based on satellite ground track configurations. Considering the constraints and mission requirements needed for InSAR observations, the optimal design problem is described and solved using the meta-heuristic optimization method. First, the orbit dynamics are formulated using Kepler orbital elements. From dynamics equations (Gauss's planetary equations), the effect of the J_2 perturbations in one orbit is evaluated, and the averaged time derivative of each orbital element is formulated. From this, the analytical model of orbital element trajectories is formulated. Using the obtained analytical orbit model, orbit conditions for single satellites to perform InSAR observation, repeating Sun-synchronous orbits, are mathematically formulated. By comparing the two types of expressions of the satellite position vector, the expression using the orbital element and the expression using the latitude and longitude of the nadir point, the calculation method of the satellite ground track is shown. Then, orbital requirements considering the ground track placement of multiple satellites to perform InSAR observations are presented. From these conditions, an optimal constellation design problem can be formulated as a multi-objective mixed-integer programming model, and a method to solve the problem is proposed. Finally, the results of the optimal constellation design using the proposed method for several mission conditions are presented.

Chapter 3: Constellation deployment control with atmospheric drag

This chapter proposes the atmospheric drag-based in-plane constellation deployment method for the initial operation of the mission. The required attitude maneuver and the resulting orbit trajectories are formulated analytically to achieve the required constellation configuration with the smallest altitude decrease. Then, an orbit control method based on these analytical models is constructed. First, the simplified orbit dynamics considering the atmospheric drag and averaged J_2 perturbation are formulated by simplifying Gauss's planetary equations. Then, as reference attitude and orbit maneuvers, each satellite's optimal cross-section trajectory and the resulting orbit trajectory are obtained using Direct Collocation with NonLinear Programming (DCNLP). The attitude maneuver, orbit trajectories, and deployment time are analytically modeled from the obtained optimal trajectories. The accuracy of the obtained analytical solutions is verified by comparing them with the result of numerical simulations. Then, a control method based on the designed analytical model is proposed. The simulation verifies the usefulness of the proposed control method.

Chapter 4: Optimal mission scheduling

This chapter considers the optimal mission scheduling of the satellite with CMGs for the actual mission operation. The optimal imaging plan for the satellite during the mission is formulated as the attitude maneuver scheduling problem, considering the satellite condition, imaging requirements, and actuator behavior as constraint conditions. Using these constraints, the mission scheduling optimization problem is formulated as a mixed-integer programming problem. Then, the mission scheduling optimization method is solved using ant colony optimization to observe more targets more accurately. When calculating the maneuver time constraints, gimbal trajectories of CMGs and the satellite attitude maneuver should be calculated at a low computational cost. Thus, a low-cost satellite attitude maneuver computation law using CMGs is also proposed. Using the obtained optimal observation scheduling result, the validity of the proposed attitude maneuver estimation method is verified through the numerical simulation. Although this chapter considers the mission scheduling of a single satellite, the proposed design path selection algorithm and the candidate refinement method can be extended to multi-ground track situations. Hence, this research can be easily extended to mission planning for satellite constellations.

Chapter 2

Optimal constellation design

In this chapter, an optimal constellation design method is introduced. At the beginning, orbit dynamics, which is the basis of this research, are described. Considering requirements for the observation mission, orbit conditions are formulated. Taking such conditions into account, multiple constraint conditions and objective functions are mathematically expressed to reflect the mission requirements. Then, constellation design problems are formulated as a mixed-integer programming problem and solved by the ant colony optimization. The optimization is done for two mission cases, and the trend of the optimal solution is discussed.

2.1 Orbit dynamics model using orbital elements

2.1.1 Gauss's planetary equations

In this research, the Kepler orbital elements (orbit semi-major axis a, eccentricity e, inclination i, right ascension of ascending node Ω, argument of perigee ω, and true anomaly f) are used as parameters for the satellite orbit. Also, the argument of latitude θ is defined as $\theta = f + \omega$. Fig. 2.1 shows the relation between orbital elements and the satellite position.

Consider the coordinate system $\{\hat{\boldsymbol{r}}, \hat{\boldsymbol{s}}, \hat{\boldsymbol{h}}\}$ that moves with the satellite, where $\hat{\boldsymbol{r}}$ is the unit vector in the satellite direction, $\hat{\boldsymbol{h}}$ is the vector normal to the orbit plane (angular momentum direction), and the $\hat{\boldsymbol{s}}$ is a unit vector and satisfying $\hat{\boldsymbol{s}} = \hat{\boldsymbol{h}} \times \hat{\boldsymbol{r}}$. In this case, the perturbation force $\boldsymbol{F}_p$ applied to the satellite is expressed as follows:

$$\boldsymbol{F}_p = F_r \hat{\boldsymbol{r}} + F_s \hat{\boldsymbol{s}} + F_h \hat{\boldsymbol{h}}, \tag{2.1}$$

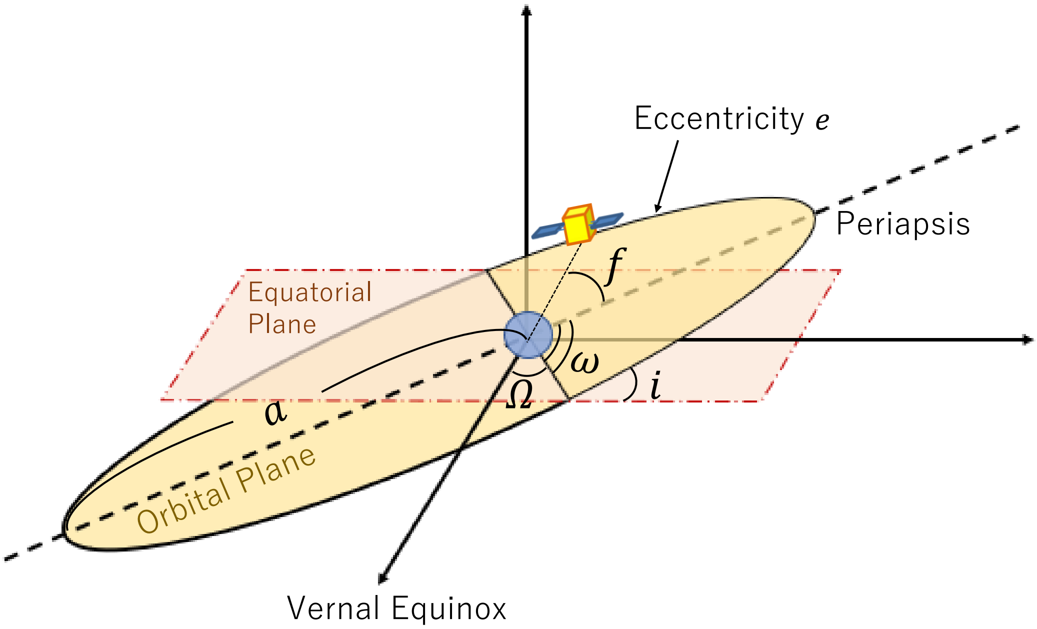

Figure 2.1: Relation between orbital elements and the satellite position.

where F_r, F_s, and F_h mean the $\{\hat{\boldsymbol{r}}, \hat{\boldsymbol{s}}, \hat{\boldsymbol{h}}\}$ elements of the perturbation force $\boldsymbol{F}_p$, respectively. If satellites perform the Keplerian motion without any perturbations, orbital elements a, e, i, Ω, and ω are constant. However, if these perturbation forces exist, these elements are not constant and vary according to the current position, velocity, and perturbation forces. Gauss's planetary equations, which represent the time variation of orbital elements when a perturbation force $\boldsymbol{F}_p$ is applied, are expressed as follows[44]:

$$\dot{a} = \frac{2}{n\eta}\left(F_r e \sin f + F_s \frac{p}{r}\right), \tag{2.2}$$

$$\dot{e} = \frac{\eta}{an}\left\{F_s \sin f + F_s\left(\cos f + \frac{e + \cos f}{1 + e\cos f}\right)\right\}, \tag{2.3}$$

$$\dot{i} = \frac{rF_h \cos\theta}{\sqrt{\mu p}}, \tag{2.4}$$

$$\dot{\Omega} = \frac{rF_h \sin\theta}{\sqrt{\mu p}\sin i}, \tag{2.5}$$

$$\dot{\omega} = -\frac{\eta}{ane}\left\{F_r \cos f - F_s\left(1 + \frac{r}{p}\right)\sin f\right\} - \frac{r\cot i}{a^2 n\eta}F_h \sin\theta, \tag{2.6}$$

$$\dot{M} = n + \frac{\eta}{ane}\left\{F_r\left(\cos f - \frac{2re}{p}\right) - F_s\left(1 + \frac{r}{p}\right)\sin f\right\}, \tag{2.7}$$

where $r = |\boldsymbol{r}|$ and $r = p/(1 + e\cos f)$ holds. When true anomaly f is used instead of mean anomaly M, the following relation holds:

$$\dot{f} = \frac{\sqrt{\mu p}}{r^2} + \frac{p}{\sqrt{\mu p}e}\left\{F_r \cos f - F_s \frac{\sin f(2 + e\cos f)}{1 + e\cos f}\right\}. \tag{2.8}$$

A method for obtaining true anomaly f from the known mean anomaly M is described here. The relation between eccentric anomaly E and M is expressed in Eq. (2.9) from Kepler's equation.

$$M = E - e\sin E. \tag{2.9}$$

When M is known, the value of E that satisfies Eq. (2.9) can be obtained from Newton's method. Using the obtained E, f can be calculated using the following equation:

$$\tan\frac{f}{2} = \sqrt{\frac{1 + e}{1 - e}}\tan\frac{E}{2}. \tag{2.10}$$

In the case of the circular orbit ($e = 0$), f, M, and E all coincide. Here, the J_2 perturbation is considered as the perturbation force in the orbit design. Other disturbances, such as the higher-order terms of the perturbation force and air drag, are not considered. Then, each component of $\boldsymbol{F}_p$ is described as follows:

$$F_r = \frac{3\mu J_2 R_E^2}{2r^4}(3\sin^2 i \sin^2\theta - 1), \tag{2.11}$$

$$F_s = -\frac{3\mu J_2 R_E^2}{2r^4}\sin^2 i \sin 2\theta, \tag{2.12}$$

$$F_h = -\frac{3\mu J_2 R_E^2}{2r^4}\sin 2i \sin\theta. \tag{2.13}$$

2.1.2 The evaluation of perturbations in one orbit

By integrating Gauss's planetary equations from 0 to 2π with f using Eqs. (2.2) - (2.8), the deviation of orbital elements in one orbit caused by the effect of J2 perturbation can be obtained as follows:

$$\Delta a = 0, \tag{2.14}$$

$$\Delta e = 0, \tag{2.15}$$

$$\Delta i = 0, \tag{2.16}$$

$$\Delta\Omega = -\frac{3\pi J_2 {R_E}^2 \cos i}{a^2(1-e^2)^2}, \tag{2.17}$$

$$\Delta\omega = \frac{3\pi J_2 {R_E}^2 (5\cos^2 i - 1)}{2a^2(1-e^2)^2}, \tag{2.18}$$

$$\Delta M = \frac{3\pi J_2 {R_E}^2 (3\cos^2 i - 1)}{2a^2(1-e^2)^{\frac{3}{2}}}. \tag{2.19}$$

From Eqs. (2.14) - (2.19), a, e, and i do not fluctuate in one orbit, and only Ω, ω, and M shift. Here, using orbit mean angular velocity $n = \sqrt{\mu/a^3}$, the orbital period T can be obtained in the following manner:

$$T = \frac{2\pi}{n} = 2\pi\sqrt{\frac{a^3}{\mu}}. \tag{2.20}$$

Then, $\bar{\dot{\Omega}}$, $\bar{\dot{\omega}}$, and $\bar{\dot{M}}$ defined in Eqs. (2.21) - (2.23) can be treated as the averaged time derivative of Ω, ω, and M:

$$\bar{\dot{\Omega}} = \frac{\Delta\Omega}{T} = -\frac{3\pi J_2 {R_E}^2 \cos i \sqrt{\mu}}{2a^{\frac{7}{2}}(1-e^2)^2}, \tag{2.21}$$

$$\bar{\dot{\omega}} = \frac{\Delta\omega}{T} = \frac{3\pi J_2 {R_E}^2 (5\cos^2 i - 1)\sqrt{\mu}}{4a^{\frac{7}{2}}(1-e^2)^2}, \tag{2.22}$$

$$\bar{\dot{M}} = \frac{\Delta M}{T} = \frac{3\pi J_2 {R_E}^2 (3\cos^2 i - 1)\sqrt{\mu}}{4a^{\frac{7}{2}}(1-e^2)^{\frac{3}{2}}}. \tag{2.23}$$

From the averaged time derivative of these elements, the values of Ω, ω, and M at time t can be analytically formulated as follows:

$$\Omega = \Omega_0 + \bar{\dot{\Omega}}(t - t_0), \tag{2.24}$$

$$\omega = \omega_0 + \bar{\dot{\omega}}(t - t_0), \tag{2.25}$$

$$M = M_0 + \bar{\dot{M}}(t - t_0), \tag{2.26}$$

where Ω_0, ω_0, and M_0 is the values of Ω, ω, and M at $t = t_0$.

The validity of the analytical solution Eqs. (2.24) - (2.26) is evaluated. The analytical solution and the simulation result of trajectories of Ω and argument of latitude $\theta = f + \omega$ are compared in Figs. 2.2 and 2.3. "Approximate" in the figure means the analytical solution, and "Gauss" means the numerical solution obtained by integrating Gauss's planetary equations using the Runge-Kutta-Gill method. The simulation and analytical calculation are performed over two orbits. The satellite orbit is $a = 6939.15$[km], $e = 0$, $i = 97.64$[deg], and f is obtained from Eqs. (2.9) and (2.10). From Fig. 2.2, the analytical and numerical solutions of the argument of latitude are almost the same. Therefore, considering the time longer than several orbits, analytical solutions of the orbital element trajectories shown in Eqs. (2.24) - (2.26) are helpful. From now on, the circular orbit ($e = 0$) is assumed in this chapter. In addition, a, e, i are assumed to be constant, and Eqs. (2.24) - (2.26) are used to calculate the time-varying orbital elements Ω, ω, and M.

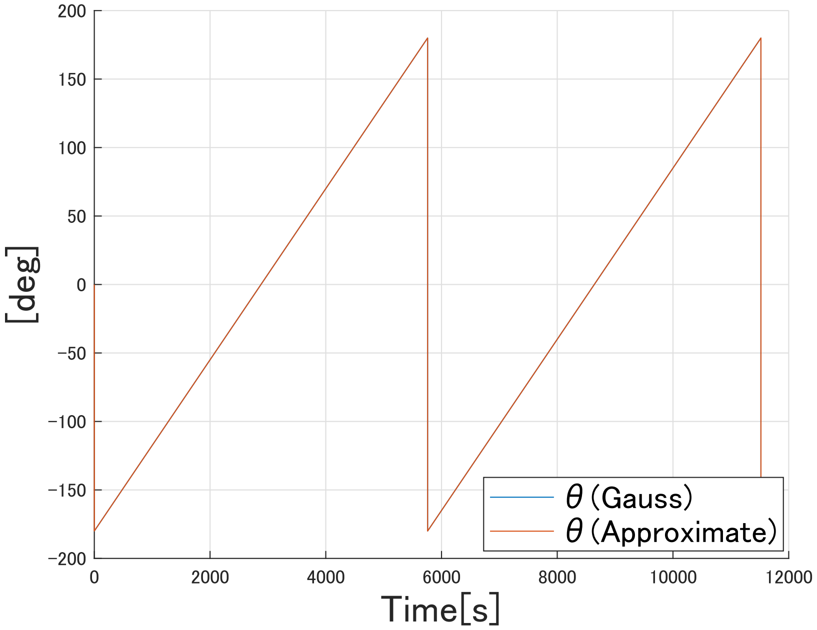

Figure 2.2: θ trajectories (analytical and numerical solution).

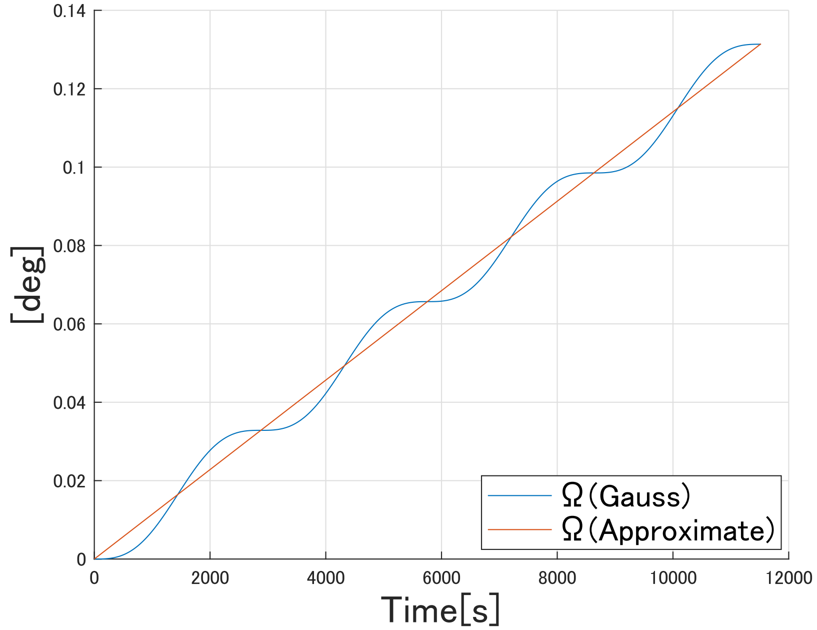

Figure 2.3: Ω trajectories (analytical and numerical solution).

2.2 Orbit conditions for Earth observation missions

Sun-synchronous orbit is a commonly used orbit for Earth observation missions. Earth rotates on average 360/365.2422 = 0.9856° per day around the Sun. Consider setting orbital elements so that the orbital plane perturbation $\Delta\Omega$ obtained from Eq. (2.5) will be equal to 0.9856°. Then, the angle between the orbital plane and the direction of the Sun does not fluctuate considerably. Such an orbit is called a Sun-synchronous orbit, which allows satellites to pass through their descending nodes at the same local solar time [45]. Therefore, Sun-synchronous orbit is widely used for LEO satellite missions such as positioning systems and Earth observations [46, 47], including InSAR observation missions [48]. Moreover, orbits whose ground track repeats after rotating m times around the Earth per N days are called repeating orbits. Repeating orbits are adequate for InSAR's repeated observation from the same point because they are guaranteed to return to the initial point. In this section, orbital elements conditions for repeating Sun-synchronous orbit are introduced.

2.2.1 Sun-synchronous orbit

The orbital elements condition to become a Sun-synchronous orbit is introduced. The time derivative of the orbital plane's drift caused by the perturbation, in other words, the time derivative of Ω can be described as shown in Eq. (2.5). In addition, the time variation of the direction of the Sun seen from the Earth can be expressed as follows:

$$\begin{aligned}\dot{\Omega}_s &= \frac{360}{365.2421897}[\text{deg/day}] \\ &= 1.991663853 \times 10^{-7}[\text{rad/sec}]. \end{aligned} \tag{2.27}$$

When $\dot{\bar{\Omega}} = \dot{\Omega}_s$ holds, the orientation of the orbital plane with respect to the Sun is permanently fixed. Such orbits are called Sun-synchronous orbits. Therefore, comparing Eqs. (2.5) and (2.27) under the condition of the circular orbit ($e = 0$), the condition for a and i to achieve the Sun-synchronous orbit is expressed in the following manner:

$$\cos i = -\frac{2 \times 1.991663853 \times 10^{-7}}{3 J_2 R_E^2 \sqrt{\mu}} a^{\frac{7}{2}}. \tag{2.28}$$

2.2.2 Repeating orbit

The orbital element condition is introduced to become a repeating orbit. The time for a satellite to complete one orbit around the Earth is called nodal period T_N, and the following relation holds:

$$T_N = \frac{2\pi}{n + \bar{\dot{M}} + \bar{\dot{\omega}}}. \tag{2.29}$$

Substituting $e = 0$ in Eqs. (2.22) and (2.23), T_N can be calculated in a following manner:

$$\begin{aligned} T_N &= 2\pi \left\{ n - \frac{3}{2} n J_2 \left(\frac{R_E}{a} \right)^2 (1 - 4\cos^2 i) \right\}^{-1} \\ &\approx \frac{2\pi}{n} \left(1 + \frac{3}{2} J_2 \left(\frac{R_E}{a} \right)^2 (1 - 4\cos^2 i) \right), \end{aligned} \tag{2.30}$$

where $J_2 = 1.08263 \times 10^{-3}$ and the relation $1 >> 3/2nJ_2(R_E/a)^2(1-4\cos^2 i)$ is considered. The orbit condition for a satellite to return to the initial position in N days after m orbits is that the drift of the descending node in m orbits is equal to $2\pi N$. This condition can be formulated in the following manner:

$$m T_N (\omega_e - \bar{\dot{\Omega}}) = 2\pi N. \tag{2.31}$$

By substituting Eqs. (2.6), (2.7), and (2.30) into Eq. (2.31), the condition for orbital elements a and i and repeating conditions N and m to become a repeating orbit is formulated as shown in Eq. (2.32) [49]

$$\frac{N}{m} = \sqrt{\frac{a^3}{\mu}} \left\{ 1 + \frac{3}{2} J_2 \left(\frac{R_E}{a} \right)^2 (1 - 4\cos^2 i) \right\} \left\{ \omega_e + \frac{3}{2} J_2 \left(\frac{R_E}{a} \right)^2 \sqrt{\frac{\mu}{a^3}} \cos i \right\}. \tag{2.32}$$

The repeating orbit can be achieved by setting proper a and i that satisfy Eq. (2.32) for the desired N and m. Generally, smaller N and m enable high-frequency observations, whereas the imageable area is limited, and vice versa. This is the trade-off of the satellite constellation for Earth observation missions.

2.2.3 Orbit design of repeating Sun-synchronous circular orbit

By substituting Eq. (2.28) to Eq. (2.32), the equation for a is obtained. From this equation and Eq. (2.28), the settings of a and i to achieve the repeating Sun-synchronous circular orbit for given N and m can be obtained. However, it is impossible to solve that equation analytically. Therefore, numerical calculation is performed in the following way:

1. Set desired values of N and m.

2. By substituting Eq. (2.28) into Eq. (2.32), the equation $f(a) = 0$ is obtained.
3. Calculate the approximated value of a from $N/m = \sqrt{a^3/\mu}\omega_e$, which is obtained from Eq. (2.32) when the J_2 perturbation is ignored.
4. Using the approximated a as an initial value, $f(a) = 0$ is solved with Newton's method.
5. Obtained a is substituted to Eq. (2.28) to obtain the orbital inclination i.

By performing the calculations in the above steps, orbital elements a and i such that the orit is a repeating Sun-synchronous circular orbit can be obtained.

2.2.4 Derivation of satellite ground tracks

In this section, the satellite ground track is determined. When satellite orbital elements $(a,\ e(=0),\ i,\ \Omega,\ \omega,\ M)$ at time t are given, The unit vector of the satellite direction $[\hat{\boldsymbol{r}}_s]_I$ and the position vector of the satellite $[\boldsymbol{r}_s]_I$ in the inertial frame $\mathcal{F}_I$ can be expressed as follows:

$$[\hat{\boldsymbol{r}}_s]_I = \begin{bmatrix} \hat{r}_x \\ \hat{r}_y \\ \hat{r}_z \end{bmatrix} = \begin{bmatrix} \cos\Omega\cos\theta - \sin\Omega\sin\theta\cos i \\ \sin\Omega\cos\theta + \cos\Omega\sin\theta\cos i \\ \sin\theta\sin i \end{bmatrix}, \tag{2.33}$$

$$[\boldsymbol{r}_s]_I = \begin{bmatrix} r_x \\ r_y \\ r_z \end{bmatrix} = a[\hat{\boldsymbol{r}}_s]_I. \tag{2.34}$$

The latitude and longitude of the nadir point of the satellite are denoted as θ_{el} and θ_{az}. Then, the unit vector of the satellite direction in $\mathcal{F}_E$ can be expressed as follows:

$$[\hat{\boldsymbol{r}}_s]_E = \begin{bmatrix} \cos\theta_{\text{az}}\cos\theta_{\text{el}} \\ \sin\theta_{\text{az}}\cos\theta_{\text{el}} \\ \sin\theta_{\text{el}} \end{bmatrix}, \tag{2.35}$$

where north latitude and east longitude are described as positive values, respectively. When the angle between $\mathcal{F}_E$ and $\mathcal{F}_I$ at time t is defined as λ, the relation $\lambda = \lambda_0 + \omega_E t$ holds. λ_0 is the value of λ at the initial time t=0. How to calculate λ_0 is explained later. Then, the unit vector of the satellite direction in $\mathcal{F}_I$ can be expressed as follows:

$$[\hat{\boldsymbol{r}}]_I = \begin{bmatrix} \cos\lambda & -\sin\lambda & 0 \\ \sin\lambda & \cos\lambda & 0 \\ 0 & 0 & 1 \end{bmatrix} \begin{bmatrix} \cos\theta_{\text{az}}\cos\theta_{\text{el}} \\ \sin\theta_{\text{az}}\cos\theta_{\text{el}} \\ \sin\theta_{\text{el}} \end{bmatrix}. \tag{2.36}$$

Both Eqs. (2.33) and (2.36) mean the unit vector of the satellite direction in the inertial system $\mathcal{F}_I$. Since they must be equal, we can calculate the latitude and longitude of the satellite nadir point by comparing their components. From the third component of both vectors, the following relation holds:

$$\hat{r}_z = \sin\theta_{\rm el}. \tag{2.37}$$

Since the range of the longitude of the satellite $\theta_{\rm el}$ is $-\pi/2 \leqq \theta_{\rm el} \leqq \pi/2$, $\theta_{\rm el}$ can be calculated as follows:

$$\theta_{\rm el} = \arcsin(\hat{r}_z). \tag{2.38}$$

From above, the latitude of the satellite nadir point can be determined without using λ. On the other hand, the value of λ at time t is needed when we calculate the longitude. Since $\lambda = \lambda_0 + \omega_E t$, when λ_0 is determined, the value of λ at any time can be calculated. Thus, the longitude can also be calculated. As mentioned in Eq. (2.33), the unit vector of the satellite direction at the initial time ($t = 0$) is determined from the initial values of orbital elements and can be described as follows:

$$[\hat{\boldsymbol{r}}_{s0}]_I = \begin{bmatrix} \cos\Omega_0\cos\theta_0 - \sin\Omega_0\sin\theta_0\cos i_0 \\ \sin\Omega_0\cos\theta_0 + \cos\Omega_0\sin\theta_0\cos i_0 \\ \sin\theta_0\sin i_0 \end{bmatrix}, \tag{2.39}$$

where the subscript 0 means the value at the initial time. The satellite is assumed to be the ascending node (the latitude is zero) at $t = 0$, and the longitude of the initial position is described as $\theta_{\rm az0}$. Since the satellite orbit is a repeating Sun-synchronous orbit, the initial position of the satellite can be assumed to be the ascending node without loss of generality. Then, by comparing the first and the second components of Eqs. (2.36) and (2.39), λ_0 can be calculated in the following equation:

$$\lambda_0 = \Omega_0 - \theta_{\rm az0}. \tag{2.40}$$

From the obtained λ_0, $\lambda = \lambda_0 + \omega_E t$ in any time t can be determined. Also, the satellite longitude and latitude trajectories can be calculated using the following procedure. First, the latitude $\theta_{\rm el}$ obtained from Eq. (2.38) and λ are substituted into Eq. (2.36). Then, by comparing the first and the second components of Eqs. (2.33) and (2.36), the longitude of the satellite nadir point $\theta_{\rm az}$ at any time t can be determined. In this way, the satellite ground track can be determined from the nadir longitude and latitude of the initial position and satellite position vector in the inertial systems.

2.3 Ground track following

2.3.1 Necessity of ground track following

To perform InSAR observations, it is necessary to image the target points multiple times at different times from the same location. Therefore, in the case of a satellite moving in a repeating orbit, images can be taken from the same point at different times with only one satellite because it will return to the same point every N days. If multiple satellites in a constellation move along the same ground track, the imaging interval can be shortened. Thus, faster and more accurate observations can be achieved. This section describes setting up orbital elements so that multiple satellites follow the same ground track. The chief determines the reference ground track, and deputies follow it. The chief and deputies take the same orbit semi-major axis a and orbital inclination i; in other words, they take repeating Sun-synchronous orbits with the same N and m. On the other hand, RAAN Ω and the argument of latitude θ at the initial time can be different. In this section, in-plane placement of the satellite (with the same Ω) to all satellites taking the same ground track is considered first. Out-plane placement is considered next. In this section, averaged analytical solutions shown in Eqs. (2.21) - (2.23) are used as time derivatives of Ω, ω, and M.

2.3.2 Ground track following of satellites in the same orbital plane

The number of satellites placed in one orbital plane is denoted as S. Satellite 1 is the chief of the ground track, and satellites 2 to S are the deputies that take the same ground track as satellite 1. The difference in the argument of latitude between satellite 1 and satellite j ($2 \leqq j \leqq S$) is denoted as ΔM_j. A configuration example for $S = 3$ is shown in Fig. 2.4.

From Eq. (2.34), the position vector $\boldsymbol{r}_{Sj}(t, \Delta M_j)$ of deputy j at time t is described as follows:

$$\begin{aligned} \boldsymbol{r}_{Sj}(t, \Delta M_j) &= a \begin{bmatrix} \cos\Omega\cos\Theta(t) - \sin\Omega\sin\Theta(t)\cos i \\ \sin\Omega\cos\Theta(t) + \cos\Omega\sin\Theta(t)\cos i \\ \sin\Theta(t)\sin i \end{bmatrix}, \\ \Theta(t) &= \theta_0 + \Delta M_j + \dot{\theta}t. \end{aligned} \tag{2.41}$$

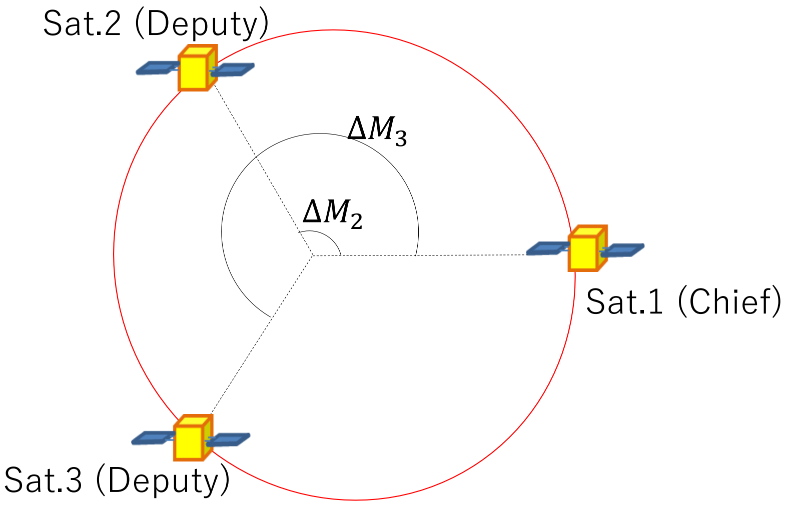

Figure 2.4: Example of satellite in-plane configuration ($S = 3$).

From Eq. (2.36), the position vector of the observation target point $\boldsymbol{r}_C(t, \theta_{\mathrm{el}}, \theta_{\mathrm{az}})$, with latitude θ_{el} and longitude θ_{az} at time t, is described in the following manner:

$$\boldsymbol{r}_C(t, \theta_{\mathrm{el}}, \theta_{\mathrm{az}}) = R_E \begin{bmatrix} \cos(\theta_{\mathrm{az}} + \lambda_0 + \omega_e t) \cos\theta_{\mathrm{el}} \\ \sin(\theta_{\mathrm{az}} + \lambda_0 + \omega_e t) \cos\theta_{\mathrm{el}} \\ \sin\theta_{\mathrm{el}} \end{bmatrix}. \tag{2.42}$$

For the ground tracks of satellite 1 and j to coincide, satellite j should fly over the initial position of satellite 1 at time t. In other words, the location of satellite 1 and the observation target at the initial time should coincide with the location of satellite j and the observation target at time t. This relation can be formulated as follows:

$$\boldsymbol{r}_{S1}(0,0) - \boldsymbol{r}_C(0, \theta_{\mathrm{el}}, \theta_{\mathrm{az}}) = \boldsymbol{r}_{Sj}(t, \Delta M_j) - \boldsymbol{r}_C(t, \theta_{\mathrm{el}}, \theta_{\mathrm{az}}). \tag{2.43}$$

By substituting Eqs. (2.41) and (2.42) into Eq. (2.43), the condition for ground tracks of satellites in the same orbital plane to coincide is expressed as follows:

$$\begin{cases} \omega_e t = 2\pi k \\ \Delta M_j + \dot{\theta} t = 2\pi l \end{cases} \quad (k, l \text{ are integer variables}). \tag{2.44}$$

The first equation of Eq. (2.44) holds only when $t = 24 \times 60 \times 60 \times d = 86400d$ [s] (d is an integer). Taking this into account and transforming the second equation, the following equation is obtained:

$$\Delta M_j = 2\pi \left\{ \mathrm{ceil}\left(D\frac{m}{N} \right) - D\frac{m}{N} \right\} (D = 1, 2, \cdots, N-1[\mathrm{day}]), \tag{2.45}$$

where ceil(p) means the integer rounded up to the real number p. From Eq. (2.45), up to N satellites in one orbital plane can track the same ground track. When N satellites are placed so that all satellites track the same ground track, the imaging frequency of the same point is 1 day. This is the minimum imaging interval of the single-plane constellation.

2.3.3 Ground track following of satellite in other orbital planes

From Eq. (2.45), when all satellites in the same orbital plane have the same ground track, the maximum number of satellites that can be placed is N, and the minimum time to revisit the same point is one day. In other words, we cannot shorten the revisit time to less than one day by placing all satellites in the same orbital plane. Here, it is possible to observe the same targets more frequently by placing deputies correctly in other orbital planes. If all satellites in P orbital planes take the same ground track at equal intervals, revisit time can be shortened to $1/P$ days. Consider orbital plane 1 as the reference orbital plane and another orbital plane k ($2 \leqq k \leqq P$) as the dependent orbital plane. Satellite 1 in the orbital plane k is the chief of the orbital plane k. The phase difference between orbital plane 1 and orbital plane k is $\Delta\Omega_k$, and the difference in the argument of latitude between the reference satellite of plane 1 and the reference satellite of plane k is described $\Delta m_{k,1}$. An example of satellite configuration is shown in Figs. 2.5 and 2.6.

Settings of $\Delta\Omega_k$ and Δm_k for satellite k to pass over the initial nadia point of the chief (descending node) at time t_a is introduced here. Due to the effect of the Earth's rotation and perturbation of Ω, the longitude of the nadir point changes $-(\omega_E - \dot{\Omega})t_a$ during time t_a. Therefore, to follow the ground track, the following relation should hold:

$$\Delta\Omega = (\omega_E - \dot{\Omega})t_a. \tag{2.46}$$

In addition, the chief's argument of latitude changes from 0 to $(\dot{M} + \dot{\omega})t_a$ during time t_a. Therefore, for the deputy to pass over the chief's initial position at time t_a, Δm_k should meet the following condition:

$$\Delta m_k = -(\dot{M} + \dot{\omega})t_a. \tag{2.47}$$

By setting the orbital element of the chief of the orbital plane k from Eqs. (2.46) and (2.47), the chief of plane k follows the same ground track as the chief of plane 1. Here,

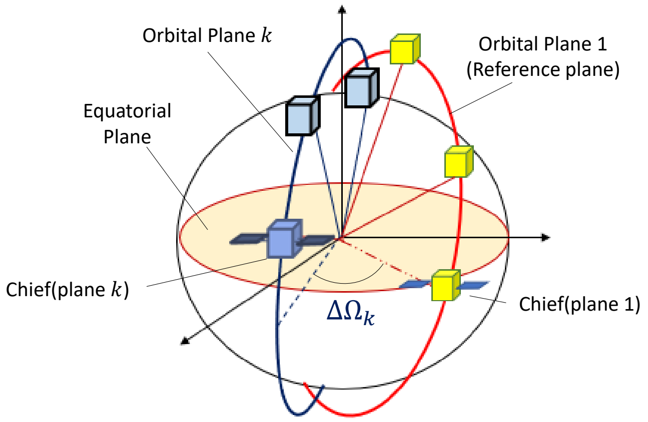

Figure 2.5: Example of the orbital plane placement.

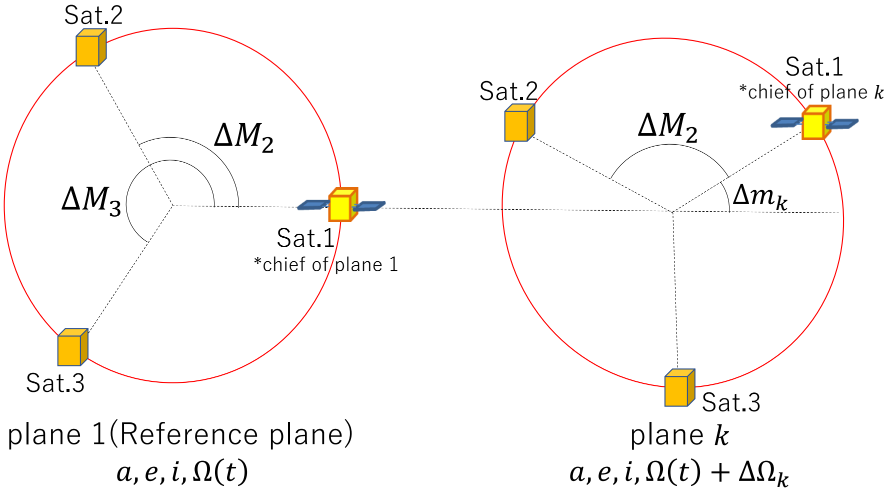

Figure 2.6: Example of satellite configuration ($S = 3$).

we consider the P orbital planes constellation with N satellites in one plane. When all satellites evenly follow the same ground track, the imaging interval of a target can be shortened to $1/P$ days. Set $t_a = k/P \times 86400$ [s] ($k = 1, 2, \cdots, P$) in Eqs. (2.46) and (2.47). Then, $\Delta\Omega_k$ and Δm_k for orbital plane k is expressed as follows [6, 7]:

$$\Delta\Omega_k = (\omega_e - \dot{\Omega}) \left(\frac{mT_N}{N} \times \frac{k-1}{P} \right), \tag{2.48}$$

$$\Delta m_k = -(\dot{M} + \dot{\omega}) \left(\frac{mT_N}{N} \times \frac{k-1}{P} \right). \tag{2.49}$$

2.4 Summary of orbital element conditions

From section 2 and 2.3, conditions for the InSAR observation constellation using the repeating Sun-synchronous circular orbit are summarized as follows:

- The ground track can be determined from N, m, and the chief's initial descending node θ_{az}.
- Up to N satellites in one orbital plane can follow the same ground track.
- When satellites with the same ground track are placed on one orbital plane to the maximum extent, the revisit frequency to the same point (i.e., the InSAR imaging frequency) is 1 day.
- If P orbital planes are evenly placed, the InSAR imaging frequency of the constellation system can be shortened to $1/P$ days.

2.5 Optimal constellation design

A multi-satellite constellation enables an InSAR observation mission to observe more accurately than a single satellite mission. As the number of satellites following the same ground track increases, the observation from the same point can be more frequent, and the observation data can be more accurate. On the other hand, expanding constellation coverage by increasing the number of ground tracks helps observe more targets. However, when the maximum number of satellites placed in the constellation is limited, increasing the number of ground tracks will reduce the number of satellites that can follow each ground track, decreasing the imaging frequency for each target. From the above, to carry out the Earth observation mission with a satellite constellation, it is essential to properly design design parameters such as the number of ground tracks, repeat cycle N, and the number of orbits to repeat m, for a given maximum number of satellites. In this section, the optimal constellation design problem is formulated as a nonlinear mixed-integer programming problem and describes how to find the optimal satellite configuration.

2.5.1 Problem definition

This research focuses on a mission to image a predetermined target cities. Assuming that each ground track has the same N and m, the maximum number of satellites in the constellation is denoted as $N_{\mathrm{sat,max}}$, and the number of ground tracks is denoted as τ. Then, from Eq. (2.45), up to N satellites with the same ground track can be placed in the same orbital plane. Therefore, under N repeat cycles and τ ground tracks, up to τN satellites can be placed in one orbital plane. Define the number of orbital planes as P and assume that τN satellites, the maximum number of satellites per one plane, are placed in each orbital plane. From this setting, satellites pass over the same point at least once a day in all τ ground tracks. The number of satellites placed in the whole constellation is denoted as N_{sat} and can be calculated as follows:

$$N_{\mathrm{sat}} = P\tau N. \tag{2.50}$$

P satisfies the following relationship:

$$N_{\mathrm{sat}} = P\tau N \leqq N_{\mathrm{sat,max}} < (P+1)\tau N. \tag{2.51}$$

This means, for given N and τ, the number of orbital planes P is maximized so that the total number of satellites N_{sat} does not exceed $N_{\mathrm{sat,max}}$ under the condition that τN satellites are placed in one orbital plane. Each ground track is described as ground track l ($1 \leqq l \leqq \tau$), and ground track 1 is defined as the reference ground track of the constellation. The chief of ground track 1 is the reference satellite of the entire constellation and is assumed to be placed at the descending node at the initial time. The chief of ground track l ($l \geqq 2$) is the satellite placed in the same orbital plane as the chief of ground track 1 and follows ground track l. The example of $N = 3$ and $\tau = 3$ is shown in Fig. 2.7. Then, the difference in the argument of latitude between the reference satellite of ground track 1 and the reference satellite of ground track l is Δf_l, and the satellites are placed so that the following relationship holds:

$$\Delta f_l = \frac{2\pi(l-1)}{N\tau}. \tag{2.52}$$

From Eq. (2.52), descending nodes of τ ground tracks are evenly distributed on the equator. For ground track l, the difference in the argument of latitude between the chief and deputy in the reference orbital plane can be obtained from Eq. (2.45). In addition, the inter-orbital phase difference and the intra-orbital phase difference when placed in other orbital planes can be obtained from Eqs. (2.48) and (2.49).

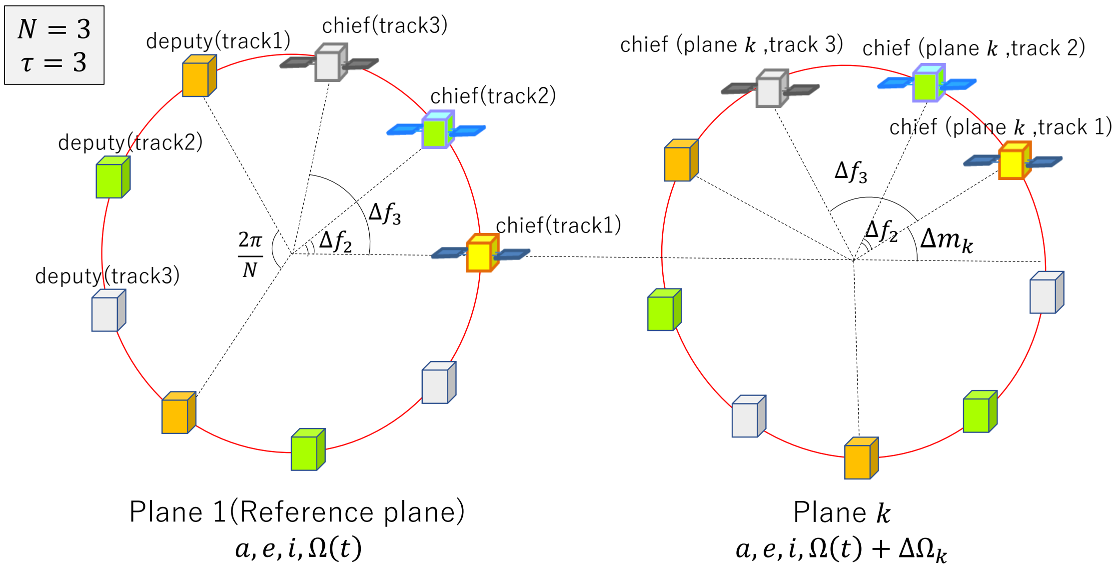

Figure 2.7: Example of satellite configuration for multiple planes.

2.5.2 Design parameters

In this research, the constellation design problem is formulated as the design problem of the satellite ground track's shape, number, and placement. Design parameters for the optimization are defined as

$$\boldsymbol{x} = [N, \tau, \gamma, \bar{m}], \tag{2.53}$$

where repeat cycle N and the number of ground tracks τ are integer variables, and the others are continuous variables. γ is the longitude parameter, and $\bar{m}$ is the repeating orbit parameter. They determine the longitude of reference descending node θ_{az} and m, respectively. N and $\bar{m}$ determine the shape, τ determines the number, and γ determines the placement of satellite ground tracks. The meaning of two continuous parameters, γ and $\bar{m}$, is described in the following section.

Longitude parameter γ

Since all τ ground tracks take the same N and m and are evenly distributed in this research, all ground track configurations can be determined automatically by only setting the longitude of one descending node of ground track 1 (chief ground track of the whole constellation), θ_{az}, which is called the reference longitude. Figure 2.8 shows an example of the configuration of each ground track and its descending nodes when $\tau = 3$. Considering that orbits are repeating Sun-synchronous orbits and each ground track is evenly distributed, the range of reference longitude θ_{az} can be narrowed down to $-360/(2m\tau) \leqq \theta_{\mathrm{az}} \leqq 360/(2m\tau)$ without the loss of generality. However, because the upper and lower bounds of reference longitude $\pm 360/(2m\tau)$ depend on design parameters m and τ, a range of θ_{az} cannot be set correctly in optimization tools. To solve this problem, a longitude parameter γ is introduced as an alternative design variable to θ_{az}. Using γ, the reference longitude can be described as follows:

$$\theta_{\mathrm{az}} = \frac{360}{m\tau}\gamma \qquad \left(-\frac{1}{2} \leqq \gamma \leqq \frac{1}{2}\right). \tag{2.54}$$

Using a variable γ with a fixed range as the design variable, optimization can be performed with a minimum search range.

Repeating orbit parameter $\bar{m}$

The relations among N, m, and the satellite altitude can be obtained from Eqs. (2.28) and (2.32). Thus, the satellite altitude depends on m, and there exist upper and lower limits of

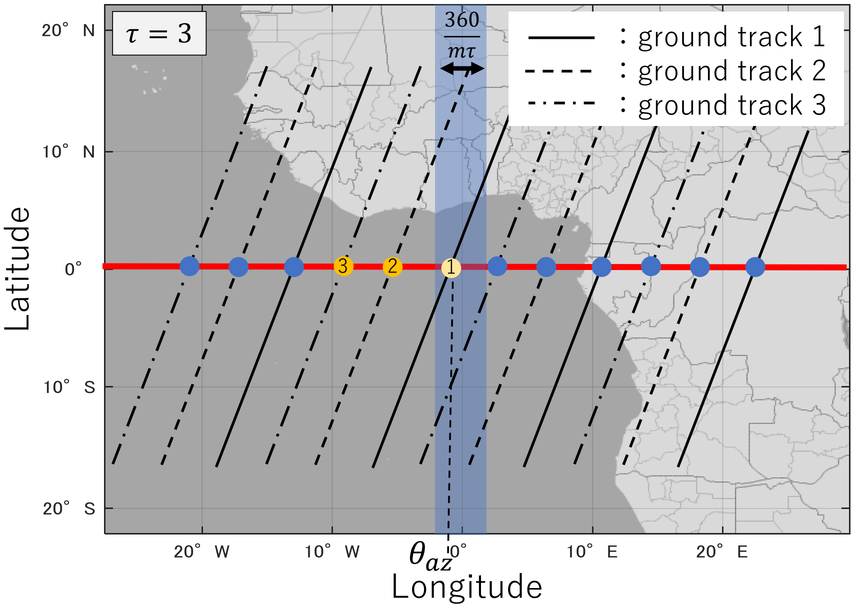

Figure 2.8: Example of ground track configuration ($\tau = 3$).

the altitude depending on the mission constraints, for example, observation instruments and communication requirements. Therefore, m must be limited in some range for a given repeat cycle N. For example, when the upper bound of the satellite altitude is 700 km and the lower bound is 400 km, $44 \leqq m \leqq 46$ for $N = 3$ and $146 \leqq m \leqq 155$ for $N = 10$. In this way, the range of m greatly changes according to the design parameter N. Therefore, the proper range of m cannot be directly set in the optimization algorithm. To solve this problem, a repeating orbit parameter $\bar{m}$ is introduced as an alternative design variable to m. Using $\bar{m}$ and N, m can be described as follows:

$$m = [N\bar{m}], \tag{2.55}$$

where $[x]$ is the floor function, which means the maximum integer number is less than or equal to a real number x. The parameter m can be designed with a constant design parameter range by giving upper and lower bounds of $\bar{m}$ according to the altitude constraints.

2.5.3 Objective functions

To evaluate constellation performance, it is necessary to consider mission requirements from multiple aspects, such as the number of imaging opportunities for each target, revisit time, fuel consumption, and so on. In this section, the four objective functions are described to evaluate constellation performance.

Number of orbital planes

When there are P orbital planes that contain τN satellites that meet the ground track tracking conditions, satellites pass over the same spot P times a day. Multiple observations from the same position are needed for InSAR observation, and a larger P enables a higher frequency of InSAR observations, which provides more accurate and more useful observation data. Therefore, by setting the first objective function f_1 as

$$f_1 = -P, \tag{2.56}$$

$-P$ is minimized, in other words, P is maximized in the optimization process to achieve high-frequency InSAR observations.

Number of observation windows

We describe a method for determining coverage, which indicates how many cities can be imaged from a given set of candidate cities by a satellite moving in a given orbit. When satellites conduct SAR observations, they mainly take images in the left-right direction and cannot take images in the nadir or front-back directions due to instrumental limitations [21]. Therefore, when angles α and β are represented as shown in Fig. 2.9 for given positions of satellites and target cities at a certain time, the target city can be imaged from the satellite at that time if the following conditions hold:

$$30^\circ \leqq |\alpha| \leqq 40^\circ, \tag{2.57}$$

$$|\beta| \leqq 5^\circ. \tag{2.58}$$

From Eqs. (2.5) - (2.7), the position vector of the satellite can be obtained. Therefore, from its position vector and Eq. (2.36), we can calculate the location of the satellite and candidate cities and obtain α and β at each time for each candidate city. If a satellite in the constellation satisfies Eqs. (2.57) and (2.58) at least once for a candidate city, the city is imageable in the constellation.

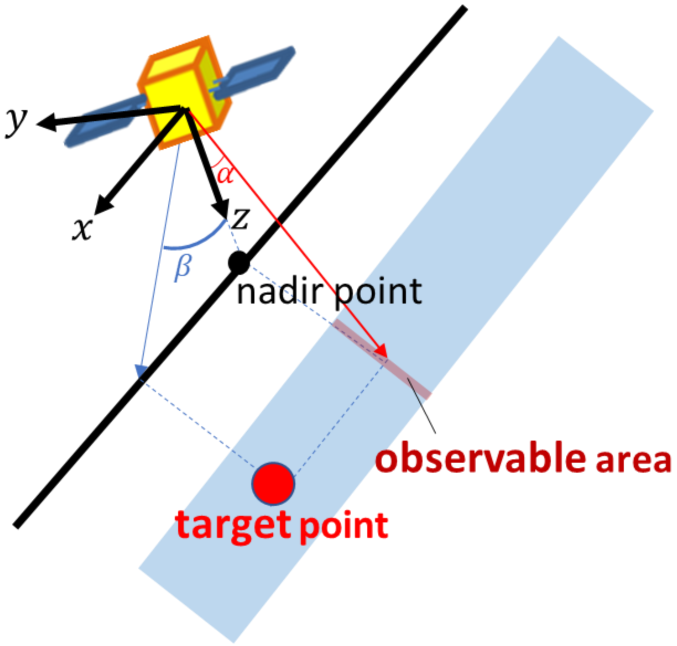

Figure 2.9: Coverage model for SAR observation.

Due to the effect of maneuver time and imaging time, not all candidate cities that satisfy Eqs. (2.57) and (2.58) cannot be imaged in the actual imaging missions [48]. To properly evaluate the number of observation opportunities by considering these constraints, an idea of "observation windows" is proposed. The mission period (N days) is separated into fixed time intervals, which are called observation windows. It is assumed that attitude maneuvers and imaging operations are performed within a single observation window and that only one target can be imaged in one observation window. Then, the number of observation windows in which there is at least one imageable target can be used as an indicator of the number of SAR observations that can actually be performed in the designed constellation. In this research, the length of a single observation window is set to 20 seconds, taking into account attitude maneuver scheduling results shown in Chapter 4. Suppose that the number of observation windows with at least one imageable target in a grand track l ($1 \leqq l \leqq \tau$) is w_l. Then, the objective function f_2 is formulated as follows:

$$f_2 = \sum_{l=1}^{\tau} w_l, \tag{2.59}$$

where f_2 represents the sum of the number of imageable observation windows over all ground tracks. Since a larger f_2 results in a greater number of SAR observation opportunities in the constellation, the optimization aims to maximize f_2.

Maximum waiting time

In Earth observation, there may be a situation where it is suddenly necessary to carry out an imaging mission to a specific city, for example, when a disaster occurs. To design a constellation that can respond quickly to such a situation, it is necessary to minimize the waiting time until each city becomes available for imaging. In this research, we define $\boldsymbol{X}_{\text{rev}}$ as a vector of the maximum waiting time between the time when each city is ready to be imaged and the time when it is ready to be imaged again, for all candidate cities as

$$\boldsymbol{X}_{\text{rev}} = [t_{1,\max}, t_{2,\max}, \cdots, t_{C,\max}]. \tag{2.60}$$

The mean value of $\boldsymbol{X}_{\text{rev}}$ is denoted as $\bar{X}_{\text{rev}}$, and the standard deviation of $t_{1,\max}$ to $t_{C,\max}$ is denoted as I_{rev}. Then, the maximum waiting time for each city should be small, and the bias of the values among all candidate cities should be also small. Therefore, the objective function f_3 for the maximum waiting time can be expressed as follows:

$$f_3 = \bar{X}_{\text{rev}} + I_{\text{rev}}, \tag{2.61}$$

and f_3 is minimized in the optimization.

Fuel consumption

In a low Earth orbit, altitude maintenance control by consuming fuel is needed because satellite altitude decreases due to atmospheric drag. Since atmospheric density exponentially decreases with increasing altitude, the lower the altitude of satellites is, the more fuel is needed to keep the altitude. Reducing fuel consumption is an important issue in the satellite constellation design. Here, we present a method to estimate fuel consumption for altitude maintenance with enough small computation costs to be included in the optimization algorithm. From Gauss's planetary equations, the time derivative of the semi-major axis a is described as follows [44]:

$$\dot{a} = \frac{2}{n\eta}\left(F_r e \sin f + F_s \frac{p}{r}\right). \tag{2.62}$$

Using cross-section A, velocity vector $\boldsymbol{v}(|\boldsymbol{v}| = v)$, drag coefficient C_d, and satellite mass m_{sat}, atmospheric drag $\boldsymbol{F}_{\text{drag}}$ is formulated as follows:

$$\boldsymbol{F}_{\text{drag}} = -\frac{1}{2m_{\text{sat}}}\rho C_d A v^2 \frac{\boldsymbol{v}}{v}. \tag{2.63}$$

When atmospheric drag is given as an external force in the direction of the velocity vector of Eq. (2.62), the time derivative of a is described as follows [9]:

$$\dot{a} \;=\; \frac{2a^{\frac{3}{2}}}{\sqrt{\mu}}\left(-\frac{\rho C_d A}{2m_{\mathrm{sat}}}v^2\right) = -\frac{\rho C_d A}{m_{\mathrm{sat}}}\sqrt{\mu a}, \tag{2.64}$$

where a circular orbit ($e = 0$) is assumed. For simplicity, we assume that the atmospheric density ρ is a constant which is determined only by the initial altitude of the satellite and is not affected by altitude decrease. Then, if the initial semi-major axis is set to $a_0 = h_{\mathrm{sat}} + R_E$, from Eq. (2.64), the value of the semi-major axis a at time t can be expressed analytically as follows:

$$a(t) = \left(\sqrt{a_0} - \frac{\rho C_d A}{2m_{\mathrm{sat}}}\sqrt{\mu}t\right)^2. \tag{2.65}$$

From Eq. (2.62), the amount of velocity increase ΔV required to raise the altitude of the satellite by Δa with one impulse can be expressed as follows:

$$\Delta V = \frac{n}{2}\Delta a. \tag{2.66}$$

From Eqs. (2.65) and (2.66), $\Delta V(h_{\mathrm{sat}}, T)$, the estimated fuel consumption per time T of a satellite moving at an altitude h_{sat}, can be described as follows:

$$\Delta V(h_{\mathrm{sat}}, T) = \frac{n}{2}(h_{\mathrm{sat}} + R_E - a(T)). \tag{2.67}$$

In this research, the estimated fuel consumption of one satellite per 1 day (86400 s) is used as the objective function. Therefore, the objective functionf_4 is expressed as follows:

$$f_4 = \Delta V(h_{\mathrm{sat}}, 86400), \tag{2.68}$$

and f_4 is minimized in the optimization.

Evaluation of the objective function f_4

In calculating the fuel consumption index f_4, approximations to atmospheric density and orbital angular velocity are incorporated to reduce calculation costs, and the approximated analytical solution of the orbit semi-major axis trajectory is obtained. Here, this analytical solution is compared with the result of the numerical simulation considering the atmospheric drag to verify the validity of the objective function f_4. When the position vector of the satellite is $\boldsymbol{r}$, the equations of motion for the two-body problem considering the perturbation forces acting on the satellite are as follows:

$$\ddot{\boldsymbol{r}} = -\mu \frac{\boldsymbol{r}}{r^3} + \boldsymbol{F}_{J2} + \boldsymbol{F}_{\mathrm{drag}}, \tag{2.69}$$

where $\boldsymbol{F}_{J2}$ and $\boldsymbol{F}_{\mathrm{drag}}$ can be calculated from Eqs. (2.11) - (2.13) and (2.63), respectively. The simulation result of the 10-day altitude trajectory is compared with the approximated analytical solution calculated from Eq. (2.65). The value of a shows periodic oscillation due to the effect of J2 perturbation. Since this oscillation is eliminated after one cycle from Eq. (2.14), the numerical solution for a is expressed by integrating the value over time and recording the average value for each cycle. In this research, three conditions, $(N, m) = (2, 29)$ (altitude 720.0 km), $(N, m) = (1, 15)$ (altitude 561.0 km), $(N, m) = (2, 31)$ (altitude 410.6 km) are considered. Comparisons of a's trajectories between simulation results and analytical solutions for each condition are shown in Figs. 2.10 - 2.12. Comparisons of the final semi-major axis and calculation time are shown in Tables 2.1-2.3. Simulations were performed using MATLAB®R2021a on an IntelCore(TM)i7-1165G7-based computer. The Runge-Kutta-Gill method is used for the numerical simulations, and the time step is set to 1 second.

Table 2.1: a after 10 days and computation time (altitude 720.0 km).

	a after 10 days [km]	Computation time [s]
numerical solution	7098.059	80.7
analytical solution	7098.061	2.76×10^{-3}

Table 2.2: a after 10 days and computation time (altitude 561.0 km).

	a after 10 days [km]	Computation time [s]
numerical solution	6938.738	75.0
analytical solution	6938.754	2.30×10^{-3}

Table 2.3: a after 10 days and computation time (altitude 410.6 km).

	a after 10 days [km]	Computation time [s]
numerical solution	6783.915	74.9
analytical solution	6784.095	3.39×10^{-3}

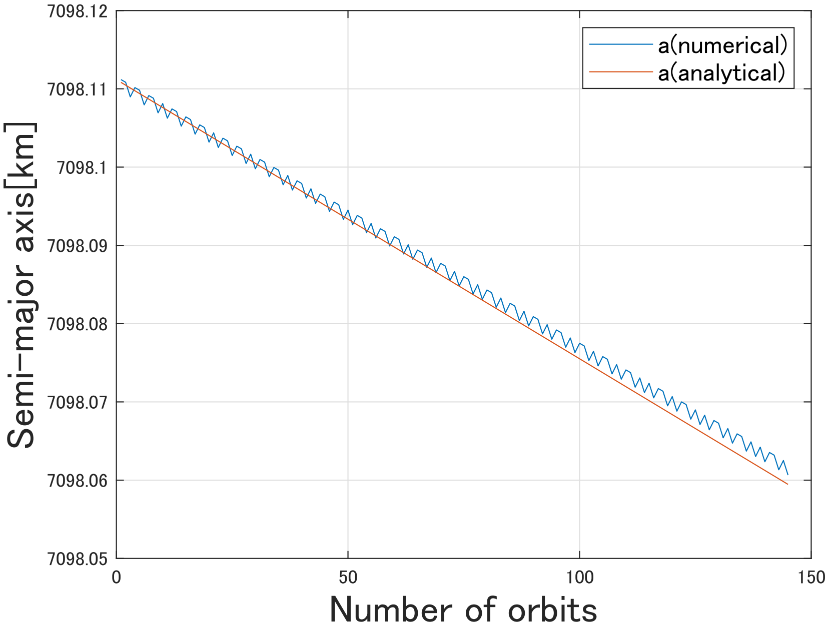

Figure 2.10: Altitude decrease caused by the atmospheric drag (altitude 720.0km).

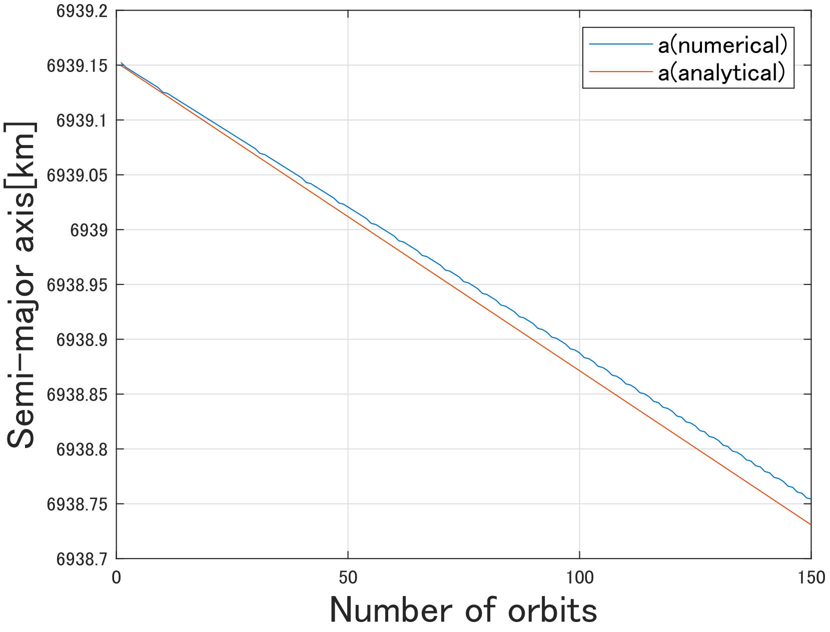

Figure 2.11: Altitude decrease caused by the atmospheric drag (altitude 561.0km).

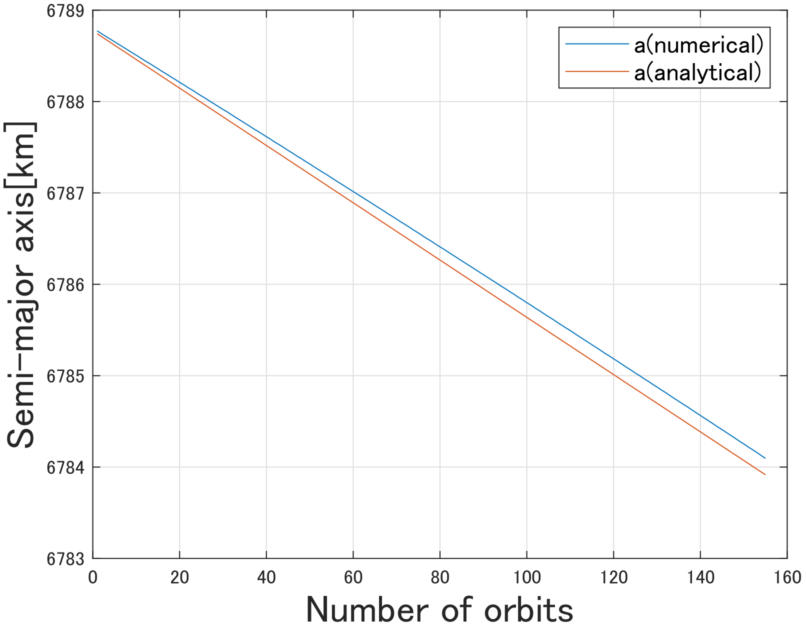

Figure 2.12: a decrease caused by the atmospheric drag (altitude 410.6km).

From Figs. 2.10 - 2.12 and Tables 2.1 - 2.3, altitude decrease error depends on the initial altitude. Even at the lowest altitude case, the error of the analytical solution is only 0.180 [km] over 10 days, which is 2.7×10^{-3}% of the numerical solution. The accuracy of the numerical solution is sufficient as an evaluation index for optimization calculations. In addition, the analytical solution reduces computation time by more than 99.99 % for all altitude conditions. Since thousands of calculations are performed in the optimization process, the computation time of objective functions should be reduced. From the above, we can conclude that f_4 is appropriate as an indicator of fuel consumption in terms of accuracy and computational cost.

2.5.4 Optimization conditions

We set constraints for optimization in the following ways:

- 500 [km] $\leqq h \leqq$ 700 [km]
- N and m are coprime each other
- All candidate cities are imageable
- $\tau N \leqq N_{\mathrm{sat,max}}$

The upper and lower bounds of the altitude are determined by the conditions of the observation instruments. In addition, because the constellation design assumes global coverage, the constellations with candidate cities that cannot be imaged are not focused. The upper and lower limits of the design variables and various parameters are shown in Tables 2.4 and 3.1.

The range of the repeating orbit parameter $\bar{m}$ is set so that all pairs of (N, m) that satisfy the altitude constraint condition are included. For given ranges of altitudes and repeat cycles, all possible (N, m) pairs in the given altitude range and N range are examined, and the possible altitudes for each N value are plotted in Fig. 2.13. The top twelve results from Fig. 2.13, sorted by altitude, are shown in Table 2.6. We set observation target cities as big cities with a population of more than one million, and the analysis is conducted by considering two mission patterns with different observation areas. In the first analysis, 292 cities all over the world are set as the candidate cities to be imaged. The second analysis considers satellite missions that observe dense target cities within a specific area. In this research, as the case study of the second analysis, 99 cities in Asia

Table 2.4: Range of design parameters.

Design parameters	Symbol	Min	Max
Repeat cycle	N	1	30
Number of ground track	τ	1	30
Longitude parameter	γ	-0.5	0.5
Repeating orbit parameter	$\bar{m}$	14.5	15.5

Table 2.5: Various constellation conditions.

Parameter	Symbol	Value	Unit
Maximum number of satellites	$N_{\mathrm{sat,max}}$	30	-
Satellite mass	m_{sat}	100	kg
Satellite cross-section	A	2	m^2
Drag coefficient	C_d	2.2	-

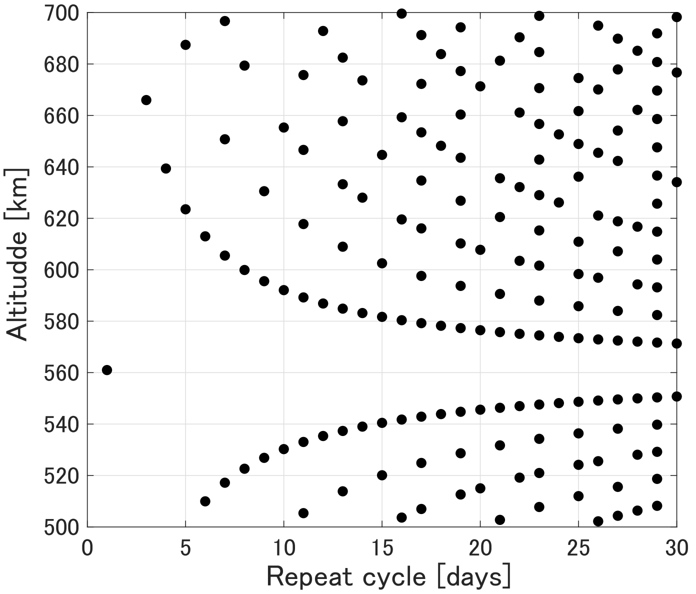

Figure 2.13: Relation between repeat cycle N and possible altitudes.

Table 2.6: Pair of (N, m) (top 12 highest altitude).

Repeat cycles N	Repeating orbits m	altitude [km]
16	233	699.6
23	335	698.7
30	437	698.2
7	102	696.7
26	379	694.9
19	277	694.3
12	175	692.8
29	423	691.9
17	248	691.2
22	321	690.4
27	394	689.8
5	73	687.4

are regarded as the candidate cities. Fig. 2.14 shows the distribution of candidate cities. The list of candidate cities is shown in the appendix. Meta-heuristic methods such as genetic algorithms are commonly used for the optimization problem, and in this research, ant colony optimization [50] is used as the optimization method. In the next section, we show the results of the optimal constellation design for the above two patterns.

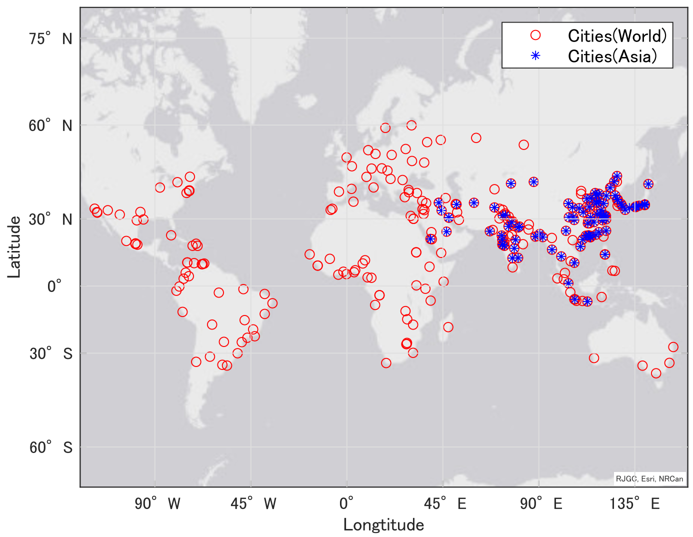

Figure 2.14: Candidate cities.

2.6 Optimization results

The optimization results for 292 cities in the entire world are shown in Table 2.7, and those for 99 Asian cities are shown in Table 2.8. The satellite altitude of each optimal constellation is obtained from N, m, and Eq. (2.32). Consider Sols. 1, 4, and 5 of Table. 2.7, solutions with different numbers of the orbital plane. The orbital plane configuration and histograms of the maximum waiting time, mean waiting time, and number of observation windows for each candidate city are shown in Figs. 2.15(a) - 2.17(d).

Table 2.7: Pareto-optimal solutions (World).

	θ_{az} [deg]	N	m	τ	N_{sat}	Altitude [km]	$-f_1 = P$	f_2 (observation windows)	f_3 (Maximum waiting time) [h]	f_4 (ΔV) [10^{-3}m/s]
Sol. 1	-0.183	5	73	6	30	687.44	1	3689	12.037	4.004
Sol. 2	0.136	7	102	4	28	696.69	1	3530	12.029	3.475
Sol. 3	-0.663	5	73	3	30	687.44	2	1847	11.141	4.004
Sol. 4	0.0330	7	102	2	28	696.69	2	1772	11.135	3.475
Sol. 5	0.882	7	102	2	28	696.69	2	1765	11.128	3.475
Sol. 6	-0.944	5	73	2	30	687.44	3	1271	4.961	4.004
Sol. 7	-1.019	5	73	2	30	687.44	3	1253	4.995	4.004

Consider Sol. 1, 4, 5, and 7 of Table. 2.8, solutions with different numbers of the orbital plane. The orbital plane configuration and histograms of the maximum waiting

	θ_{az} [deg]	N	m	τ	N_{sat}	Altitude [km]	$-f_1 = P$	f_2 (observation windows)	f_3 (Maximum waiting time) [h]	f_4 (ΔV) [10^{-3}m/s]
Sol. 1	-0.183	5	73	6	30	687.44	1	3689	12.037	4.004

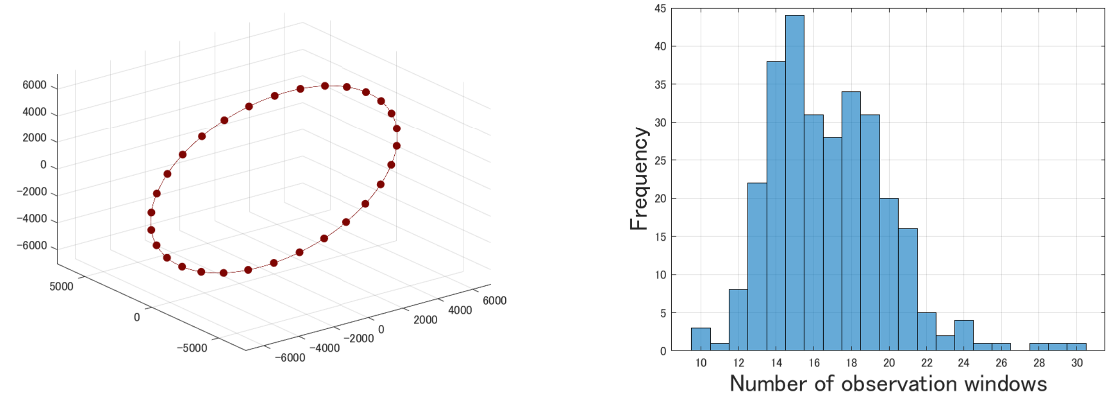

(a)Orbital plane configuration (b)The number of observation windows

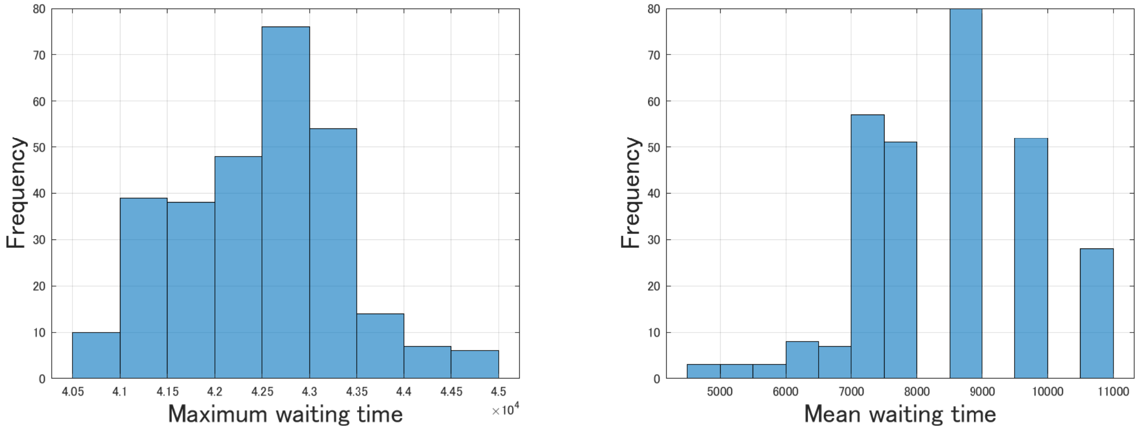

(c)Maximum waiting time (d)Mean waiting time

Figure 2.15: The detail of the optimization result(World, $P = 1$).

	θ_{az} [deg]	N	m	τ	N_{sat}	Altitude [km]	$-f_1 = P$	f_2 (observation windows)	f_3 (Maximum waiting time) [h]	f_4 (ΔV) [10^{-3}m/s]
Sol. 3	-0.663	5	73	3	30	687.44	2	1847	11.141	4.004

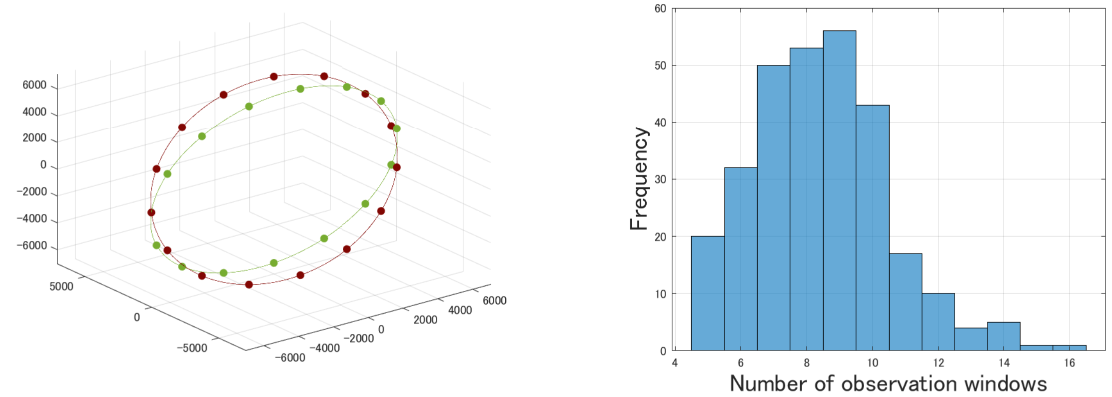

(a)Orbital plane configuration (b)The number of observation windows

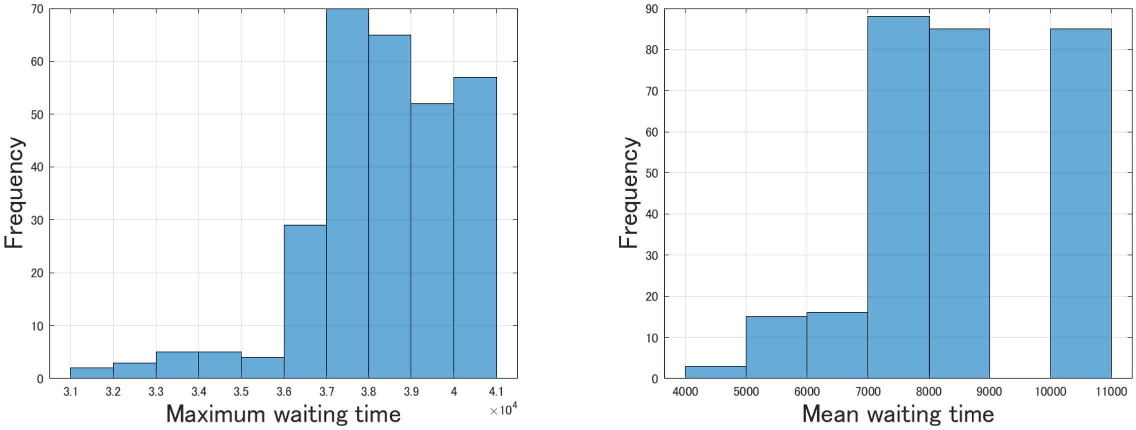

(c)Maximum waiting time (d)Mean waiting time

Figure 2.16: The detail of the optimization result(World, $P = 2$).

	θ_{az} [deg]	N	m	τ	N_{sat}	Altitude [km]	$-f_1 = P$	f_2 (observation windows)	f_3 (Maximum waiting time) [h]	f_4 (ΔV) [10^{-3}m/s]
Sol. 6	-0.944	5	73	2	30	687.44	3	1271	4.961	4.004

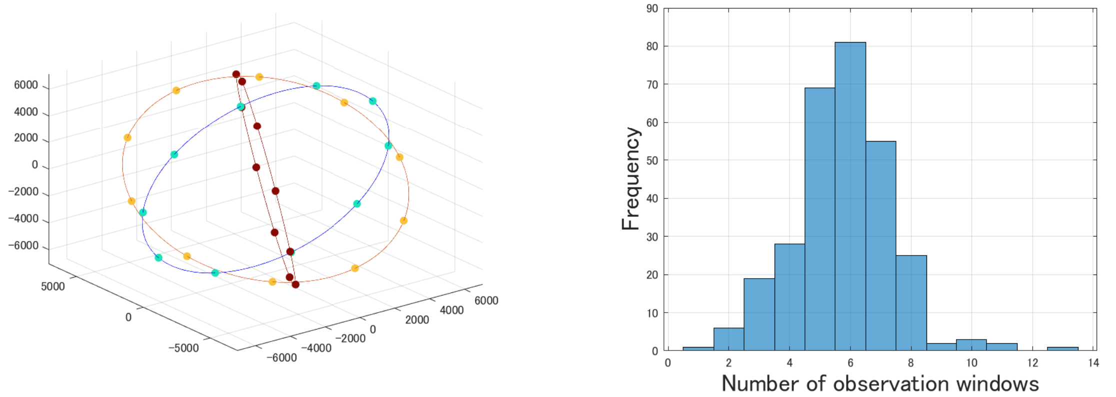

(a)Orbital plane configuration (b)The number of observation windows

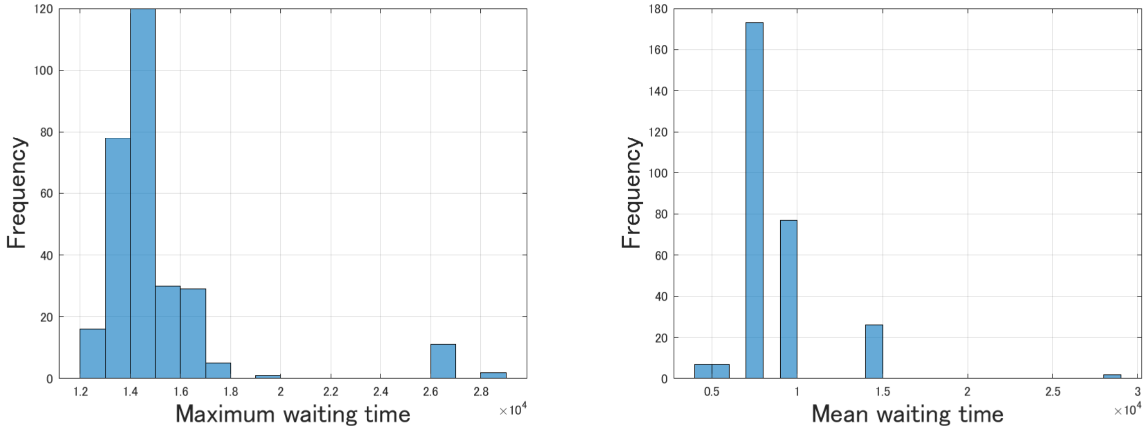

(c)Maximum waiting time (d)Mean waiting time

Figure 2.17: The detail of the optimization result(World, $P = 3$).

Table 2.8: Pareto-optimal solutions (Asia).

	θ_{az} [deg]	N	m	τ	N_{sat}	Altitude [km]	$-f_1 = P$	f_2 (observation windows)	f_3 (Maximum waiting time) [h]	f_4 (ΔV) [10^{-3}m/s]
Sol. 1	0.380	30	437	1	30	698.24	1	1280	11.985	3.387
Sol. 2	-0.103	16	233	1	16	699.60	1	693	12.024	3.310
Sol. 3	0.205	5	73	3	30	687.44	2	626	10.912	4.004
Sol. 4	-0.749	7	102	2	28	696.69	2	604	10.915	3.475
Sol. 5	-1.233	5	73	2	30	687.44	3	439	5.288	4.004
Sol. 6	-1.191	5	73	2	30	687.44	3	436	5.197	4.004
Sol. 7	-1.083	5	73	2	30	687.44	3	434	4.864	4.004
Sol. 8	-0.913	5	73	2	30	687.44	3	425	4.740	4.004
Sol. 9	0.355	5	73	2	30	687.44	3	413	4.653	4.004
Sol. 10	0.461	7	103	1	28	650.73	4	262	5.741	6.116

time, mean waiting time, and number of the observation windows for each candidate city are shown in Figs. 2.18(a) - 2.21(d).

	θ_{az} [deg]	N	m	τ	N_{sat}	Altitude [km]	$-f_1 = P$	f_2 (observation windows)	f_3 (Maximum waiting time) [h]	f_4 (ΔV) [10^{-3}m/s]
Sol. 1	0.380	30	437	1	30	698.24	1	1280	11.985	3.387

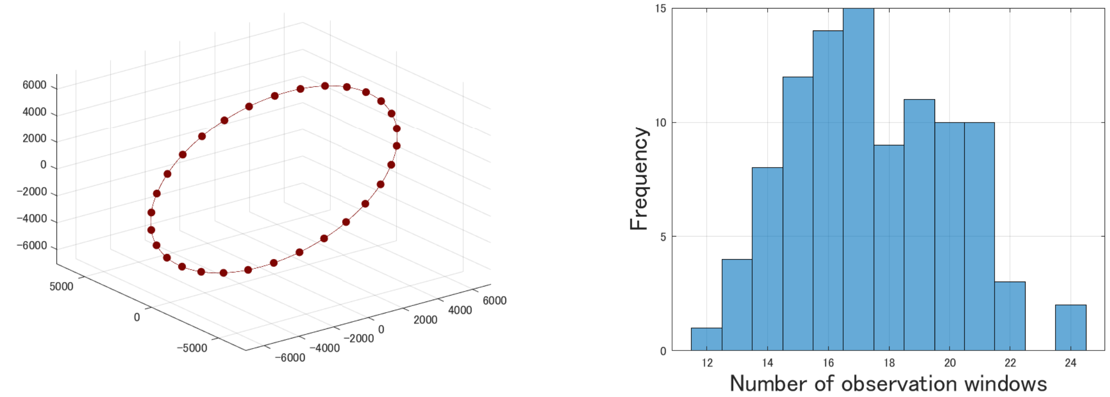

(a)Orbital plane configuration (b)The number of observation windows

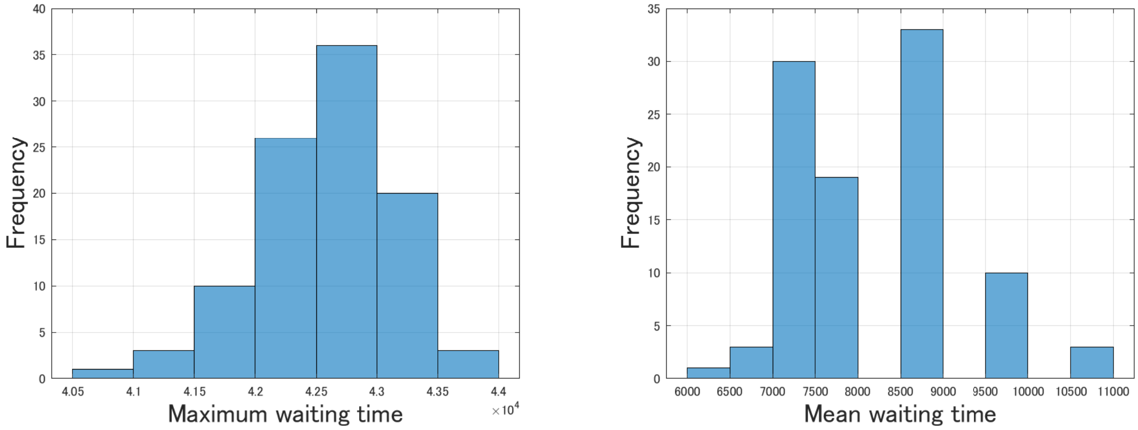

(c)Maximum waiting time (d)Mean waiting time

Figure 2.18: The detail of the optimization result(Asia, $P = 1$).

	θ_{az} [deg]	N	m	τ	N_{sat}	Altitude [km]	$-f_1 = P$	f_2 (observation windows)	f_3 (Maximum waiting time) [h]	f_4 (ΔV) [10^{-3}m/s]
Sol. 4	-0.749	7	102	2	28	696.69	2	604	10.915	3.475

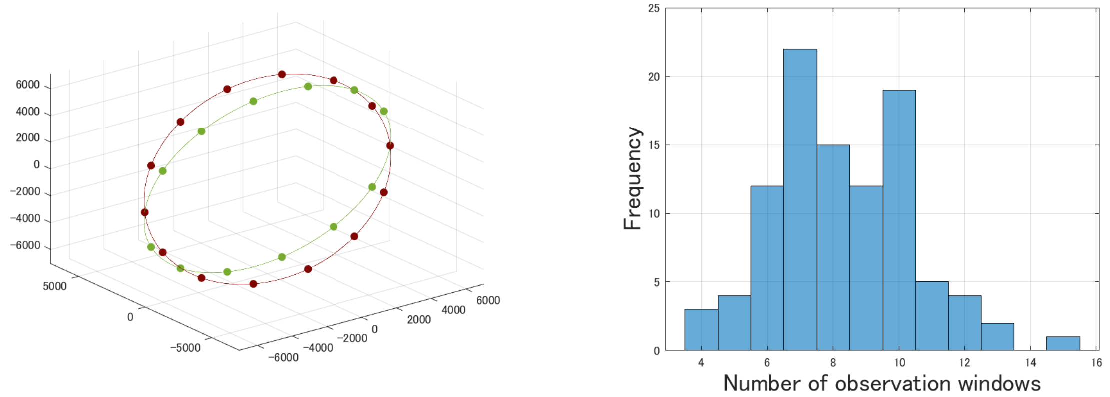

(a)Orbital plane configuration (b)The number of observation windows

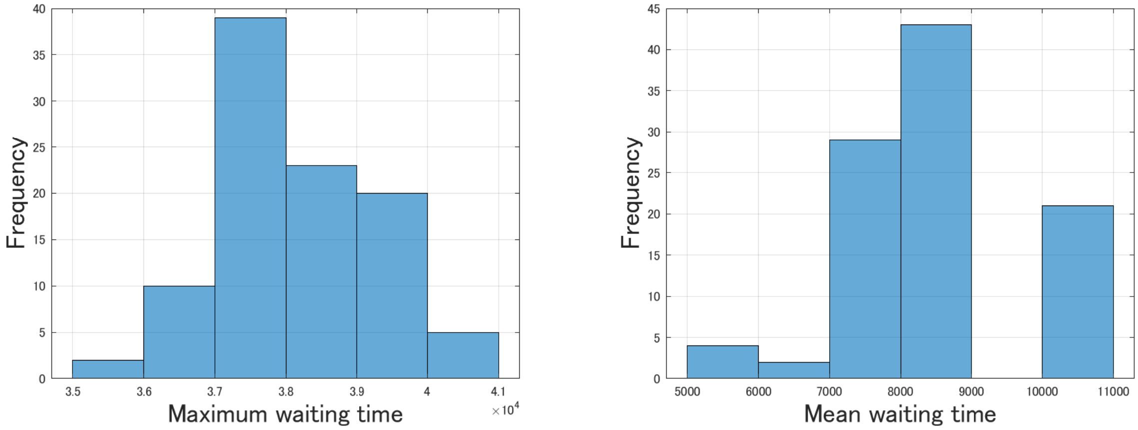

(c)Maximum waiting time (d)Mean waiting time

Figure 2.19: The detail of the optimization result(Asia, $P = 2$).

	θ_{az} [deg]	N	m	τ	N_{sat}	Altitude [km]	$-f_1 = P$	f_2 (observation windows)	f_3 (Maximum waiting time) [h]	f_4 (ΔV) [10^{-3}m/s]
Sol. 5	-1.233	5	73	2	30	687.44	3	439	5.288	4.004

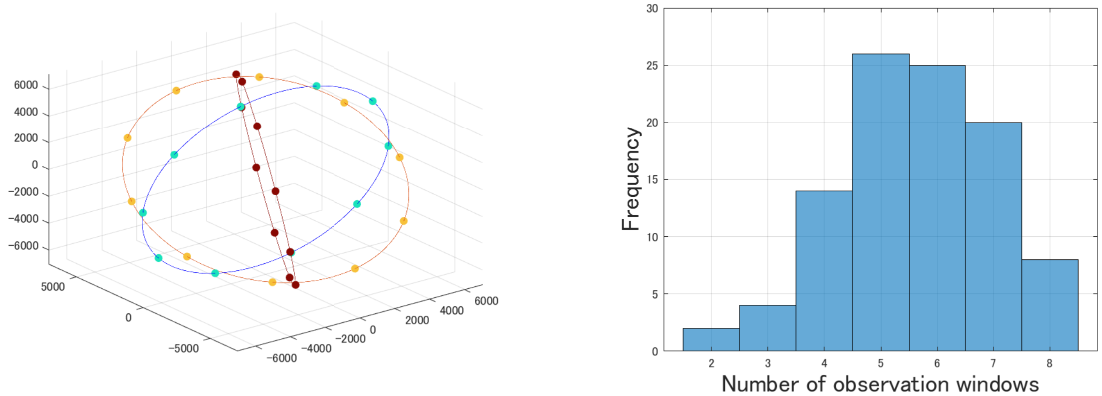

(a)Orbital plane configuration (b)The number of observation windows

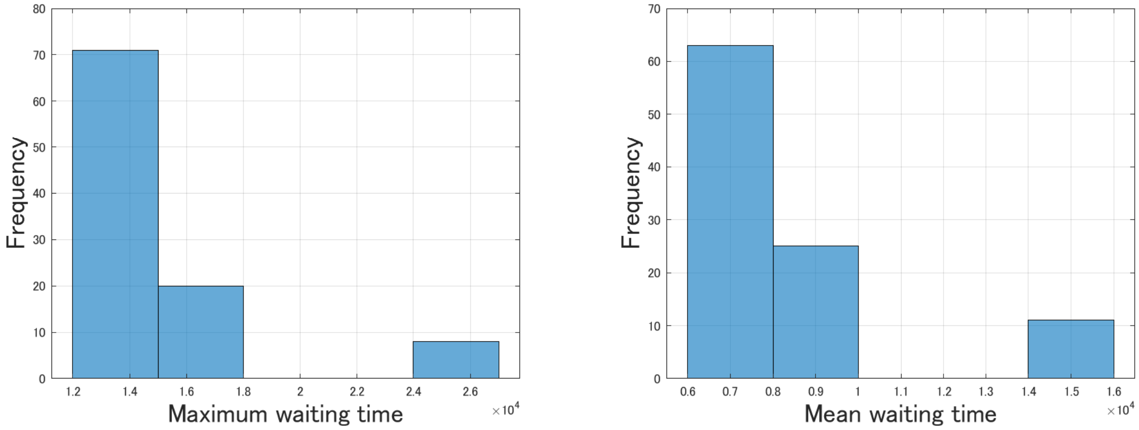

(c)Maximum waiting time (d)Mean waiting time

Figure 2.20: The detail of the optimization result(Asia, $P = 3$).

	θ_{az} [deg]	N	m	τ	N_{sat}	Altitude [km]	$-f_1 = P$	f_2 (observation windows)	f_3 (Maximum waiting time) [h]	f_4 (ΔV) [10^{-3}m/s]
Sol. 10	0.461	7	103	1	28	650.73	4	262	5.741	6.116

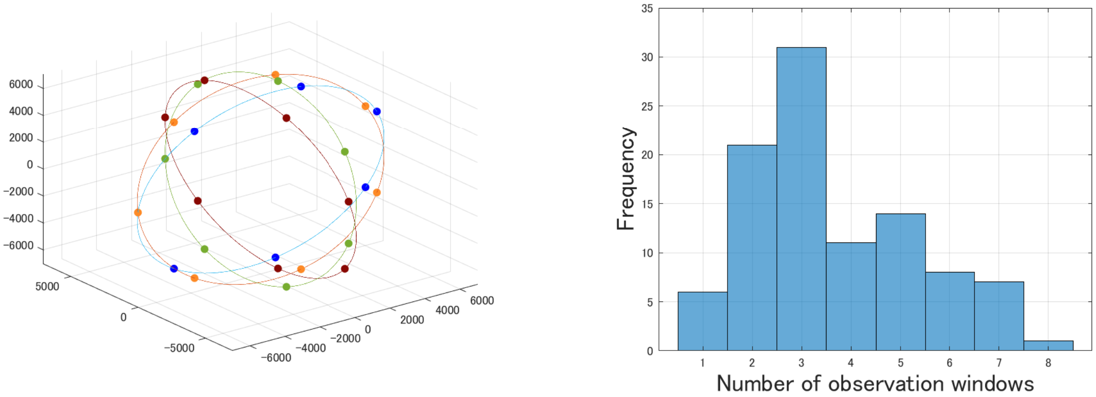

(a)Orbital plane configuration (b)The number of observation windows

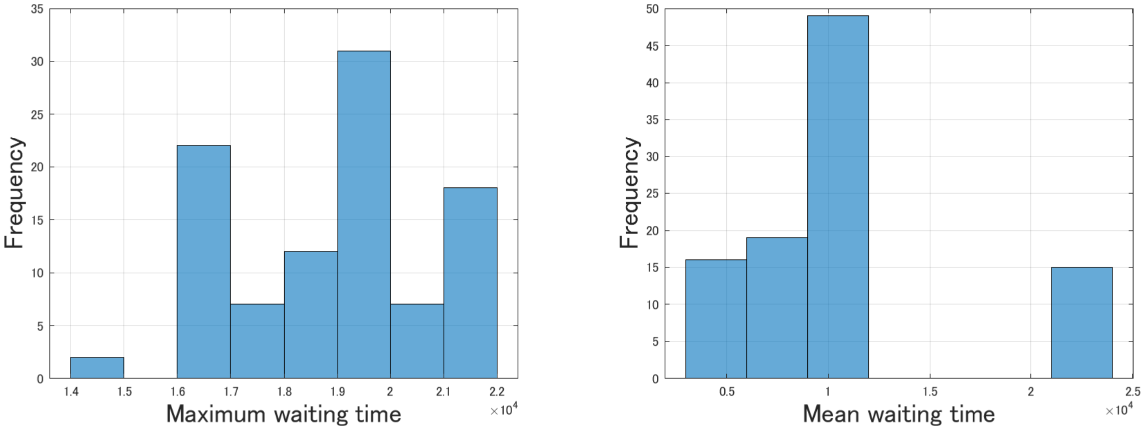

(c)Maximum waiting time (d)Mean waiting time

Figure 2.21: The detail of the optimization result(Asia, $P = 4$).

2.7 Discussion

Tables 2.7 and 2.8 show that the maximum waiting time and the number of observation windows tend to decrease as the number of orbital planes increases. In other words, there is generally a trade-off relation between the number of InSAR imaging opportunities and the InSAR observation frequency or the required waiting time. However, as an exception, only in the case of $P = 4$ for Asia, the values of all the objective functions except the number of orbital planes are worse than in the case of $P = 3$. This is because, from Eq. (2.50), achieving global coverage with a smaller number of ground tracks and repeat cycles is needed when the number of orbital planes is set as four. Therefore, there is no room to improve other objective functions in such a narrow possible range of design parameters. From above, the frequency of InSAR imaging and mission robustness, i.e., short imaging latency, are not always compatible. Next, the histograms of the maximum waiting time and the mean waiting time are compared. They show almost the same trend in some conditions like Fig. 2.17. On the contrary, there are some conditions in which the shape of the historam does not coincide, such as Figs. 2.15 and 2.21. These facts show that the trend of the maximum waiting time does not entirely coincide with the trend in the mean waiting time and the number of observation windows. We can say that increasing the number of observation windows alone is not enough to improve mission robustness. Therefore, the robustness of the constellation for the emergency mission and the mission scheduling flexibility for regular missions must be evaluated separately. This result shows the necessity of the objective function f_2 that evaluates the robustness of the mission.

Comparing Sols. 1 and 2 for both conditions and Sols. 3 and 4 for the World, the number of the observation windows tends to be larger when τ and N are large. There are two possible approaches to increasing the number of observation windows.

- Increasing P to improve the revisit frequency to the same position
- Increasing N and τ to expand the coverage area of the ground track

P, N, and τ are constrained by the relation $N\tau P \leqq N_{\mathrm{sat,max}}$. Therefore, the optimal combination of these three elements must be considered. The solution with $N = 5$ and $\tau = 6$ takes the best value of f_2 when the entire World is observed. Therefore, increasing τ effectively expands the coverage area in this condition. On the contrary, since the solution with $N = 30$ and $\tau = 1$ takes the best f_2 in the case of Asia, taking the larger value of N is effective in expanding the imaging possibilities of the target cities in Asia. As these results show, the factors that strongly affect the imageability depend on the distribution of observation targets of the mission. It is shown that the proposed method can be used to obtain optimal constellation configurations that reflect the different mission settings and requirements.

In addition, when observation targets are limited to Asia, $P = 4$ can be achieved, and 4 InSAR imaging in one day is possible. However, in the case of the entire world, the solution with $P = 4$ cannot be achieved. This difference can be attributed to the difficulty of global coverage. When the entire world is observed, it is more difficult to ensure global coverage than in the case of Asia. Therefore, the larger N and τ are needed to expand the coverage area. Then, P is strongly constrained by $N\tau P \leqq N_{\text{sat,max}}$ and $P = 4$ becomes impossible.

For both target conditions, most of the Pareto-optimal orbits are set at the higher 600 km altitude, near the upper bounds of the altitude. There are two possible reasons for this. The first reason is the effect of minimizing fuel consumption as the objective function f_4. The other reason is that the high altitude expand the field of view [12, 21]. Therefore, the high altitude is also adequate for increasing the number of observation windows. Moreover, especially in the case of Asia, the solutions with fewer orbital planes tend to have a higher altitude, and those with more orbital planes tend to have a lower altitude. This is likely due to the relationship between the distribution of possible (N, m) values and altitudes. Figure 2.13 shows that the larger the value of N, the larger the number of possible altitudes, and it becomes easier to obtain a high-altitude solution. However, since N and m must be prime to each other in the constraint condition, there are some exceptions. For example, $(N, m) = (14, 204)$ (altitude: 696.7 km) can be treated as the same orbit as $(N, m) = (7, 102)$. Then it is omitted from the $N = 14$ column in Fig. 2.13. In the case of Asia, the first and third orbital conditions of Table 2.6 are used in the solution of $P = 1$. Since $N_{\text{sat,max}} = 30$ in this research, from Eq. (2.51), it is impossible to take more than one orbital plane for the top three constellation configurations of Table 2.6. The pair of (N, m) with the largest altitude that can take more than one orbital plane is $(N, m) = (7, 102)$, which is adopted in many solutions with two orbital planes in both conditions. The solution with $(N, m) = (5, 73)$, which is adopted in the solutions with three orbital planes, takes the second-highest altitude among the solutions with less than ten repeat cycles; that is, solutions with at least three orbital planes are possible. Thus, it is implied that the Pareto-optimal solutions mainly select the pair of (N, m) with the highest altitude to the extent that the global coverage constraint and Eq. (2.51) are satisfied, while also taking into account the impact of τ on the number of imageable observation windows.

2.8 Conclusion to Chapter 2

In this research, an optimal constellation design method for Earth observation missions using InSAR is proposed. First, the analytical orbit model was constructed to calculate the time variation of orbital elements at a low computational cost. The validity of that model is demonstrated by comparing it with the numerical simulation. First, requirements for satellite orbital elements to carry out observation missions properly and effectively, i.e., repeating Sun-synchronous orbit, have been formulated. Next, the method for the satellite's ground track has been described. Then, the conditions for multiple satellites to follow the same ground track to improve the InSAR observation frequency have been formulated. They are formulated separately for satellites in one orbital plane and different orbital planes. Then, the optimal constellation design problem has been mathematically formulated as a nonlinear mixed-integer programming problem. This problem has been solved using ant colony optimization, a multi-objective optimization method, from the perspective of the number of orbital planes, the number of observation windows, maximum waiting time, and fuel consumption. The optimization calculation has been conducted under two mission conditions; observing cities all over the world or cities only in Asia. As a result of the optimization, a set of Pareto-optimal solutions consisting of multiple constellation configurations with trade-off relations have been obtained for both mission conditions.

From the Pareto-optimal solutions, it has been found that the best solution is to obtain as high an altitude as possible while satisfying the number of orbital planes and coverage constraints. The comparison of the two observation conditions has shown several differences in trends. First, the Asian case has provided solutions with better mission robustness and design flexibility. Furthermore, only in the case of Asia, a solution with four orbital planes has been obtained, which means that four InSAR observations can be achieved in one day. The reason for these trends is thought to be the difference in difficulty in achieving global coverage between observing the entire world and only Asia. These results confirm that the proposed method can provide optimal constellation configurations adapted to the given mission conditions. The proposed method can be applied to various observation requirements and mission settings by giving a different list of candidate cities.

Chapter 3

Constellation deployment control with atmospheric drag

3.1 Satellite Orbit Dynamics

This chapter focuses on the in-plane deployment of launched satellites. The effect of atmospheric drag can be adjusted by moving the attitude of the satellite or rotating the solar panel. From Gauss's planetary equations, if the altitude decrease caused by the atmospheric drag can be properly controlled, in-plane constellation deployment can be achieved only by atmospheric drag without fuel. Therefore, this research proposes an atmospheric drag-based feedback control law for constellation in-plane deployment. From the simplified orbit dynamics, optimal cross-section trajectories of satellites for the constellation deployment is calculated by the nonlinear optimization. Using obtained trajectories as reference trajectories, cross-section trajectories and resulting orbit trajectories are analytically formulated. Then, a feedback control law with regular updates of analytical solutions is constructed and the efficiency is verified by the numerical simulation.

3.1.1 Problem settings

To express the satellite dynamics, Gauss's planetary equations shown in Chapter 2 is used. From Eqs. (2.2) - (2.8), the time derivative of each orbital element is affected by some of the other orbital elements. Therefore, if the transitions of these orbital elements are designed appropriately, the desired constellation configuration can be achieved. From Gauss's planetary equations (Eqs. (2.2) - (2.8)) and Eqs. (2.11) - (2.13), the effect of J_2 perturbation on a, e, and i is canceled in one orbit cycle. Therefore, it is assumed that a, e, and i do not change with the effect of the J_2 perturbation. In addition, from Eqs. (2.5)

- (2.8), the time derivative of Ω is much smaller than that of $\theta = f + \omega$ [51, 52]. Since satellite constellation deployment in one orbital plane is considered in this chapter, Ω is assumed to be constant. Then, the trajectory of one satellite in the constellation can be determined from two orbital elements, a and θ.

Next, let $\boldsymbol{F}_{\text{drag}}$ be the external force due to the atmospheric drag. When $\boldsymbol{v}$ is the velocity vector of the satellite and $v = |\boldsymbol{v}|$, $\boldsymbol{F}_{\text{drag}}$ is formulated as follows:

$$\boldsymbol{F}_{\text{drag}} = -\frac{\rho C_d A v^2}{2m_{\text{sat}}}\hat{\boldsymbol{s}}, \tag{3.1}$$

where ρ is assumed to be constant in this research. Although the effect of the J_2 on the semi-major axis a is neglected, the effect of the atmospheric drag on a is considered in this research. When the effect of the atmospheric drag is considered, $\hat{\boldsymbol{r}}$, $\hat{\boldsymbol{s}}$, and $\hat{\boldsymbol{h}}$ components of $\boldsymbol{F}_{\text{drag}}$ are used as F_r, F_s, and F_h in Eqs. (2.2) - (2.8).

3.1.2 Simplified orbit dynamics

When assumptions shown in the previous section are applied to Eqs. (2.2), (2.6), and (2.8), the simplified satellite orbit dynamics considering the effect of the J_2 perturbation and atmospheric drag is expressed as follows:

$$\dot{a} = \frac{C_d \rho A \sqrt{\mu}}{m_{\text{sat}}}, \tag{3.2}$$

$$\dot{\theta} = \sqrt{\mu} a^{-\frac{3}{2}} - \frac{3\pi J_2 {R_e}^2}{2}(1 - 4\cos^2 i)\sqrt{\mu} a^{-\frac{7}{2}}, \tag{3.3}$$

where the circular orbit ($e = 0$) is assumed. In actual operation, A in Eq. (3.2) is manipulated by the satellite attitude maneuver, a and θ change accordingly. In this way, the atmospheric drag can be used to change satellite orbits without fuel consumption. The optimal A transitions to achieve the desired in-plane constellation configuration are discussed in the next section.

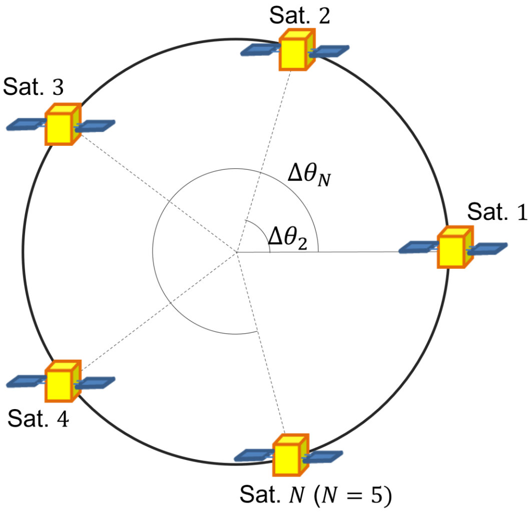

Figure 3.1: Constellation configuration for $N = 5$.

3.2 Maneuver Optimization

3.2.1 Problem definition

In this research, N satellites are assumed to be launched at the same position in a circular orbit. The orbit of each satellite is changed through its attitude maneuver. Finally, all satellites are evenly distributed in one orbital plane with the same semi-major axis. Among N satellites of a constellation in one orbital plane, one satellite is designated as Sat. 1, which is the reference satellite. Then, starting from the satellite with the smallest in-plane phase difference to Sat. 1, Sat. 2 to Sat. N are defined. Figure 3.1 shows the final constellation configuration for $N = 5$, where $\Delta\theta_j$ in the figure is the desired in-plane phase difference of satellite j from the reference satellite. The orbit semi-major axis and the argument of latitude at time t of the satellite j are described as $a_j(t)$ and $\theta_j(t)$, respectively. Then, the requirements on a_j and θ_j at the deployment ending time t_f are expressed as follows:

$$a_1(t_f) = a_2(t_f) = \cdots = a_N(t_f), \tag{3.4}$$

$$\theta_{j+1}(t_f) - \theta_j(t_f) = \frac{2\pi}{N} \quad (j = 1, 2, \cdots, N-1). \tag{3.5}$$

3.2.2 Normalized dynamics

To accelerate the convergence of the nonlinear maneuver optimization, semi-major axis a and time t are normalized. Normalized parameters $\bar{a}$ and τ are expressed in the following manner:

$$\bar{a} = \frac{a}{a_0}, \tag{3.6}$$

$$\tau = \sqrt{\frac{\mu}{{a_0}^3}} t, \tag{3.7}$$

where a_0 is the semi-major axis of the desired constellation. Then, using normalized parameters, Eqs. (3.2) and (3.3) can be rewritten in the following way:

$$\frac{\mathrm{d}\bar{a}}{\mathrm{d}\tau} = -\beta\sqrt{\bar{a}}, \tag{3.8}$$

$$\frac{\mathrm{d}\theta}{\mathrm{d}\tau} = \bar{a}^{-\frac{3}{2}} + \bar{P}\bar{a}^{-\frac{7}{2}}, \tag{3.9}$$

where $\beta = C_d a_0 \rho A / m_{\mathrm{sat}}$ and $\bar{P} = -3\pi J_2 {R_e}^2 (1 - 4\cos^2 i)/(2{a_0}^2)$. In addition, the normalized parameter α ($-1 \leqq \alpha \leqq 1$) is introduced instead of A. Between α and A, the following relation holds:

$$A = \frac{(A_{\max} + A_{\min})}{2} + \alpha \frac{(A_{\max} - A_{\min})}{2}, \tag{3.10}$$

where $A_{\max}$ and $A_{\min}$ are the maximum and minimum values of A, respectively.

3.2.3 Optimization using DCNLP

Direct collocation with nonlinear programming (DCNLP) [53] is used as a trajectory optimization method. DCNLP is an optimization method that designs time transitions of inputs and state variables using the equations of motion and initial and terminal conditions as constraints. In this research, the input is the cross-section for each satellite and each time. Moreover, the state variables are a and θ. In addition to the input and state variables, normalized total deployment time τ_f is also optimized as a design parameter. When the deployment time is divided equally into T time steps and the number of satellites is N, state $y_{j,k}$ and input $u_{j,k}$ for Sat. j ($1 \leqq j \leqq N$) at the kth time step ($1 \leqq k \leqq T$) are described in the following manner:

$$y_{j,k} = [\bar{a}_{j,k}, \theta_{j,k}], \tag{3.11}$$

$$u_{j,k} = \alpha_{j,k}. \tag{3.12}$$

Using the above $y_{j,k}$ and $u_{j,k}$, Eqs. (3.8) and (3.9) can be rewritten as shown in Eq. (3.13)

$$\dot{y}_{j,k} = f(y_{j,k}, u_{j,k}). \tag{3.13}$$

The design parameter $\boldsymbol{x}$ of the DCNLP has the $3NT + 1$ variables shown below:

$$\begin{aligned} \boldsymbol{x} &= [\boldsymbol{z}_1, \cdots, \boldsymbol{z}_T, \tau_f], \\ \boldsymbol{z}_k &= [y_{1,k}, u_{1,k}, \cdots y_{N,k}, u_{N,k}]. \end{aligned} \tag{3.14}$$

As the constraint condition, a and θ in each j and k must satisfy Eq. (3.13). To adopt equations of motion in the constraints of DCNLP, the equations are discretized using the Hermite-Simpson Collocation [54]. When Eqs. (3.8) and (3.9) are discretized with Hermite- Simpson Collocation, constraints of equations of motion are described as the following equations for $1 \leqq j \leqq N$ and $1 \leqq k \leqq T-1$:

$$\begin{aligned} y_{j,k+1} &- y_{j,k} = \frac{f(y_{j,k+1}, u_{j,k+1}) + 4\bar{f}_{j,k} + f(y_{j,k}, u_{j,k})}{6} \mathrm{d}\tau, \\ \bar{f}_{j,k} &= f\left(\frac{y_{j,k} + y_{j,k+1}}{2} - \frac{\Delta f_{j,k}}{8}\mathrm{d}\tau, \frac{u_{j,k+1} + u_{j,k}}{2}\right), \\ \Delta f_{j,k} &= f(y_{j,k+1}, u_{j,k+1}) - f(y_{j,k}, u_{j,k}), \\ \mathrm{d}\tau &= \frac{\tau_f}{T} = \frac{x(3NT+1)}{T}. \end{aligned} \tag{3.15}$$

In addition, the initial and final constraints are expressed as follows:

$$\bar{a}_{1,1} = \bar{a}_{2,1} = \cdots = \bar{a}_{N,1}, \quad \theta_{j,1} = 0, \tag{3.16}$$

$$\bar{a}_{j,T} = 1, \quad \theta_{j,T} - \theta_{1,T} - \frac{2\pi(j-1)}{N} = 0, \tag{3.17}$$

where values of $\bar{a}$ and θ of Sat. j in time step k are denoted as $\bar{a}_{j,k}$ and $\theta_{j,k}$, respectively. In this research, the objective function of DCNLP is the minimization of the altitude decrease during the deployment. Since the final altitude is fixed, it can be achieved by minimizing the initial altitude, which requires less fuel for launch. Therefore, this objective function is reasonable to improve the launch efficiency. Considering Eqs. (3.16) and (3.17), the objective function of DCNLP $f_{\mathrm{obj,opt}}$ is described as follows:

$$f_{\mathrm{obj,opt}} = \bar{a}_1(0) - \bar{a}_1(\tau_f) = \bar{a}_1(0) - 1. \tag{3.18}$$

The optimization is performed using the orbit and satellite conditions shown in Table 3.1.

Table 3.1: Optimization conditions.

Parameter	Symbol	Value	Unit
Initial semi-major axis	a_0	6788.8	km
Orbial inclination angle	i	97.07	deg
Number of satellites	N	10	-
Satellite mass	m_{sat}	4.9	kg
Maximum cross-section	A_{max}	2.25×10^{-1}	m^2
Minimum cross-section	A_{min}	3.71×10^{-2}	m^2
Drag coefficient	C_d	2.2	-
Atmospheric density	ρ	2.459×10^{-3}	kg/km^3
Number of time step	T	500	-

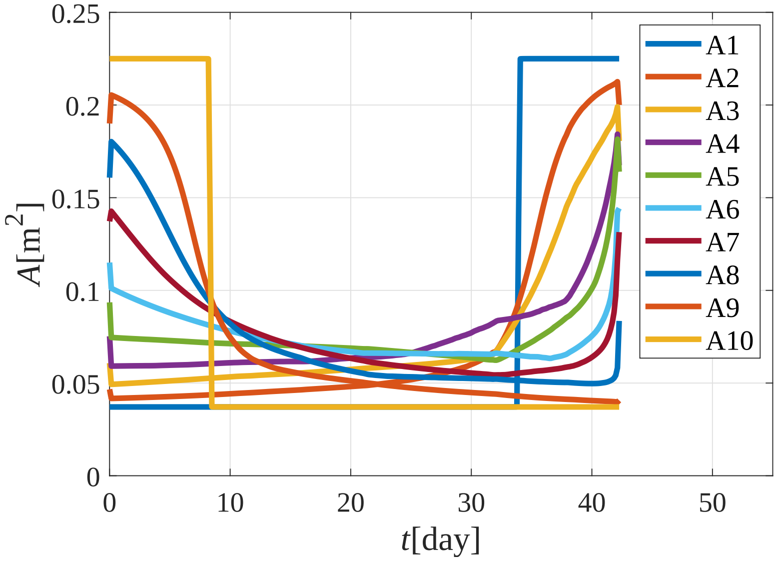

Figure 3.2: Optimal trajectories of cross-section A.

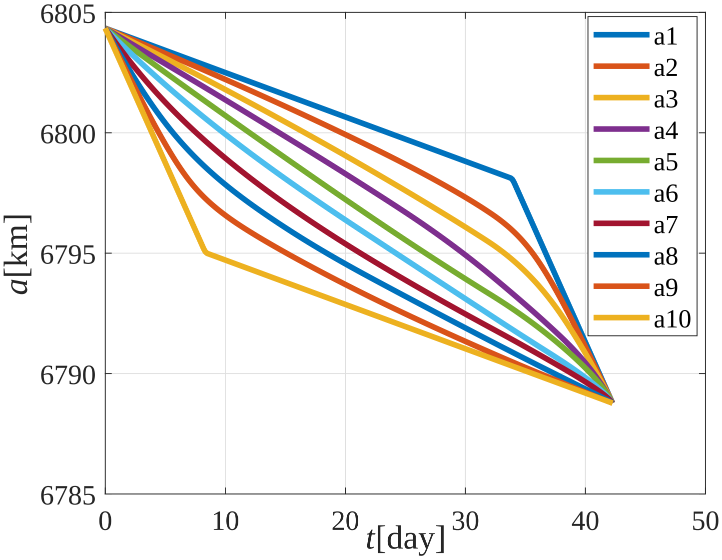

Figure 3.3: Optimal trajectories of semi-major axis a.

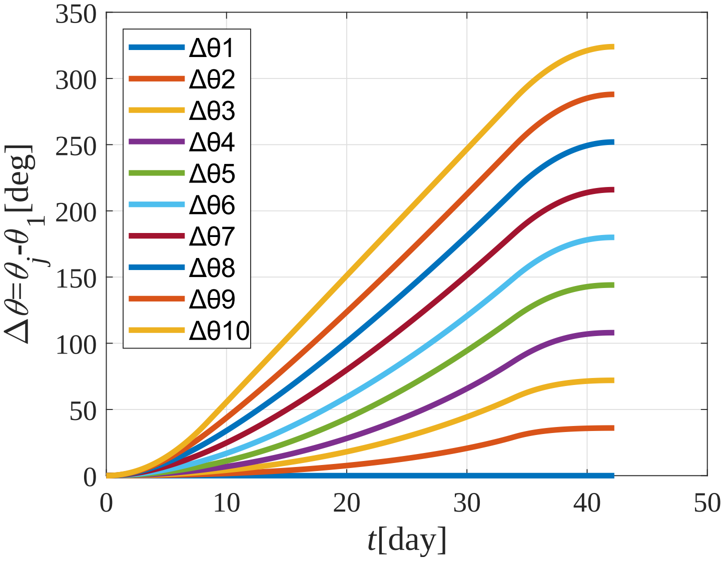

Figure 3.4: Optimal trajectories of the constellation deployment maneuver.

Optimal trajectories of cross-section A, semi-major axis a, and in-plane phase difference from Sat. 1 are shown in Figs. 3.2 - 3.4.

From Fig. 3.2, it can be seen that Sat. 1 and Sat. N switches the maximum and minimum cross-section during the deployment. In addition, other satellites also perform a switch from the small A to the large A, or vice versa. Moreover, Fig. 3.3 shows that all satellites take the same a at final time t_f, and Fig. 3.4 shows that the phase difference of each satellite from Sat. 1 is increasing evenly. Therefore, it can be said that the optimal attitude maneuver and trajectories of a and θ have been obtained from DCNLP.

3.3 Analytical Formulation of the In-Plane Constellation Deployment Maneuver

In the optimal design of the satellite constellation, thousands of calculations must be performed to evaluate the cost and performance of the constellation [13, 55]. In addition, for real-time orbit control, orbit transitions must be calculated at a low computational cost because of the limited performance of on-board satellite computers. Therefore, analytical solutions of the normalized deployment time τ_f and the trajectories of a, θ, and A are needed. Thus, in this section, a simplified satellite maneuver to achieve the desired constellation configuration is modeled. First, from the tendency of the obtained analytical maneuver, analytical trajectory models of A, a, and θ are formulated. From the analytical models for Sat. 1 and Sat. N, the total deployment time τ_f is obtained. Using τ_f, parameters to determine other satellites' trajectories of A, a, and θ are calculated.

3.3.1 Cross-section trajectory model

Based on the tendency of optimal trajectories of the cross-section shown in the previous section, the optimal cross-section trajectory of the satellite j is formulated as the two-phase maneuver model shown in Eq. (3.19) and Fig. 3.5:

$$\begin{aligned}
\beta &= \begin{cases} \beta_2 & (0 \leqq \tau \leqq (1-\gamma)\tau_f) \\ \beta_1 & ((1-\gamma)\tau_f < \tau \leqq \tau_f) \end{cases} (0 \leqq \Delta\theta_j < \pi)\,, \\
\beta &= \begin{cases} \beta_1 & (0 \leqq \tau \leqq \gamma\tau_f) \\ \beta_2 & (\gamma\tau_f < \tau \leqq \tau_f) \end{cases} (\pi \leqq \Delta\theta_j < 2\pi)\,, \\
\beta_1 &= \frac{\beta_{\max}+\beta_{\min}}{2} + \alpha_1\frac{\beta_{\max}-\beta_{\min}}{2}, \quad \beta_2 = \frac{\beta_{\max}+\beta_{\min}}{2} - \alpha_2\frac{\beta_{\max}-\beta_{\min}}{2},
\end{aligned} \tag{3.19}$$

where β_1 and β_2 take different values for each satellite. The trajectory model of the cross-section depends on the desired in-plane phase difference $\Delta\theta_j$. α_1 and α_2 determine the cross-section that each satellite takes. The switching timing of the cross-section is determined by γ, which is common to all satellites.

3.3.2 Analytical formulation of the orbit trajectories

Trajectories of $\bar{a}$ and θ when the satellite takes the cross-section transition shown in Eq. (3.19) are formulated here. At the initial time $\tau = 0$, θ's of all satellites are assumed to be 0. In addition, at the final time $\tau = \tau_f$, $\bar{a}$'s of all satellites are assumed to be 1. Then,

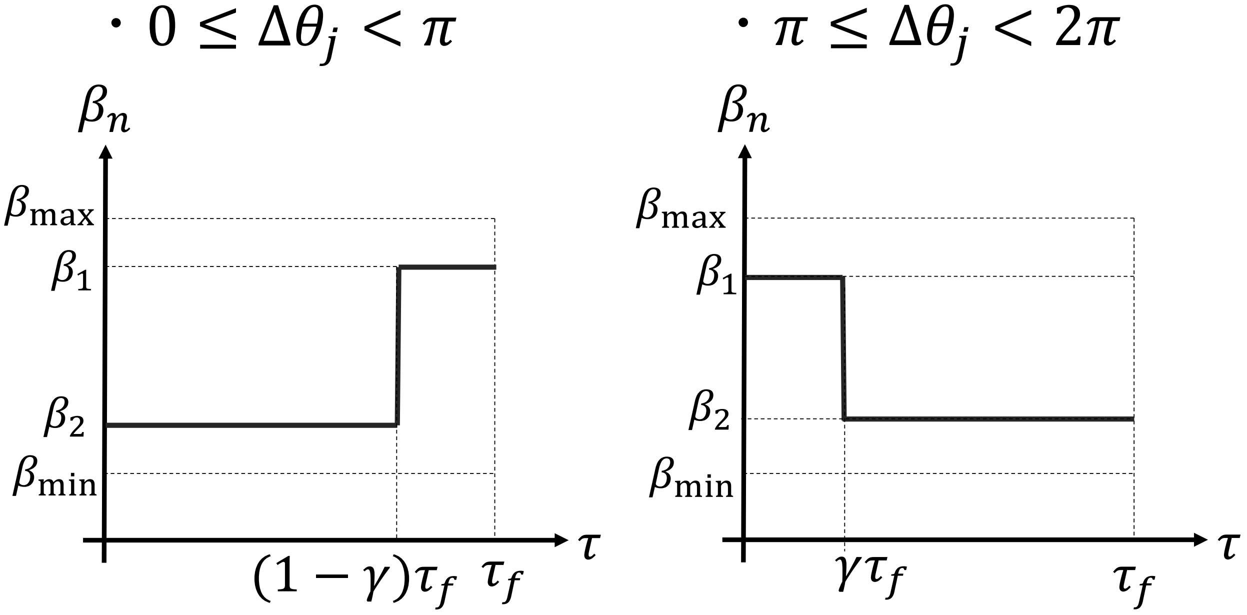

Figure 3.5: Two-phase cross-section trajectory model.

from Eq. (3.8), the trajectory of $\bar{a}$ is analytically formulated as shown in Eqs. (3.20) and (3.21):

$$\sqrt{\bar{a}(\tau)} = \begin{cases} 1 + \frac{\beta_2}{2}(\tau_f - \tau) + \frac{\beta_1 - \beta_2}{2}\gamma\tau_f \quad (0 \leqq \tau \leqq (1-\gamma)\tau_f) \\ 1 + \frac{\beta_1}{2}(\tau_f - \tau) \quad ((1-\gamma)\tau_f < \tau \leqq \tau_f) \end{cases} \qquad (0 \leqq \Delta\theta_j < \pi)\,, \tag{3.20}$$

$$\sqrt{\bar{a}(\tau)} = \begin{cases} 1 + \frac{\beta_1}{2}(\gamma\tau_f - \tau) + \frac{\beta_2}{2}(1-\gamma)\tau_f \quad (0 \leqq \tau \leqq \gamma\tau_f) \\ 1 + \frac{\beta_2}{2}(\tau_f - \tau) \quad (\gamma\tau_f < \tau \leqq \tau_f) \end{cases} \qquad (\pi \leqq \Delta\theta_j < 2\pi)\,. \tag{3.21}$$

From the obtained $\bar{a}$ trajectories and Eq. (3.9), the trajectory of the argument of latitude θ for satellite j $(0 \leqq \Delta\theta_j < \pi)$ can be formulated as follows:

$$\theta(\tau) = \begin{cases} \frac{1}{\beta_2}\left(1 - \frac{\beta_2}{2}\tau\right)^{-2} + \frac{\bar{P}}{3\beta_2}\left(\bar{M} - \frac{\beta_2}{2}\tau\right)^{-6} - \frac{\bar{M}^{-2}}{\beta_2} - \frac{\bar{P}\bar{M}^{-6}}{3\beta_2} & (0 \leqq \tau \leqq (1-\gamma)\tau_f) \\ \frac{1}{\beta_1}\left\{\left(\bar{L} - \frac{\beta_1}{2}\tau\right)^{-2} - \left(1 - \frac{\gamma\beta_1}{2}\tau_f\right)^{-2}\right\} & \\ +\frac{\bar{P}}{3\beta_1}\left\{\left(\bar{L} - \frac{\beta_1}{2}\tau\right)^{-6} - \left(1 - \frac{\gamma\beta_1}{2}\tau_f\right)^{-6}\right\} + \theta_1\left((1-\gamma)\tau_f\right) & ((1-\gamma)\tau_f < \tau \leqq \tau_f) \end{cases}, \tag{3.22}$$

where $\bar{M} = 1 + \beta_2/2\tau_f + (\beta_1 - \beta_2)/2\gamma\tau_f$ and $\bar{L} = 1 + \beta_1/2\tau_f$. Similarly, the trajectory of the argument of latitude θ for satellite j $(\pi \leqq \Delta\theta_j < 2\pi)$ can be formulated as follows:

$$\theta(\tau) = \begin{cases} \frac{1}{\beta_1}\left(\bar{Q} - \frac{\beta_1}{2}\tau\right)^{-2} + \frac{\bar{P}}{3\beta_1}\left(\bar{Q} - \frac{\beta_1}{2}\tau\right)^{-6} - \frac{\bar{Q}^{-2}}{\beta_1} - \frac{\bar{P}\bar{Q}^{-6}}{3\beta_1} & (0 \leqq \tau \leqq \gamma\tau_f) \\ \frac{1}{\beta_2}\left\{\left(\bar{R} - \frac{\beta_2}{2}\tau\right)^{-2} - \left(1 + \frac{(1-\gamma)\beta_2}{2}\tau_f\right)^{-2}\right\} & \\ +\frac{\bar{P}}{3\beta_2}\left\{\left(\bar{R} - \frac{\beta_2}{2}\tau\right)^{-6} - \left(1 + \frac{(1-\gamma)\beta_2}{2}\tau_f\right)^{-6}\right\} + \theta\left(\gamma\tau_f\right) & (\gamma\tau_f < \tau \leqq \tau_f) \end{cases}, \tag{3.23}$$

where $\bar{Q} = 1 + \beta_2/2\tau_f + (\beta_1 - \beta_2)/2\gamma\tau_f$ and $\bar{R} = 1 + \beta_2/2\tau_f$.

3.3.3 Parameter derivation

In this section, values of τ_f, α_1, α_2, and γ to achieve the desired constellation configuration are obtained using the analytical solutions of $\bar{a}$ and θ shown in Eqs. (3.20) - (3.23). First, the normalized deployment time τ_f is obtained from the required relation between satellite 1 (reference satellite) and satellite N (the satellite with the largest θ). $\bar{a}$, θ, and the required phase difference from satellite 1 of satellite j are denoted as $\bar{a}_j$, θ_j, and $\Delta\theta_j$, respectively. Then, for Sat. 1 and Sat. N, the following equations must be satisfied:

$$\bar{a}_1(\tau_f) = \bar{a}_N(\tau_f), \tag{3.24}$$

$$\theta_N(\tau_f) - \theta_1(\tau_f) = \Delta\theta_N. \tag{3.25}$$

In this research, all satellites in the constellation are assumed to be placed equally. Therefore, for satellite j, $\Delta\theta_j = 2\pi \times (j-1)/N$ holds. Substituting $\tau = \tau_f$ into Eqs. (3.20) and (3.21), Eq. (3.24) always holds. In addition, from Fig. 3.2 (a), satellites 1 and N take the maximum or minimum cross-section value. Thus, for satellites 1 and N, $\alpha_1 = \alpha_2 = 1$ holds. Then, by substituting Eqs. (3.22) and (3.23) into Eq. (3.25), an eighteenth-order equation of τ_f can be obtained. However, it is impossible to solve the eighteenth-order equation analytically. Since nano or micro-satellites are assumed, the order of each parameter is as follows:

$$\beta_{\max} \sim 10^{-6}, \quad \beta_{\min} \sim 10^{-7}, \quad \bar{P} \sim 10^{-3}. \tag{3.26}$$

By considering Eq. (3.26), terms of higher order than the square of $\beta_{\max}$ or $\beta_{\min}$ can be ignored. Then, τ_f can be obtained as the positive real solution of the quadratic equation shown below:

$$\begin{aligned} &p_f\tau_f^2 + q_f\tau_f + r_f = 0, && (3.27)\\ &p_f = 3\gamma(1-\gamma)(\beta_{\max} - \beta_{\min}), \quad q_f = -12\Delta\theta_N(\beta_{\max} + (1-\gamma)\beta_{\min}), \quad r_f = -2\Delta\theta_N. \end{aligned}$$

Here, $p_f > 0$, $q_f < 0$, and $r_f < 0$ hold because $0 \leq \gamma \leq 1$ and $\beta_{\max} > \beta_{\min}$. Then, considering τ_f must be larger than 0, τ_f can be calculated in the following manner:

$$\tau_f = \frac{-q_f + \sqrt{q_f^2 - 4p_fr_f}}{2p_f}. \tag{3.28}$$

From Eq. (3.26) and $0 < \gamma < 1$, $q_f^2 \ll -4p_fr_f$ holds. Therefore, the numerator of Eq. (3.28) can be approximated as $\sqrt{-4p_fr_f}$. Then, τ_f can be simplified as follows:

$$\tau_f \approx \frac{\sqrt{24\gamma(1-\gamma)(\beta_{\max} - \beta_{\min})\Delta\theta}}{6\gamma(1-\gamma)(\beta_{\max} - \beta_{\min})} = \sqrt{\frac{2\Delta\theta}{3\gamma(1-\gamma)(\beta_{\max} - \beta_{\min})}}. \tag{3.29}$$

Next, γ that determines the switching timing is obtained from the optimal condition. In this research, the objective is the minimization of the altitude decrease during the deployment. Therefore, since the final value of $\bar{a}$ is fixed to 1, the initial semi-major axis should be minimized. Thus, the following equation must hold:

$$\frac{\partial \sqrt{\bar{a}_1(0)}}{\partial \gamma} = 0. \tag{3.30}$$

Considering that $\alpha_1 = \alpha_2 = 1$ for Sat. 1, using Eqs. (3.20) and (3.30), γ for the altitude decrease minimization case can be obtained as in Eq. (3.31):

$$\gamma = \frac{\beta_{\text{min}}}{\beta_{\text{max}} + \beta_{\text{min}}}. \tag{3.31}$$

From now, α_1, α_2, β_1, and β_2 for Sat. j are denoted as $\alpha_{1,j}$, $\alpha_{2,j}$, $\beta_{1,j}$, and $\beta_{2,j}$, respectively. The required cross-section parameters $\alpha_{1,j}$ and $\alpha_{2,j}$ to achieve the desired constellation are calculated from the obtained τ_f and γ. Here, $\alpha_{1,1} = \alpha_{2,1} = \alpha_{1,N} = \alpha_{2,N} = 1$, $\beta_{1,1} = \beta_{1,N} = \beta_{\text{max}}$, and $\beta_{2,1} = \beta_{2,N} = \beta_{\text{min}}$ hold. From the initial condition of Sat. 1 and j for the semi-major axis and Eq. (3.20) or (3.21), the following relation holds:

$$1 + \frac{\beta_{\text{min}}}{2}\tau_f + \frac{\beta_{\text{max}} - \beta_{\text{min}}}{2}\gamma\tau_f = 1 + \frac{\beta_{2,j}}{2}\tau_f + \frac{\beta_{1,j} - \beta_{2,j}}{2}\gamma\tau_f. \tag{3.32}$$

By substituting Eq. (3.19) into Eq. (3.32), $\alpha_{2,j}$ can be described using $\alpha_{1,j}$ as follows:

$$\alpha_{2,j} = \frac{\gamma}{1-\gamma}\alpha_{1,j} + \frac{1-2\gamma}{1-\gamma}. \tag{3.33}$$

Here, from either Eq. (3.22) or (3.23) at time τ_f (the choice of the equation depends on the desired phase difference $\Delta\theta$), Sat. j's argument of latitude must satisfy the following condition:

$$\theta_j(\tau_f, \alpha_{1,j}) - \theta_1(\tau_f, \alpha_{1,1}) = \Delta\theta_j. \tag{3.34}$$

As mentioned earlier, $\alpha_{1,1} = 1$. If an appropriate $\alpha_{1,j}$ such that Eq. (3.34) holds for a given $\Delta\theta_j$ is obtained, the analytical formulation of the constellation deployment maneuver using the proposed cross-section trajectory model can be achieved. Substituting either Eq. (3.22) or (3.23) into Eq. (3.34), it can be formulated as the sixth-order equation of $\alpha_{1,j}$. Due to space limitations, the details of the sixth-order equation will be omitted. In the same way as the derivation of Eq. (3.29), minor terms can be ignored considering

Eq. (3.26). Therefore, the following quadratic equation of $\alpha_{1,j}$ can be approximated:

$$
\begin{aligned}
&p_a\alpha_{1,j}^2 + q_a\alpha_{1,j} + r_a = 0, \qquad (3.35)\\
&p_a = -\gamma^2\tau_f^3(\beta_{\max} - \beta_{\min})^2,\\
&q_a = \begin{cases} -6\gamma\tau_f^2(\beta_{\max} - \beta_{\min}) & (0 \leqq \Delta\theta_j < \pi) \\ 6\gamma\tau_f^2(\beta_{\max} - \beta_{\min}) & (\pi \leqq \Delta\theta_j < 2\pi) \end{cases},\\
&r_a = \begin{cases} 6\gamma\tau_f^2(\beta_{\max} - \beta_{\min}) - 16\Delta\theta_j & (0 \leqq \Delta\theta_j < \pi) \\ -6\gamma\tau_f^2(\beta_{\max} - \beta_{\min})(4\gamma - 3) - 16\Delta\theta_n & (\pi \leqq \Delta\theta_j < 2\pi) \end{cases}.
\end{aligned}
$$

Considering Eq. (3.26), $1 \gg 4p_ar_a/q_a^2$ holds. Therefore, Eq. (3.35) can be solved as follows:

$$
\alpha_{1,j} = \frac{-q_a + q_a\sqrt{1 - \frac{4p_ar_a}{q_a^2}}}{2p_a} \approx \frac{-q_a + q_a(1 - \frac{2p_ar_a}{q_a^2})}{2p_a} = -\frac{r_a}{q_a}. \qquad (3.36)
$$

From Eqs. (3.29) and (3.36), $\alpha_{1,j}$ can be obtained in a following manner:

$$
\alpha_{1,j} = \begin{cases} -\frac{4(1-\gamma)}{\Delta\theta_N}\Delta\theta_j + 1 & (0 \leqq \Delta\theta_j < \pi) \\ \frac{4(1-\gamma)}{\Delta\theta_N}\Delta\theta_j + 4\gamma - 3 & (\pi \leqq \Delta\theta_j < 2\pi) \end{cases}. \qquad (3.37)
$$

From the above, the analytical maneuver model of the constellation deployment maneuver is formulated. Orbit and cross-section trajectories to achieve the desired constellation are calculated in the following manner:

1. Determine the value of γ using Eq. (3.31).
2. Calculate the deployment time τ_f using Eq. (3.29).
3. Cross-section parameters α_1, and α_2 are calculated using Eqs. (3.33) and (3.37).
4. Trajectories of $\bar{a}$, and θ are obtained from Eqs. (3.20) - (3.23).

3.3.4 Evaluation of Analytical Solution with Numerical Simulation

In Section 3.3, the analytical solution of the deployment time, cross-section trajectories, and the resulting transition of the semi-major axis and the argument of latitude have been

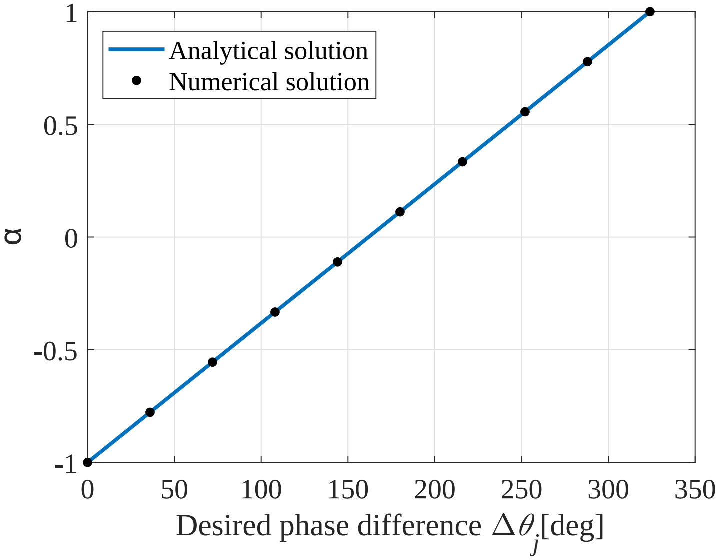

Figure 3.6: Relation between α_1 and $\Delta\theta_j$ ($N = 10$).

formulated. Here, the accuracy of the analytical solution is verified. First, the analytical solution of α_1 shown in Eq. (3.37) is verified. Analytical solutions are compared with numerical solutions of the original sixth-order equation (Eq. (3.34)) for $N = 10$. In the case of $N = 10$, $\Delta\theta_j = 2\pi \times (j-1)/10$ holds. The comparison is shown in Fig. 3.6. From the figure, the analytical solution of α_1 coincides with the numerical solution. Therefore, Fig. 3.6 shows the validity of approximating the sixth-order equation shown in Eq. (3.34) to a quadratic equation shown in Eq. (3.35) when determining $\alpha_{1,j}$.

Next, to verify the validity of obtained analytical solutions of a and θ, they are compared with the results of direct integration of Gauss's planetary equations. Orbit trajectories when cross-section trajectories in Eqs. (3.33) and (3.37) are performed are considered. Then, the mean orbital elements a and θ obtained by integrating Eqs. (2.2) - (2.8) are compared with the analytical solution obtained in Section 3.3. Results are shown in Figs. 3.7 (a) and (b). From these figures, the simulation result and the analytical solution show the same behavior and achieve the desired constellation configuration after time t_f. Therefore, it can be said that the analytical maneuver model proposed in Section 3.3 is sufficiently accurate as a model for the constellation deployment operation.

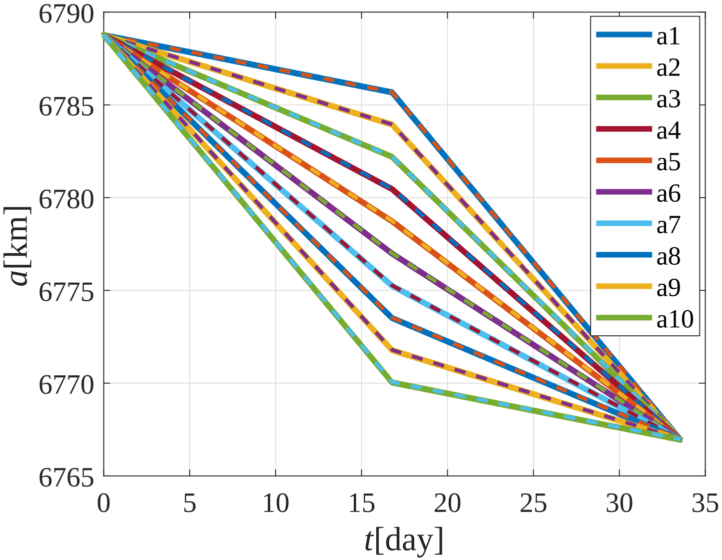

(a) Trajectries of a.

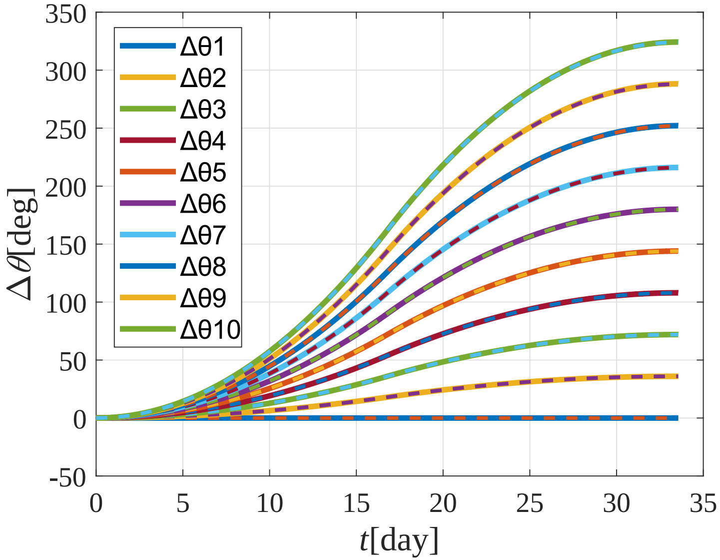

(b) Trajectries of $\Delta\theta_j = \theta_j - \theta_1$.

Figure 3.7: Comparisons of simulation results and analytical solutions.

3.4 Analytical Model Considering the Initial Condition

3.4.1 Overview of the orbit control using maneuver redesign

In Chapter 3.3, assuming that the initial state is immediately after launch, the deployment time τ_f and trajectories of a, θ, and A are analytically formulated. In the analysis, mean J_2 perturbation and constant atmospheric density are assumed. However, in actual operations, the effect of the J_2 perturbation varies dynamically, and atmospheric density changes continuously with altitude. Therefore, satellites are expected to take different orbit transitions from originally planned ones. Thus, it is necessary to compensate for these errors through orbital control. In this research, since constellation deployment using only atmospheric drag is considered, the orbit control is achieved by varying the cross-section. A drag-based orbit control method using the analytical maneuver model is proposed in this section. The cross-section transition is performed following the designed analytical maneuvers. To deal with the current state including errors, the maneuver is redesigned at regular intervals. The control flow is illustrated in Fig. 3.8. To execute the feedback control phase shown in Fig. 3.8, an analytical maneuver redesign considering the current state is needed. The basis of the analytical maneuver design is established in Section 3.3. However, since the state after launch is assumed as the initial condition, the analytical model needs to be extended to consider the arbitrary current state. The deployment time τ_f and target value of a and θ are fixed to the value obtained in Section 3.3. Then, trajectories of A, a, and θ for the given current time and conditions can be formulated. In this section, the cross-section trajectory model from the initial state and the resulting orbit trajectories are mathematically formulated for given τ_f and given target values of a and θ.

3.4.2 Formulation of the cross-section transition

Let τ_{now} denote the current time, and let $\bar{a}_0$ and θ_0 represent the values of $\bar{a}$ and θ at that time. The cross-section trajectory and resulting orbit trajectories from the current state are redesigned and updated. The parameter $\tau' = \tau - \tau_{\text{now}}$ expresses the time from the current moment. A two-phase maneuver, shown in Eq. (3.38) and Fig. 3.9, is performed starting from the current time:

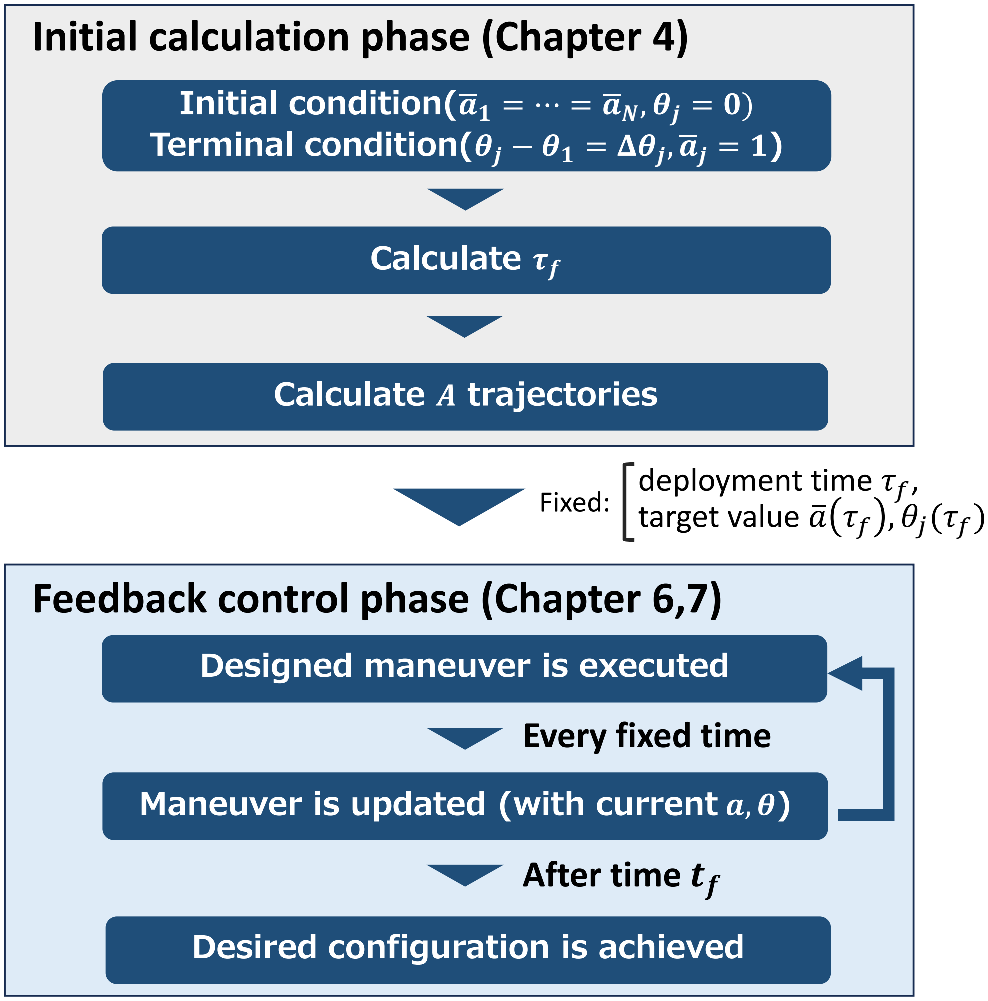

Figure 3.8: Control flow with maneuver redesign.

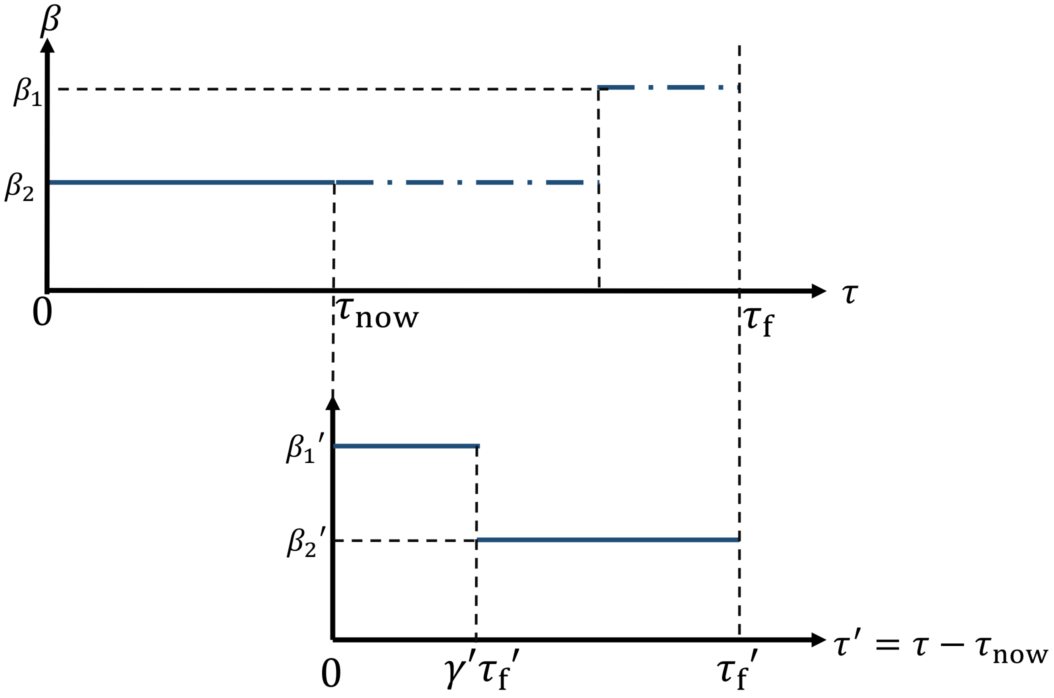

Figure 3.9: Cross-section trajectory model (redesign).

$$\beta = \begin{cases} \beta_1' & (0 \leqq \tau' \leqq \gamma'\tau_f') \\ \beta_2' & (\gamma'\tau_f' < \tau' \leqq \tau_f') \end{cases}, \tag{3.38}$$

$$\beta_1' = \frac{\beta_{\mathrm{max}} + \beta_{\mathrm{min}}}{2} + \alpha_1' \frac{\beta_{\mathrm{max}} - \beta_{\mathrm{min}}}{2}, \quad \beta_2' = \frac{\beta_{\mathrm{max}} + \beta_{\mathrm{min}}}{2} - \alpha_2' \frac{\beta_{\mathrm{max}} - \beta_{\mathrm{min}}}{2}.$$

3.4.3 Analytical formulation of the orbit trajectory considering initial states

The target value for the normalized semi-major axis remains unchanged at $\bar{a} = 1$. The target value for the argument of latitude, which is derived by substituting $\tau = \tau_f$ in Eq. (3.22) or (3.23), also remains unchanged. Assuming the transition of β follows Eq. (3.38), and considering initial values $\bar{a}_0$ and θ_0, Eqs. (3.8) and (3.9) are integrated over the range

$\tau = 0$ to τ'_f. Then, orbit parameters $\bar{a}$ and θ at time τ' are expressed as follows:

$$\sqrt{\bar{a}(\tau')} = \begin{cases} \sqrt{\bar{a}_0} - \frac{\beta'_1}{2}\tau' \quad (0 \leqq \tau' \leqq \gamma'\tau'_f) \\ \sqrt{\bar{a}(\gamma'\tau'_f)} + \frac{\beta'_2}{2}\gamma'\tau'_f - \frac{\beta'_2}{2}\tau' \quad (\gamma'\tau'_f < \tau' \leqq \tau'_f) \end{cases}, \tag{3.39}$$

$$\theta(\tau') = \begin{cases} \frac{1}{\beta'_2}\left(\sqrt{\bar{a}_0} - \frac{\beta'_2}{2}\tau'\right)^{-2} + \\ \frac{\bar{P}}{3\beta'_2}\left(\sqrt{\bar{a}_0} - \frac{\beta'_2}{2}\tau'\right)^{-6} - \frac{\sqrt{\bar{a}_0}^{-2}}{\beta'_2} - \frac{\bar{P}\sqrt{\bar{a}_0}^{-6}}{3\beta'_2} & (0 \leqq \tau' \leqq \gamma'\tau'_f) \\ \frac{1}{\beta'_1}\left\{\left(\bar{S} - \frac{\beta_1}{2}\tau'\right)^{-2} - \left(\bar{S} - \frac{(1-\gamma')\beta'_1}{2}\tau'_f\right)^{-2}\right\} + \\ \frac{\bar{P}}{3\beta'_1}\left\{\left(\bar{S} - \frac{\beta'_1}{2}\tau'\right)^{-6} - \left(\bar{S} + \frac{(1-\gamma')\beta'_1}{2}\tau'_f\right)^{-6}\right\} + \theta\left((1-\gamma')\tau'_f\right) & (\gamma'\tau'_f < \tau' \leqq \tau'_f) \end{cases}, \tag{3.40}$$

where $\bar{S} = \sqrt{\bar{a}((1-\gamma')\tau'_f)} + \beta'_1/2(1-\gamma')\tau'_f$.

3.4.4 Parameter derivation

In this section, the values for α'_1, α'_2, and γ' necessary to achieve the desired constellation configuration are determined. The target value for $\bar{a}$ at time τ'_f is calculated from Eq. (3.39). It should match $\bar{a}(\tau_f)$ derived in Section 3.3. In this research, its value is fixed at 1. Therefore, the following relationship must be satisfied:

$$\sqrt{\bar{a}(\gamma'\tau'_f)} + \frac{\beta'_2}{2}\gamma'\tau'_f - \frac{\beta'_2}{2}\tau' = 1. \tag{3.41}$$

By substituting Eqs. (3.38) and (3.39) into Eq. (3.41), the new cross-section parameter α'_2 can be expressed in terms of α'_1 and γ' in the following manner:

$$\alpha'_2 = \frac{\gamma'}{1-\gamma'}\alpha'_1 + \frac{1}{1-\gamma'}\frac{\beta_{\max} + \beta_{\min}}{\beta_{\max} - \beta_{\min}} - \frac{4(\sqrt{\bar{a}_0} - 1)}{(1-\gamma')(\beta_{\max} - \beta_{\min})\tau'_f}. \tag{3.42}$$

Let θ_{ref} be the argument of latitude that the satellite should take at the final time $\tau = \tau_f$. It is calculated from Eq. (3.22) or (3.23). Here, the value of θ at $\tau' = \tau'_f$ given by

Eq. (3.40), must coincide with θ_{ref}. Hence, the following relation must be satisfied:

$$\theta_{\mathrm{ref}} = \frac{1}{\beta_1'}\left\{\left(\bar{S} - \frac{\beta_1}{2}\tau_f'\right)^{-2} - \left(\bar{S} - \frac{(1-\gamma')\beta_1'}{2}\tau_f'\right)^{-2}\right\} \tag{3.43}$$

$$+\frac{\bar{P}}{3\beta_1'}\left\{\left(\bar{S} - \frac{\beta_1'}{2}\tau_f'\right)^{-6} - \left(\bar{S} + \frac{(1-\gamma')\beta_1'}{2}\tau_f'\right)^{-6}\right\} + \theta\left((1-\gamma')\tau_f'\right).$$

From here, α_1' and α_2' for satellite j are denoted as $\alpha_{1,j}'$ and $\alpha_{2,j}$, respectively. Simplifying Eq. (3.43) results in a sixth-order equation of $\alpha_{1,j}'$. Then, similar to the derivation of $\alpha_{1,j}$ in Section 3.3, major terms can be extracted using Eq. (3.26). From this simplification, Eq. (3.43) can be approximated as a quadratic equation:

$$p_a'\alpha_{1,j}^2 + q_a'\alpha_{1,j} + r_a' = 0, \tag{3.44}$$

where p_a', q_a', and r_a' are expressed in terms of $\beta_{\max}$, $\beta_{\min}$, τ_f', θ_{ref}, θ_0, and $\bar{a}_0$. Due to their complexity, detailed expressions are omitted. In this context, $\alpha_{1,j}'$ is expressed as follows:

$$\alpha_{1,j}' = \frac{-q_a' + \sqrt{q_a'^2 - 4p_a'r_a'}}{2p_a'}. \tag{3.45}$$

Hence, cross-section parameters $\alpha_{1,j}'$ and $\alpha_{2,j}'$ that the satellite should take after the redesign can be expressed using the parameter γ', which determines the switching timing of the satellite cross-section. Therefore, by determining γ', the maneuver that each satellite should take from the current time can be designed. There are two types of constraints: One is that the cross-section value must be within the designated range (Eqs. (3.46) and (3.47)), and the other is that switching must occur correctly during deployment (Eq (3.48)):

$$A_{\min} \leq A_1' \leq A_{\max}, \tag{3.46}$$

$$A_{\min} \leq A_2' \leq A_{\max}, \tag{3.47}$$

$$0 \leq \gamma' \leq 1, \tag{3.48}$$

where A_1' and A_2' are cross-section values calculated from β_1' and β_2', respectively. In the initial calculation phase, since the initial conditions of all satellites are the same, all parameters can be calculated analytically using the other satellites' information. However, in the middle of the deployment, the maneuver redesign without the other satellites' current information is required. In other words, only two final conditions Eqs. (3.41) and (3.43) can be used. Therefore, to deal with the lack of condition expressions and obtain the value of γ', optimization using an interior-point method is used. The objective function f_{int} for the interior-point method is expressed as follows:

$$f_{\text{int}} = k_1(\beta'_1 - \beta_{\text{now}})^2 + k_2(\beta'_2 - \beta_{\text{half}})^2, \tag{3.49}$$

where β_{now} is the current cross-section value before the maneuver redesign and $\beta_{\text{half}} = (\beta_{\text{max}} + \beta_{\text{min}})/2$. The first term of the objective function f_{int} represents the minimization of the attitude change during maneuver updates, contributing to the reduction of power consumption during the attitude maneuver. The second term aims to increase control flexibility during the late stages of deployment by avoiding the cross-section value to approach its lower limit. Without this term, there may be cases where the interior-point method fails to converge during the late stages of deployment. Since all calculations of the objective function and constraint conditions can be performed analytically, the computational cost of this optimization is low. Therefore, it is feasible for on-board calculations.

3.5 Simulation

In this section, the simulation results of the proposed orbit control shown in the previous section are conducted. To increase the control flexibility, $A_{\mathrm{max,init}}$ and $A_{\mathrm{min,init}}$, the maximum and minimum cross-section with margin, are used in the initial calculation phase. In the feedback control phase, actual A_{max} and A_{min} are used as the upper and lower limits for the cross-section. In other words, $|\alpha_1'|$ and $|\alpha_2'|$ can be slightly larger than 1. Table 3.2 outlines the numerical settings for the simulation.

Table 3.2: Simulation conditions.

Maximum cross-section(initial calculation)	$A_{\mathrm{max,init}}$	2.02×10^{-1}	m^2
Minimum cross-section(initial calculation)	$A_{\mathrm{min,init}}$	6.06×10^{-2}	m^2
Maximum cross-section(real)	A_{max}	2.25×10^{-1}	m^2
Minimum cross-section(real)	A_{min}	3.71×10^{-2}	m^2
Objective function gain1	k_1	4×10^{12}	-
Objective function gain2	k_2	1×10^{12}	-
Number of maneuver recalculation	-	15	-

Other satellite and orbital conditions, aside from those mentioned above, are based on Table 3.1.

3.5.1 Case A. With available actual atmospheric density

Real-time altitude information is assumed to be available to the satellite. In each maneuver redesign process, the value of atmospheric density is fixed. However, the atmospheric density value used in the maneuver calculation is updated according to the current altitude. In this case, it is assumed that an accurate value of atmospheric density is available. As the atmospheric density model, the U.S. Standard Atmosphere 1976 [56] is used. The results of the control simulation are illustrated in Figs. 3.10 - 3.12. The vertical dashed line represents the maneuver redesign time. From Figs. 3.10 - 3.12, it is evident that satellites achieved the desired constellation configuration at the terminal time. The error of the final semi-major axis from the target value remains less than 60 m. Additionally, the error of the final in-plane phase difference from the target value remains less than 0.05 deg. Furthermore, during the maneuver redesign in the feedback control phase, only analytical calculations and optimization using an interior-point method are performed.

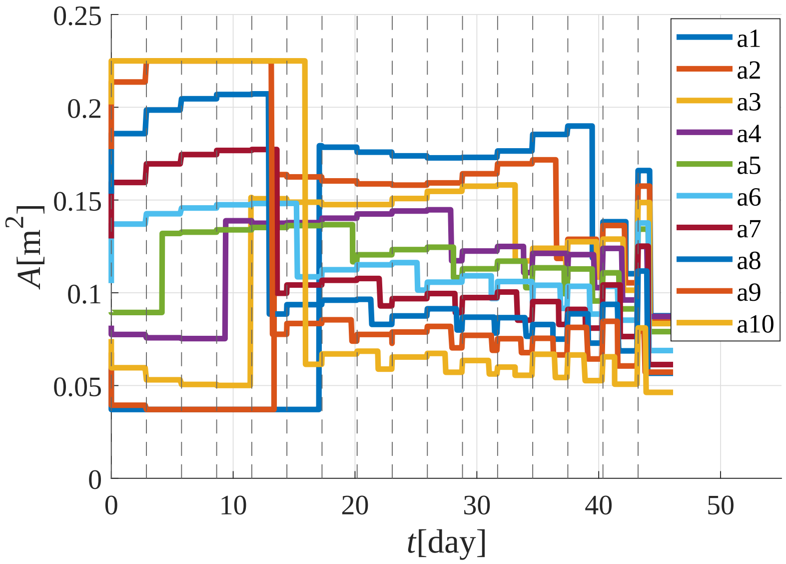

Figure 3.10: Orbit control result (cross-section A, case A).

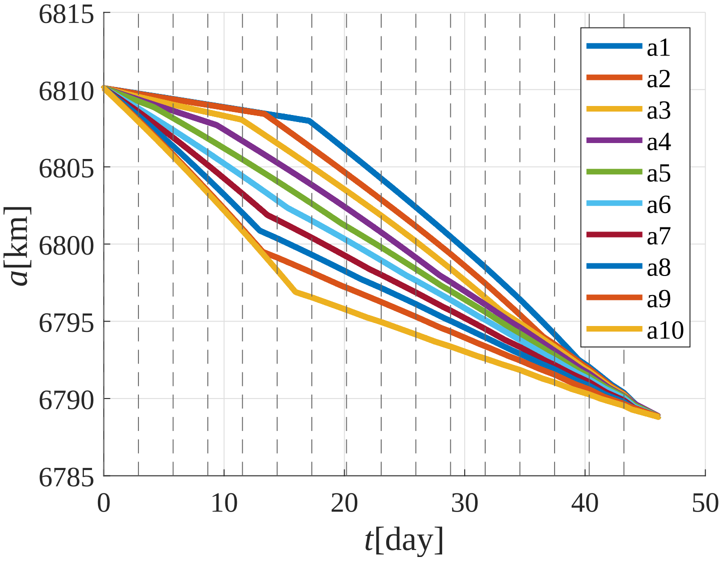

Figure 3.11: Orbit control result (semi-major axis a, case A).

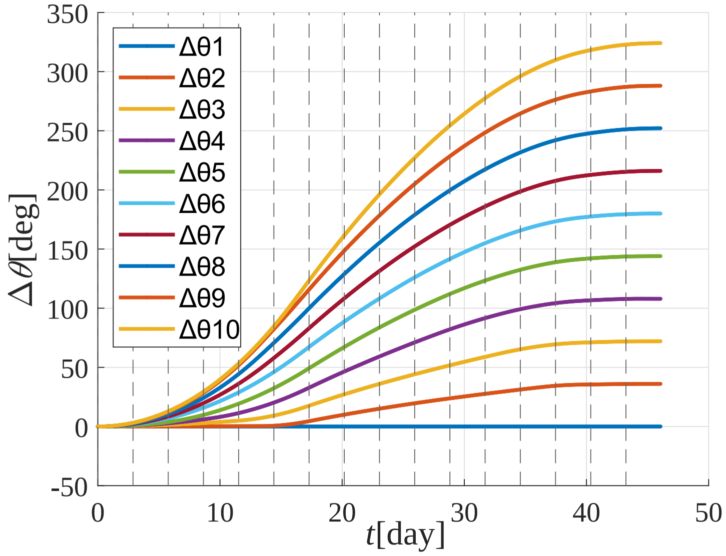

Figure 3.12: Orbit control result (in-plane phase differece $\Delta\theta$, case A).

Since the interior-point method requires low computational cost [57], it is evident that the proposed method can achieve the proper constellation deployment control on small satellites with significant constraints on on-board computer performance.

3.5.2 Case B. With atmospheric density estimation error

In case A, the correct value of the atmospheric density is assumed to be known in the maneuver redesign. However, in actual operations, the atmospheric density takes a different value from the standard atmosphere model. Therefore, the robustness of the proposed control method to the atmospheric density is verified. In the next simulation, as the actual value of the atmospheric density, the atmospheric density model based on Jacchia's model [58] is used, whereas the standard atmospheric model is used in the control calculations. In this case, there is about a 10% error between the actual value and the model of the atmospheric density. The details of these atmospheric density values are shown in Fig. 3.13. Results of the simulation with the atmospheric density error are shown in Figs. 3.14 (a) - (c). From these figures, it can be said that the required constellation configuration is properly achieved. Therefore, the robustness of the proposed control method to the atmospheric density error is verified.

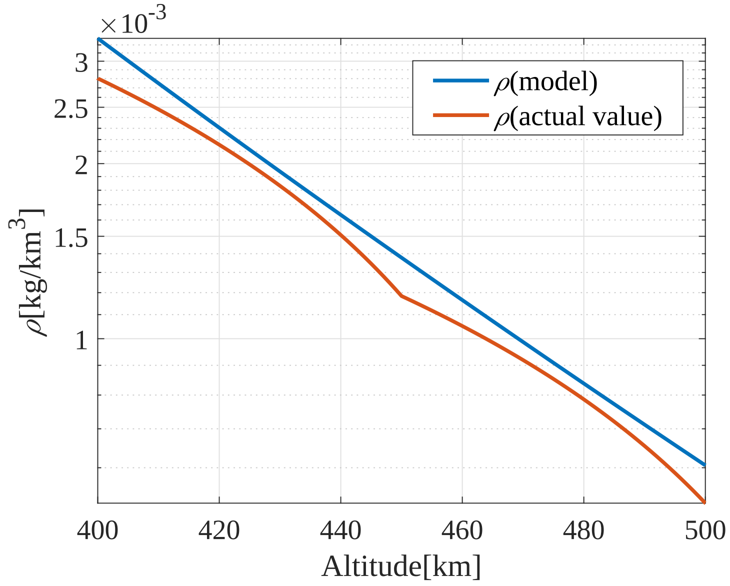

Figure 3.13: The atmospheric density model used in the simulation and control calculation.

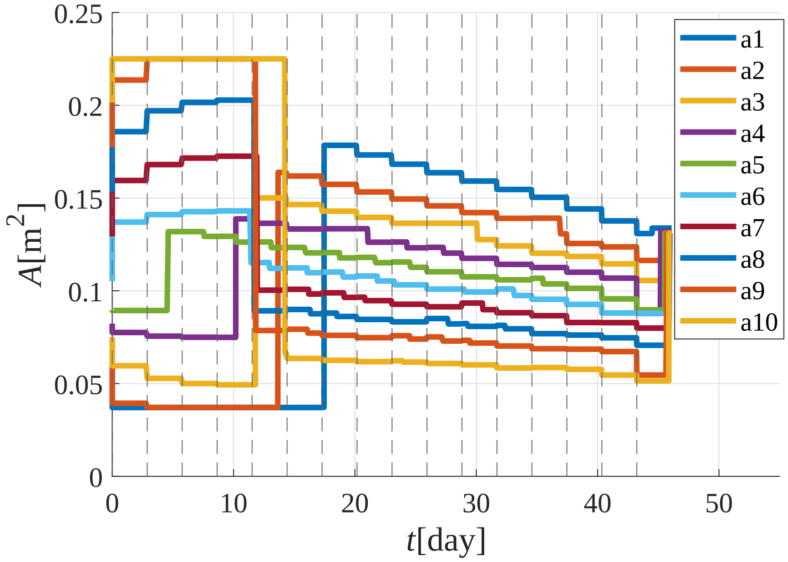

Figure 3.14: Orbit control result (cross-section A, case B).

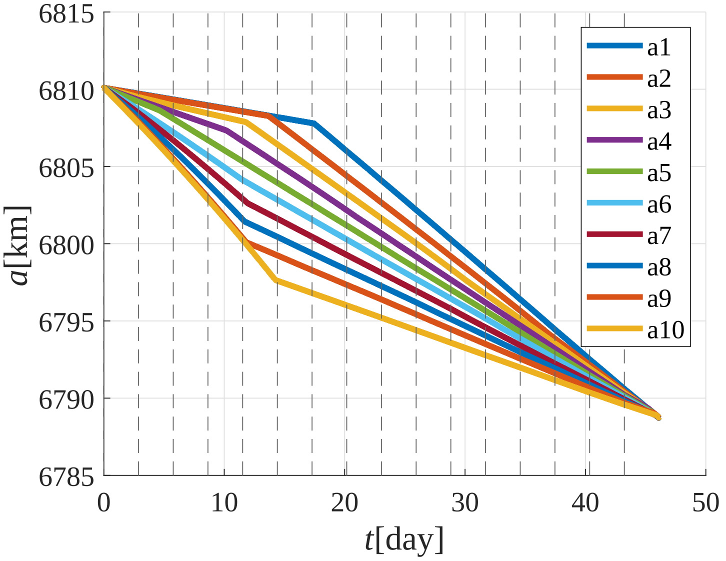

Figure 3.15: Orbit control result (semi-major axis a, case B).

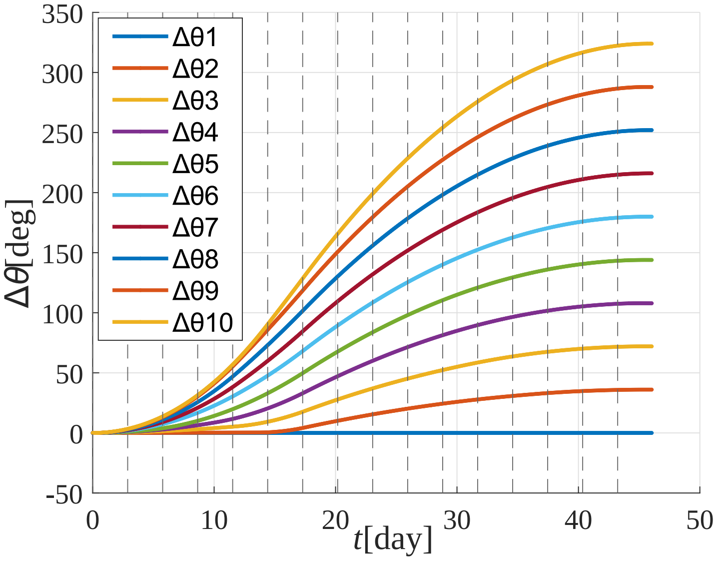

Figure 3.16: Orbit control result (in-plane phase differece $\Delta\theta$, case B).

3.6 Conclusion to Chapter 3

In this chapter, the drag-based in-plane constellation deployment control method without fuel consumption for small satellites, which has strong performance limitations on on-board computers, has been proposed. Initially, considering the effects of atmospheric drag and mean J_2 perturbations, the simplified orbit dynamics model using two parameters, orbit semi-major axis a and the argument of latitude θ, has been proposed. Then, optimal cross-section trajectories and the resulting trajectories of a and θ to minimize the altitude decrease during the deployment have been determined using DCNLP. Next, trajectories of a and θ during the deployment maneuver based on the proposed simplified dynamics and optimization results have been analytically formulated. From them, normalized deployment time τ_f and the required cross-section trajectory to achieve the desired constellation have been obtained. Additionally, considering operational scenarios, orbital transitions for the case with initial values for a and θ have been formulated. Using these formulations, the desired cross-section trajectory to reach the target constellation configuration from the current state has been analytically derived. By utilizing obtained analytical models, the orbit control law that redesigns and updates orbit and cross-section maneuvers based on the current state at regular intervals has been proposed. The effectiveness of the proposed orbit control method has been demonstrated through the numerical simulation. The robustness of the proposed control method in terms of the atmospheric density estimation error has also been verified.

Chapter 4

Optimal mission scheduling

4.1 Formulation of the optimization problem

In this chapter, an optimal Earth observation mission scheduling method for a single satellite with CMGs is developed. To image more targets from a given list of candidates with higher accuracy, we solve an optimization problem to determine the imaging target and timing for each path. First, constraint conditions and an objective function are designed considering the observation requirements, and an optimal mission scheduling problem is formulated as the mixed-integer programming problem. In the computation of the constraint conditions, a practical maneuver time calculation method considering the motion of the actuator is required. Therefore, a fast approximation method of the CMG's gimbal angle trajectory and the attitude maneuver time is developed. The usefulness of the proposed mission scheduling method is verified based on the trend of the obtained optimal solutions. Then, from the computation of rigorous attitude maneuvers and numerical simulations, we show that the proposed fast calculation method for CMG maneuvers has both high computational accuracy and low computational load.

4.1.1 Problem settings

Observation target cities are selected from the candidate list, and the imaging is performed on a north-to-south flight path. Observations are performed in order from north to south, and a stripmap method[59] is adopted in the observation process; the satellite's attitude is fixed during the imaging period. Under these conditions, optimal scheduling aims to find the appropriate city selection and imaging time to image more cities with higher accuracy. Target cities are numbered from north to south and can be selected by designating integer parameters in the optimization algorithm. Therefore, the optimal mission scheduling problem can be formulated as the mixed-integer programming problem that designs city numbers and their imaging times. The details of the constraint conditions and the objective function are shown below.

4.1.2 Constraint conditions

In this section, constraint conditions for the optimal mission scheduling problem are introduced.

Position constraint

Assume that the Earth is a sphere of radius R_E. Let γ be the angle between the position vector of the target city $\boldsymbol{r}_c$ and satellite position vector $\boldsymbol{r}_s$ at the imaging time (see Fig. 4.1). Let $\gamma_{\max}$ be the maximum value of γ within the range that the target can be imaged. Then, the following relation holds:

$$\gamma \leqq \gamma_{\max}. \tag{4.1}$$

The imaging accuracy of the satellite's onboard instruments is inversely proportional to the distance between the satellite and the target. The distance between the satellite and the target city is $|\boldsymbol{r}_s - \boldsymbol{r}_c|$, and the following relation holds when the circular orbit is assumed:

$$|\boldsymbol{r}_s - \boldsymbol{r}_c| = R_E^2 + (R_E + h_{\mathrm{sat}})^2 - 2R_E(R_E + h_{\mathrm{sat}})\cos\gamma, \tag{4.2}$$

where h_{sat} is the satellite altitude. Since the distance $|\boldsymbol{r}_s - \boldsymbol{r}_c|$ becomes smaller as γ becomes smaller, the value of γ affects the imaging accuracy. Therefore, the following constraint conditions for γ are given:

$$\gamma \leqq \gamma_a, \tag{4.3}$$

where γ_a is a constant that can be set arbitrarily less than $\gamma_{\max}$. The maximum distance between the satellite and the target city is determined by restricting the upper bound of γ. Therefore, the position constraint shown in Eq. (4.3) defines the minimum imaging accuracy that should be guaranteed.

Time constraint

Find the direction that the z-axis of the satellite should take when observing the target city j (latitude $\theta_{\mathrm{el}j}$ and longitude $\theta_{\mathrm{az}j}$) at time t_j. A satellite's position vector in an

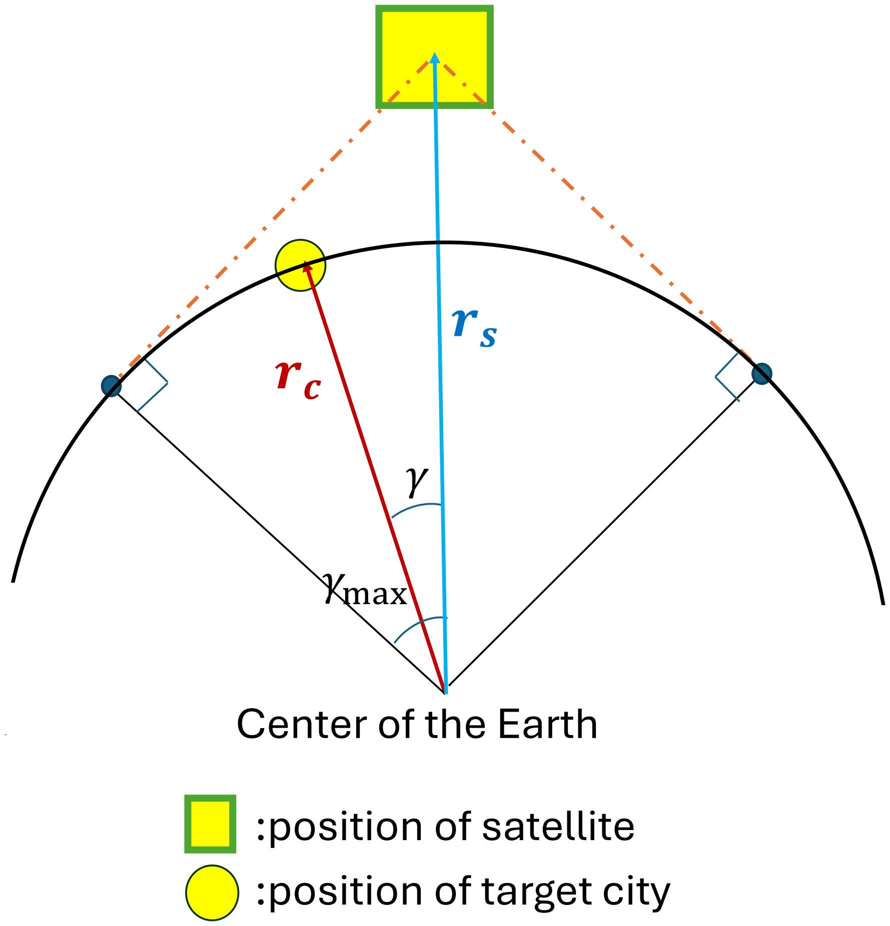

Figure 4.1: Location of satellite and target city.

inertial coordinate $[\boldsymbol{r}_s]_I$ can be calculated from Eq. (2.34). The position of the target city j, $[\boldsymbol{r}_j]_I$, at time t_j can be calculated as follows:

$$[\boldsymbol{r}_j]_I = R_E \begin{bmatrix} \cos(\theta_{\mathrm{az}j} + \lambda_j)\cos\theta_{\mathrm{el}j} \\ \sin(\theta_{\mathrm{az}j} + \lambda_j)\cos\theta_{\mathrm{el}j} \\ \sin\theta_{\mathrm{el}j} \end{bmatrix}, \tag{4.4}$$

where $\lambda_j = \lambda_0 + \omega_e(t_j - t_0)$, λ_0 is obtained from Eq. (2.40), and t_0 is the initial time. Using Eqs. (2.34) and (4.4), The direction the satellite's z-axis required to image the city j at time t_j is expressed as follows:

$$[\hat{\boldsymbol{z}}_j]_I = \frac{[\boldsymbol{r}_j]_I - [\boldsymbol{r}_s]_I}{|[\boldsymbol{r}_j]_I - [\boldsymbol{r}_s]_I|}. \tag{4.5}$$

Denote T_j as the time required for the satellite's z-axis orientation to rotate from $\hat{\boldsymbol{z}}_{j-1}$ to $\hat{\boldsymbol{z}}_j$. A detail of the calculation of T_j is shown in the next section. The satellite is assumed to be pointing its nadir point at the initial time ($j = 0$). Observation period is 2ε, and the satellite's attitude must be fixed for imaging for ε before and after time t_j. Under the above conditions, the following relationship must hold for the satellite to perform imaging correctly.

$$t_j - t_{j-1} \geqq T_j + 2\varepsilon. \tag{4.6}$$

Eq. (4.6) is the maneuver time constraint in the optimization algorithm.

Target selection constraint

This research assumes that the cities are imaged in order of latitude in a single path. All candidate cities are given city numbers in descending order of latitude. The city numbers selected in a path must increase monotonically to image the cities in order of latitude. From above, when N_j is the selected city number for the jth imaging in a path at time t_j, the following relation should hold:

$$N_j - N_{j-1} \geqq 1. \tag{4.7}$$

Eq. (4.7) is the target selection constraint.

4.1.3 Objective function

Let the number of cities observed during the current path n, the angle between the position vector of the target city j $(1 \leq j \leq n)$ and the satellite is γ_j (see Fig. 4.1). The objective function F_{obj} of the mission scheduling optimization is described in the following manner:

$$F_{\text{obj}} = \sum_{j} \gamma_j. \tag{4.8}$$

As mentioned above, a smaller γ leads to improvement in imaging accuracy. Therefore, using the objective function in Eq. (4.8), the improvement of the mean observation accuracy is pursued.

4.1.4 Mission scheduling optimization

The refinement process and calculation order determination

When orbital elements and the initial nadir point of the satellite are given, the position of the satellite and target cities in arbitrary time can be calculated. Therefore, the path order in which the calculations are performed is not necessarily the same as the actual order of the paths in flight. In this research, the trajectories of the satellite and all target cities are calculated using Eqs. (2.2) - (2.7), (2.34), and (4.4) before the optimization process. For all observation paths, find m cities that satisfy the conditions in Eq. (4.1) at least once during a designated flight path, and use them as candidate cities for the optimization calculations. In addition, target cities selected for imaging in previously computed paths are excluded from candidates to prevent overlap of cities to be imaged. These operations to reduce candidate cities in each path are called the "refinement process." The cities removed in the refinement process cannot meet the position constraint during the flight of the path. Therefore, no candidate optimal solution is lost in the refinement process. After the refinement process, the optimization starts from the path with the smallest number of candidate cities m. This prevents paths with more imageable cities from depriving paths with fewer candidate cities of their options. Then, more candidate cities can be imaged in total.

Mission scheduling optimization

In addition to improving the observation quality, the number of the target city to be imaged, denoted by n, should be as large as possible. However, the value of n affects the number of design parameters of the optimization problem. Therefore, using n as an objective function or the design parameter is difficult. Instead, we propose an algorithm that maximizes the number of imaging cities by iterative optimization while increasing n. The detail of the algorithm is shown below:

1. Determine the path to be scheduled.

2. Determine n, the number of cities to be imaged.
3. The refinement process lists m candidate cities.
4. n cities to be imaged are randomly selected from m candidates, and each city's imaging time is set.
5. Optimization is used to find the appropriate city selection and imaging time settings. The optimization can be repeated up to 5 times with different initial conditions to find a feasible solution.
6. If a solution satisfying all constraints is obtained, n is increased by 1, and the same optimization is performed.
7. Otherwise, the result for the $n - 1$ cities, the feasible result of the previous roop, is adopted as the optimal solution.
8. Move to the next path.

The flow of the mission scheduling algorithm is shown in Fig. 4.2. Since city numbers (integer variables) and the imaging time (continuous variable) for each city are designed in the optimization, the proposed optimization problem is classified as a mixed integer programming problem. Ant colony optimization is known to be effective for solving mixed integer programming problems [50]. In this research, optimization calculations are performed using MIDACO, an optimization software based on ant colony optimization. The proposed path selection concept and refinement process can be handled in the same way when there are multiple orbits by multiple satellites. Therefore, although optimization results presented in this chapter consider the single satellite mission, the proposed method is applicable to the constellation mission.

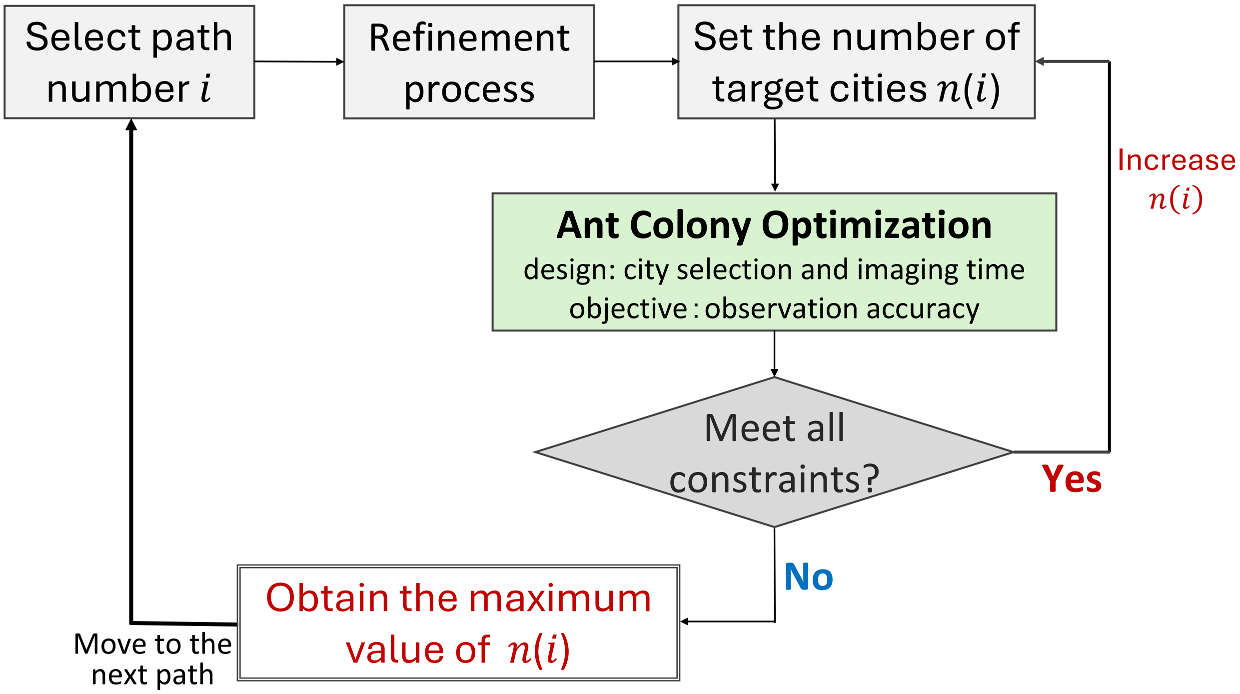

Figure 4.2: Flow of the mission scheduling algorithm.

4.2 Low-cost computation method of the attitude maneuver time using CMGs

4.2.1 Control Momeng Gyros (CMG)

Control Moment Gyro (CMG) is considered the attitude control actuator in this research. CMG is an actuator that generates gyro torque by changing the gimbal angle of the rotating wheel (see Fig. 4.3). Although CMGs require complex control, including consideration of singularities, they have the advantage of high torque output compared to other actuators such as reaction wheels. This research focuses on the system with a pyramid configuration of four CMGs shown in Fig. 4.4. CMG1 is placed in the x-axis direction in $\mathcal{F}_B$, CMG2 is in the y-axis direction, and CMG3 and CMG4 are placed every 90 deg from there. Let θ_k be the gimbal angle of the CMG k $(k = 1, 2, 3, 4)$ and h_w be the wheel angular momentum. The total angular momentum of the CMG system can be formulated as follows:

$$\begin{aligned}[\boldsymbol{h}_c]_B &= h_w \begin{bmatrix} -\sin\theta_1\cos\beta \\ \cos\theta_1 \\ \sin\theta_1\sin\beta \end{bmatrix} + h_w \begin{bmatrix} -\cos\theta_2 \\ -\sin\theta_2\cos\beta \\ \sin\theta_2\sin\beta \end{bmatrix} \\ &+ h_w \begin{bmatrix} \sin\theta_3\cos\beta \\ -\cos\theta_3 \\ \sin\theta_3\sin\beta \end{bmatrix} + h_w \begin{bmatrix} \cos\theta_4 \\ \sin\theta_4\cos\beta \\ \sin\theta_4\sin\beta \end{bmatrix},\end{aligned} \tag{4.9}$$

where β is the skew angle of the CMG system (see Fig. 4.4).

4.2.2 Angular momentum conservation law and attitude representation of satellite

Let $\boldsymbol{J}$ be the moment of inertia, $\boldsymbol{\omega}_s$ be the angular velocity, and $\boldsymbol{h}_s$ be the total angular momentum of the satellite. $\boldsymbol{h}_s$ can be described in the following manner:

$$\boldsymbol{h}_s = \boldsymbol{J}\boldsymbol{\omega}_s + \boldsymbol{h}_c. \tag{4.10}$$

When $\boldsymbol{h}_s$ is assumed to be conserved at $\boldsymbol{0}$, the following relation holds:

$$\boldsymbol{J}\boldsymbol{\omega}_s + \boldsymbol{h}_c = 0. \tag{4.11}$$

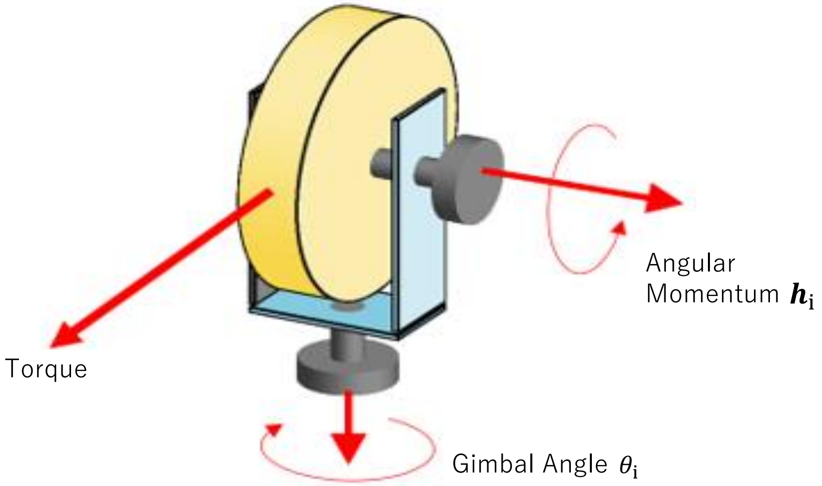

Figure 4.3: Diagram of single CMG.

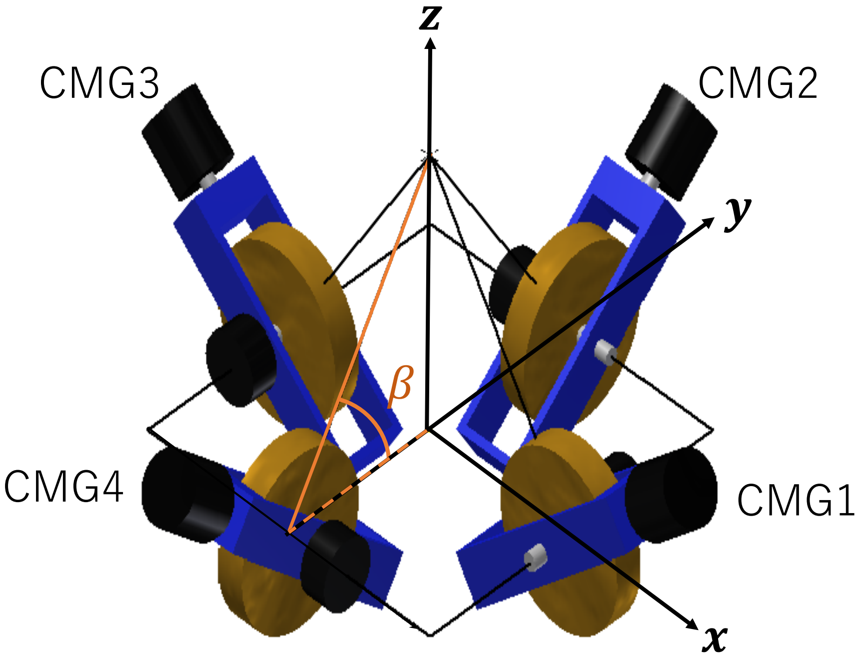

Figure 4.4: Pyramid configuration of four CMGs.

Then, the angular velocity of the satellite can be expressed as shown follows:

$$[\boldsymbol{\omega}_s]_B = -[\boldsymbol{J}]_B^{-1}[\boldsymbol{h}_c]_B. \tag{4.12}$$

The attitude of a satellite is represented by the Euler parameter $\boldsymbol{q}$. Using the rotation axis $[\hat{\boldsymbol{\alpha}}]_B = [\alpha_1, \alpha_2, \alpha_3]^{\mathrm{T}}$ and the rotation angle ϕ, $\boldsymbol{q}$ is described as follows:

$$\boldsymbol{q} = \begin{bmatrix} [\hat{\boldsymbol{\alpha}}]_B \sin\left(\dfrac{\phi}{2}\right) \\ \cos\left(\dfrac{\phi}{2}\right) \end{bmatrix}. \tag{4.13}$$

Eq. (4.14) represents the relation between the Euler parameter and the satellite angular momentum $[\boldsymbol{\omega}_s]_B = [\omega_1, \omega_2, \omega_3]^{\mathrm{T}}$:

$$\begin{aligned} \dot{\boldsymbol{q}} &= \frac{1}{2}\boldsymbol{q} \otimes [\boldsymbol{\omega}]_B \\ &= \frac{1}{2}\begin{bmatrix} 0 & \omega_3 & -\omega_2 & \omega_1 \\ -\omega_3 & 0 & \omega_1 & \omega_2 \\ \omega_2 & -\omega_1 & 0 & \omega_3 \\ -\omega_1 & -\omega_2 & -\omega_3 & 0 \end{bmatrix}\boldsymbol{q}, \end{aligned} \tag{4.14}$$

where $\otimes$ is the quaternion product. In addition, when the first and second attitude changes are expressed in $\boldsymbol{q}_1$ and $\boldsymbol{q}_2$, respectively, the Euper parameter representing the attitude change from the initial attitude to the final attitude is described as follows:

$$\boldsymbol{q}_{12} = \boldsymbol{q}_1 \otimes \boldsymbol{q}_2. \tag{4.15}$$

4.2.3 Maneuver time computation

Overview of the computation method

The calculation method of CMGs' gimbal angle trajectories to execute the desired attitude maneuver is introduced. The following assumptions are imposed for the attitude maneuver:

- Set target gimbal angles $\boldsymbol{\delta}_e$
- Satellite executes uniform angular velocity motion by keeping the gimbal angles to $\boldsymbol{\delta}_e$.

- The gimbal angle changes at the maximum angular acceleration $\ddot{\theta}_{\max}$ until the target gimbal angle is reached.
- The gimbal rate has a maximum value of $\dot{\theta}_{\max}$.
- All gimbal angles become zero at the end of the attitude maneuver.

The example of the gimbal angle trajectory is shown in Fig. 4.5. This figure shows that

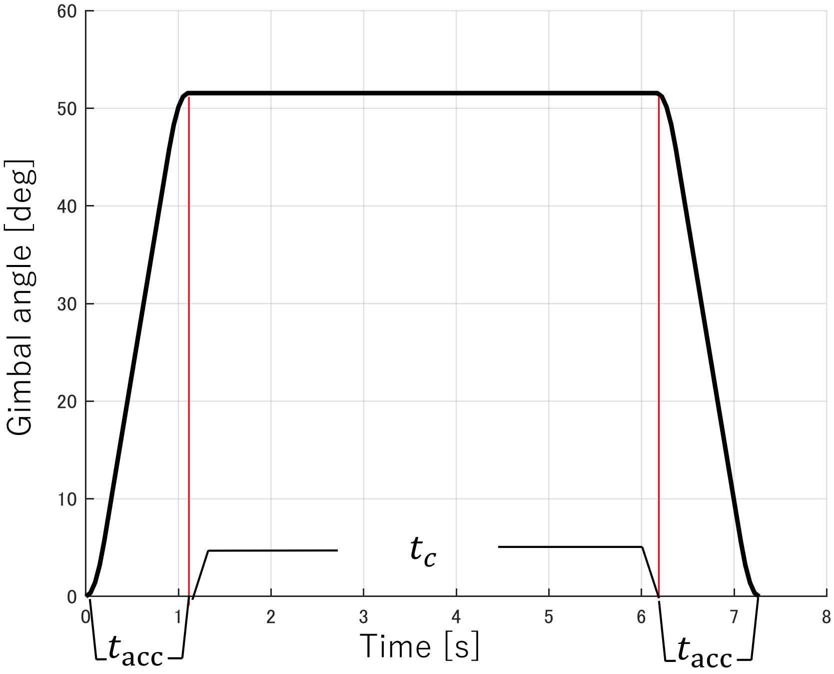

Figure 4.5: Gimbal angle trajectory.

gimbal angles change from 0 to the target value during time t_{acc}. Then, the target gimbal angle is kept for time t_c and returns to zero over time t_{acc}. When the norm of the total angular momentum h_c is given, the following relation is obtained from Eq. (4.11):

$$\boldsymbol{h}_c = h_c \frac{\boldsymbol{J}\hat{\boldsymbol{\alpha}}}{|\boldsymbol{J}\hat{\boldsymbol{\alpha}}|}. \tag{4.16}$$

Here, the target gimbal angles $\boldsymbol{\delta}_e = (\theta_1, \theta_2, \theta_3, \theta_4)$ to output the desired angular momentum $\boldsymbol{h}_c$ should be obtained. When one gimbal angle out of four is given, the remaining three gimbal angles to output the desired angular momentum $\boldsymbol{h}_c$ can be obtained by solving the 8th-order equation [60]. The gimbal angle θ_4 is varied in the range of $[-\pi, \pi]$, and the 8th-order equation is solved each time to obtain $\boldsymbol{\delta}_e$. In this case, multiple $\boldsymbol{\delta}_e$ can be obtained for a certain h_c. The satellite's attitude maneuver time depends on the maximum target gimbal angle of CMGs [42]. Therefore, when multiple $\boldsymbol{\delta}_e$ are given, the solution with the smallest maximum gimbal angle is chosen as the target gimbal angle. Once target gimbal angles $\boldsymbol{\delta}_e$ corresponding to the given h_c are determined, the time t_{acc} to change the gimbal angle and the time t_c to fix the gimbal angle at $\boldsymbol{\delta}_e$ can be obtained.

Derivation of the gimbal acceleration time

Gimbal acceleration time $t_{\mathrm{acc},k}$ to achieve the target gimbal angle θ_k for CMGk ($k =$ 1, 2, 3, 4) is calculated here. Gimbal angle trajectories are determined based on the assumptions made in the previous section. Here, the gimbal rate changes as shown in Fig. 4.6. When the target gimbal angle is small, the triangle acceleration pattern with only uniform gimbal rate and uniform gimbal angular acceleration (see Fig. 4.6(a)) is adopted. Otherwise, the trapezoidal acceleration pattern, which includes the constant gimbal angle area (see Fig. 4.6(b)), is adopted. Since the area of the figure is the Gimbal

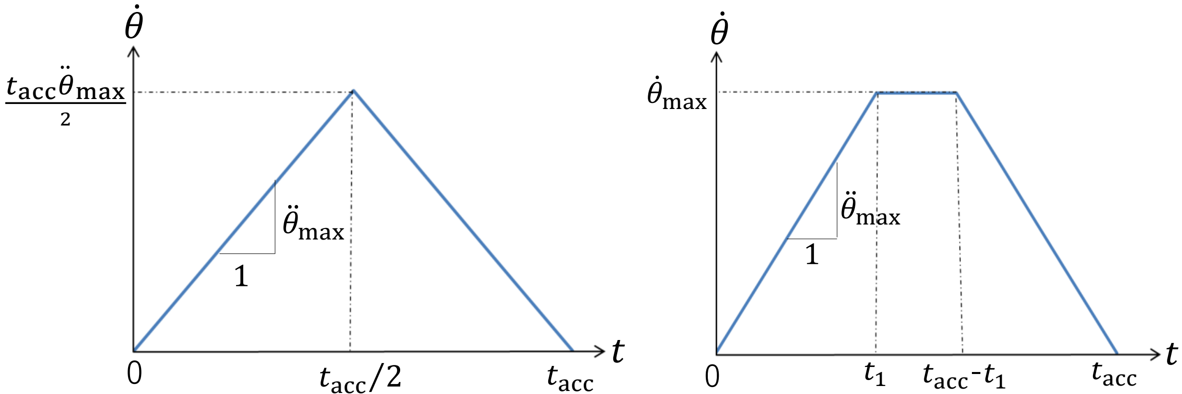

(a)When the target gimbal angle is small

(b)When the target gimbal angle is large

Figure 4.6: Gimbal rate trajectory pattern.

angle, $t_{\mathrm{acc},k}$ can be calculated as follows:

$$t_{\mathrm{acc},k} = \begin{cases} \dfrac{2}{\dot{\theta}_{\max}}\theta_k + \dfrac{2\dot{\theta}_{\max}}{\ddot{\theta}_{\max}} & \left(\frac{\dot{\theta}^2_{\max}}{\ddot{\theta}_{\max}} \leq \theta_k\right) \\ 4\sqrt{\dfrac{\theta_k}{\ddot{\theta}_{\max}}} & \left(\theta_k < \frac{\dot{\theta}^2_{\max}}{\ddot{\theta}_{\max}}\right) \end{cases}, \tag{4.17}$$

$t_{\mathrm{acc},k}$ can be calculated for each of the four CMGs, and the maximum value among them is used as the calculation result t_{acc} in the following section.

Derivation of gimbal holding time

Here, gimbal holding time t_c to fix four gimbal angles at target values is calculated. Using the total attitude maneuver time t_f, the relation between the satellite's rotation angle ϕ along rotation axis $\hat{\boldsymbol{\alpha}}$ and angular velocity $\boldsymbol{\omega}_s$ can be described as follows:

$$\begin{aligned} \phi &= \int_0^{t_f} \boldsymbol{\omega}_s \cdot \hat{\boldsymbol{\alpha}} \mathrm{d}t \\ &= \int_0^{t_{\mathrm{acc}}} \boldsymbol{\omega}_s \cdot \hat{\boldsymbol{\alpha}} \mathrm{d}t + \int_{t_{\mathrm{acc}}}^{t_{\mathrm{acc}}+t_c} \boldsymbol{\omega}_s \cdot \hat{\boldsymbol{\alpha}} \mathrm{d}t + \int_{t_{\mathrm{acc}}+t_c}^{t_{\mathrm{acc}}+t_c+t_{\mathrm{acc}}} \boldsymbol{\omega}_s \cdot \hat{\boldsymbol{\alpha}} \mathrm{d}t \\ &= 2\int_0^{t_{\mathrm{acc}}} \boldsymbol{\omega}_s \cdot \hat{\boldsymbol{\alpha}} \mathrm{d}t + (\boldsymbol{\omega}_{\max} \cdot \hat{\boldsymbol{\alpha}}) t_c, \end{aligned} \tag{4.18}$$

where $\boldsymbol{\omega}_{\max}$ is the angular velocity of the satellite when all CMGs take the maximum gimbal angle. The system angular momentum when CMGs take target gimbal angle $\boldsymbol{\delta}_e$ can be calculated from Eq. (4.9). Therefore, using the angular momentum conservation law shown in Eq. (4.12), $\boldsymbol{\omega}_{\max}$ in body flame can be formulated in the following manner:

$$[\boldsymbol{\omega}_{\max}]_B = -[\boldsymbol{J}]_B^{-1}[\boldsymbol{h}_c(\boldsymbol{\delta}_e)]_B. \tag{4.19}$$

Then, t_c can be calculated as follows:

$$t_c = \frac{\phi - 2\int_0^{t_{\mathrm{acc}}} \boldsymbol{\omega}_s \cdot \hat{\boldsymbol{\alpha}} dt}{\boldsymbol{\omega}_{\max} \cdot \hat{\boldsymbol{\alpha}}}. \tag{4.20}$$

From the obtained t_{acc} and t_c, considering the symmetry of the gimbal angle trajectory, attitude maneuver time can be calculated as follows:

$$t_f = 2t_{\mathrm{acc}} + t_c. \tag{4.21}$$

Derivation of minimum attitude maneuver time

The results above shows that the attitude maneuver time t_f can be calculated when the norm of the CMG system's angular momentum h_c is given. This calculation can be described as a function $t_f = f(h_c)$. How to find the value of h_c to minimize the maneuver time t_f is introduced. In the calculation process shown above, infeasible results can be obtained, for example, $t_c < 0$. If such an improper result is obtained for a given h_c, a sufficiently large t_f is output as a penalty value. Then, the golden section search[61] can be applied to find the proper h_c that minimizes $t_f = f(h_c)$. The obtained $t_{f\min}$ is used as the maneuver time and applied to calculate the time constraint shown in section 4.1.2. The flow of the attitude maneuver time calculation mentioned above is shown in Fig. 4.7.

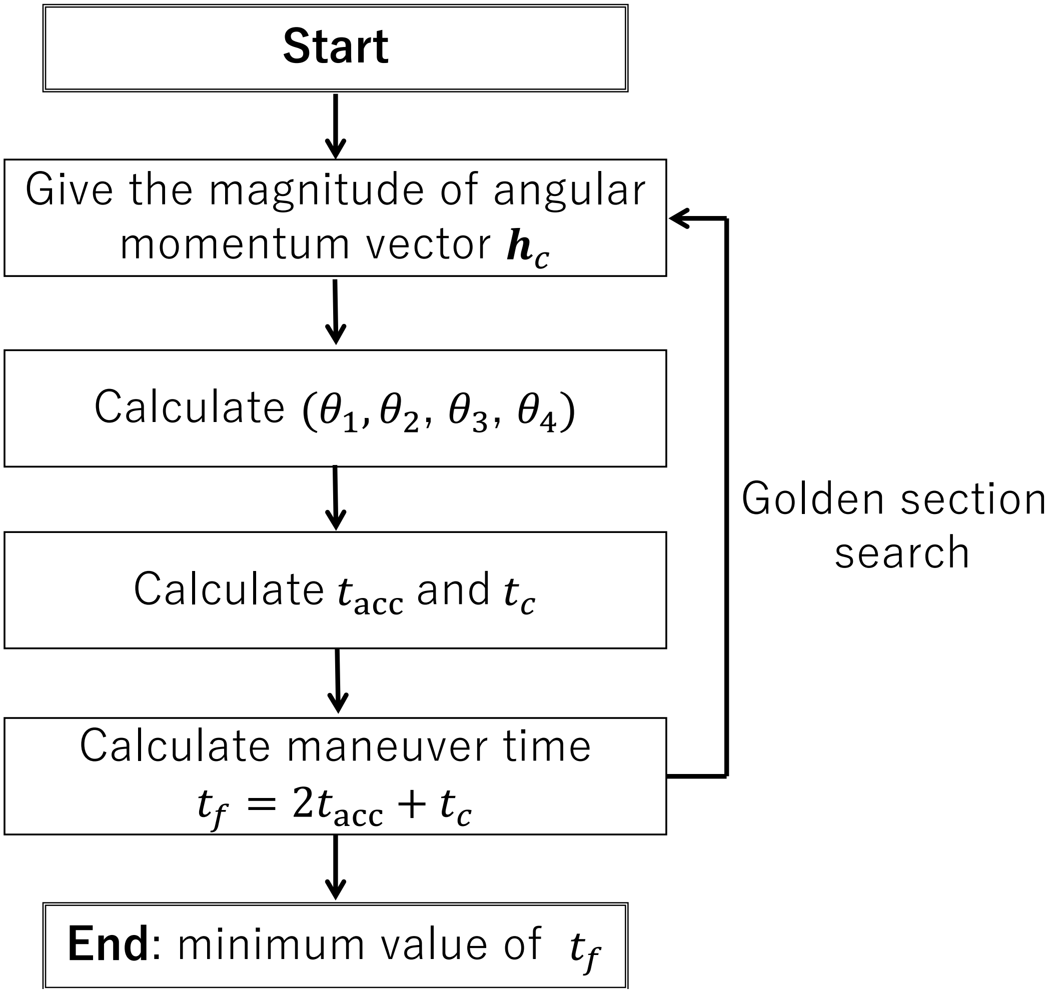

Figure 4.7: Flow of the attitude maneuver time calculation.

4.3 Optimal results of the mission scheduling

4.3.1 Verification of CMG attitude maneuver time

Attitude maneuver time t_f is calculated for various rotation axes $\hat{\boldsymbol{\alpha}}$ and fixed rotation angles ϕ. The calculation result is described with an all-direction maneuver time diagram. The all-direction maneuver time diagram graphically expresses the relation between the rotation axis $\hat{\boldsymbol{\alpha}}$ and the maneuver time t_f for a fixed ϕ. As shown in Fig. 4.8, the vector $\boldsymbol{r}$'s direction from the origin to the figure's surface corresponds to the rotation axis, and the length of $\boldsymbol{r}$ represents the attitude maneuver time t_f. The validity of the proposed method is verified by comparing the attitude maneuver time calculated by the proposed method with one calculated by a rigorous optimization method [42]. The parameters used for the calculation are shown in Table 4.1. Calculation results are shown in Figs. 4.9 - 4.13 and Table 4.2. "Approximate value" means the calculation result of the proposed method and "Optimal value" means the calculation result of the CPS method proposed by Kobayashi et al. [42] The all-direction maneuver time diagram shown in the figure is obtained by a 25×25 rotation axis; the elevation angle (0° - 180°) and azimuth angles (0° - 360°) are each divided into 25 equal parts.

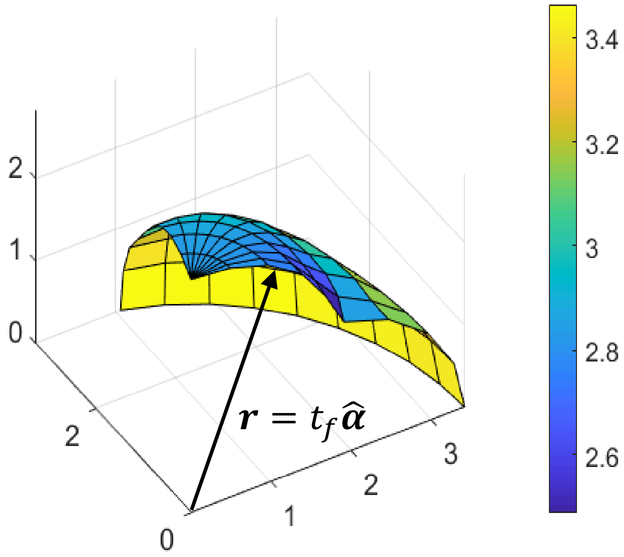

Figure 4.8: All-direction maneuver time diagram.

In a CMG system with a pyramid configuration, setting the skew angle to 54.73° makes it easier to output the same magnitude of angular momentum in all directions[62]. In this research, the optical axes of the instruments are assumed to be aligned with the z-axis. In that case, it is expected that there will be few attitude changes around the z-axis during observation operations, while there will be many attitude changes such as large rotations around the x and y-axis. Therefore, the CMG configuration that can produce large angular momentum in the x and y-axis direction is desirable. From Eq. (4.9), if β is large, the angular momentum in the z direction becomes large, and that in the x, y direction becomes small. For this reason, 45°, smaller than the general value, is adopted as a skew angle in this research.

Table 4.1: Parameters for attitude maneuver time verification.

Symbol	Value	Unit
$\boldsymbol{J}$	$\mathrm{diag}\{40, 30, 30\}$	kgm^2
ϕ	1, 5, 10, 30, 50	deg
h_w	1	Nms
β	45	deg
$\dot{\theta}_{\max}$	1	rad/s
$\ddot{\theta}_{\max}$	5	$\mathrm{rad/s}^2$

Table 4.2: Comparison of approximate and optimal value of attitude maneuver time.

ϕ [deg]	Approximate value [s]	Optimal value [s]	Optimal/Approximate		
			Mean	Maximum	Minimum
1	1.347	1.358	1.009	1.037	0.934
5	2.853	2.850	1.005	1.059	0.927
10	4.074	3.924	1.039	1.168	0.898
30	7.712	7.612	1.013	1.093	0.918
50	11.45	11.46	1.000	1.055	0.911

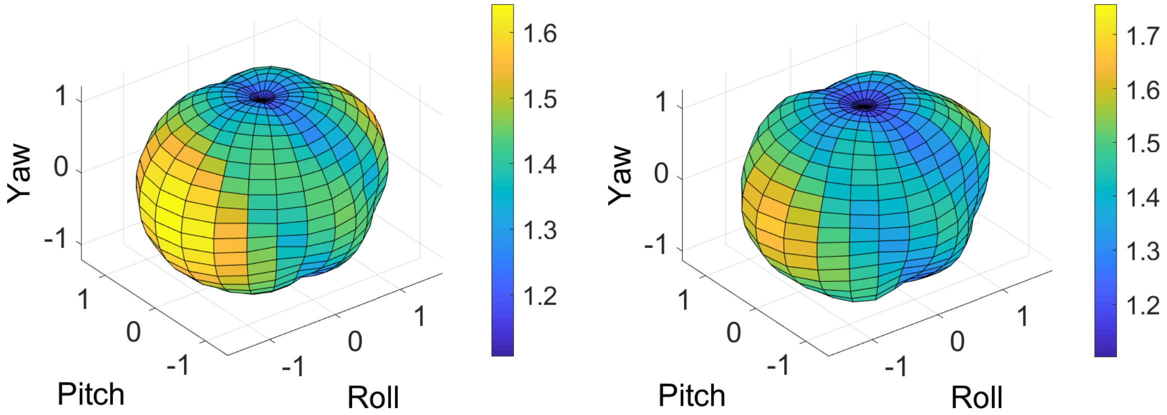

(a)Optimal value (b)Approximate value

Figure 4.9: All direction maneuver time diagram for $\phi = 1$ [deg].

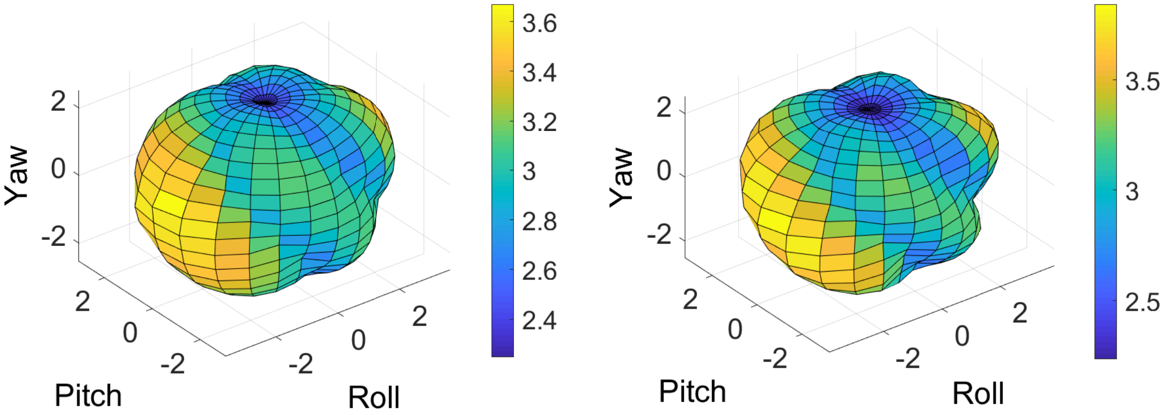

(a)Optimal value (b)Approximate value

Figure 4.10: All direction maneuver time diagram for $\phi = 5$ [deg].

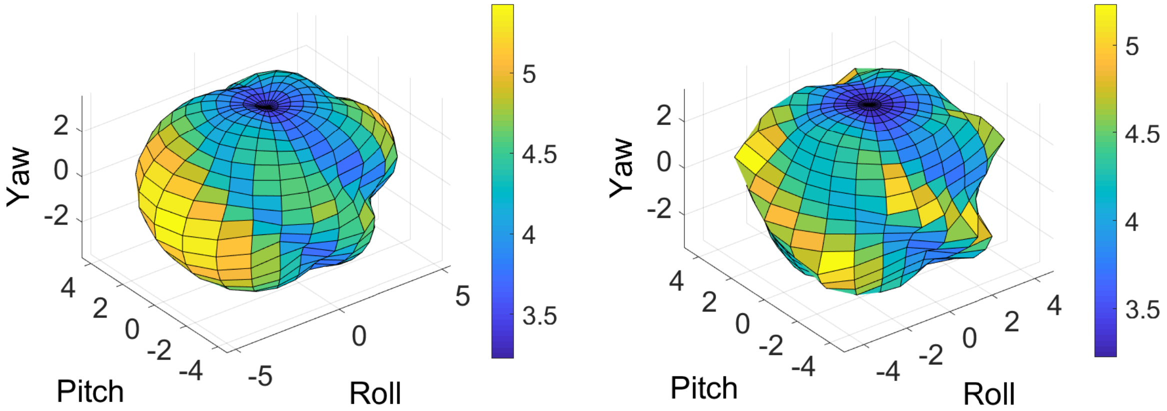

(a)Optimal value (b)Approximate value

Figure 4.11: All direction maneuver time diagram for $\phi = 10$ [deg].

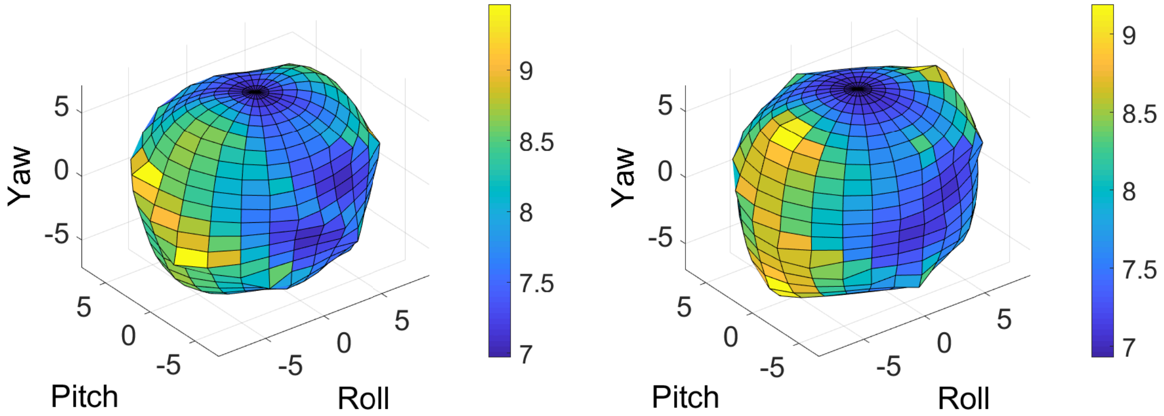

(a)Optimal value (b)Approximate value

Figure 4.12: All direction maneuver time diagram for $\phi = 30$ [deg].

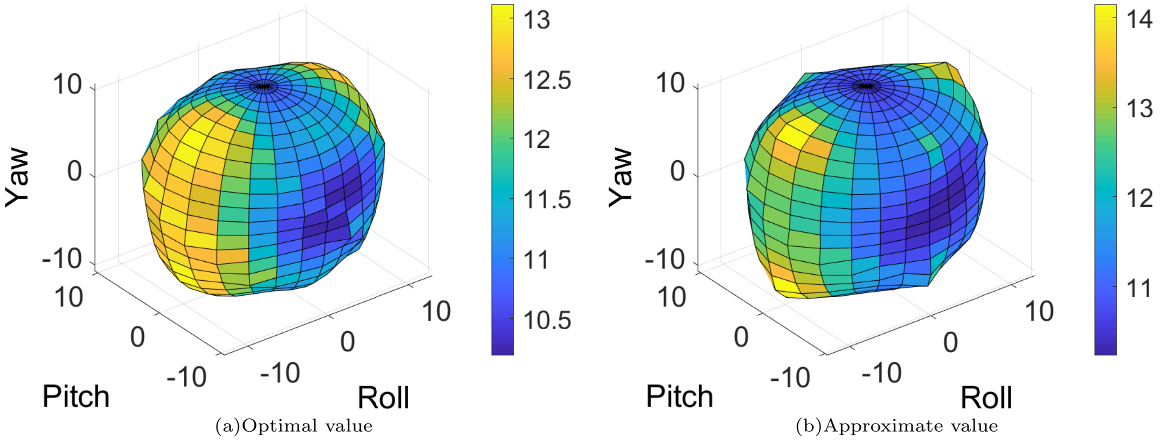

(a)Optimal value (b)Approximate value

Figure 4.13: All direction maneuver time diagram for $\phi = 50$ [deg].

From Figs. 4.9 - 4.13, the surfaces of the all-direction maneuver time diagrams are almost continuously changing. When the rotation axis direction $\hat{\boldsymbol{\alpha}}$ changes slightly, the change in attitude change time is also small. Therefore, we can say that the calculated attitude maneuver time is not sensitive to the rotation axis change. The difference in the shape of the diagram between the optimum value and the approximate value is small. In addition, from Fig. 4.2, the approximated value is within the range of 0.9 to 1.1 times the optimal value. Therefore, the proposed method can calculate a reasonable attitude maneuver time for an arbitrary rotation axis. Next, computation time is considered. For $\phi = 5°$, the calculation time of the optimal calculation [42] is 2.59 seconds on average, and the calculation time of the proposed approximate calculation method is 0.14 seconds on average (CPU: IntelCore i5-4590CPU). For both calculations, MATLAB R2019a is used. The above proposed method can reduce calculation time for attitude maneuver time by a factor of 20. These results confirm that the proposed method can quickly calculate the attitude change time. From Fig. 4.2, the approximate value is not less than the optimal value by adding a margin of 1.1 times to the approximate value. Therefore, if the approximate value multiplied by 1.1 is used to determine the time constraint, the mission schedule can be designed to ensure that the attitude maneuver and imaging can be completed on schedule, even if the approximation error from the actual attitude maneuver time is considered. The next section presents a mission scheduling process using this method, and its effectiveness is confirmed.

4.3.2 Optimization result of the mission scheduling

Target selection and time setting

In this section, we design an imaging plan such that the satellite will observe as many candidate cities as possible in 10 paths flying from north to south. Candidate cities are 292 cities worldwide, and their list is shown in Appendix. Calculations are performed under several conditions with different γ_a in the position constraint shown in Eq. (4.3), and the results are compared. The settings for the maximum satellite-target distance are shown in Table 4.5. Conditions A and E set the maximum distance to 2573 km. This is the maximum distance between a satellite and a city when $\gamma = \gamma_{\max}$ in Eq. (4.2). Conditions B to D are the settings that restrict the distance between the satellite and the target city more strictly to improve the imaging accuracy. Condition E is the same condition as Condition A, but without refinement to confirm its usefulness. Satellite and observation conditions are shown in Table 4.3. The satellite's orbit is a Sun-synchronous circular orbit, and the longitude θ_d of the descending node of the 10 paths is shown in Table 4.4. The results of the calculations for each condition are shown in Figs. 4.14 - 4.18 and Tablea 4.6. Note that the "distance" in the Table 4.6 is the distance between the satellite and the target city when each city is imaged.

Table 4.3: Satellite and observation conditions.

Symbol	Value	Unit
$\boldsymbol{J}$	$\mathrm{diag}\{44.57, 112.61, 81.71\}$	kgm^2
a	6878	km
e	0	-
i	97.4	deg
Ω	0	deg
h_w	1	Nms
β	45	deg
$\dot{\theta}_{\max}$	1	rad/s
$\ddot{\theta}_{\max}$	5	rad/s^2
θ_{lat0}	75	deg
θ_{lon0}	150	deg
The number of paths	10	-
Observation time 2ε	10	s

Table 4.4: Longitude of the descending node θ_d of each path.

Path number	1	2	3	4	5	6	7	8	9	10
θ_d[deg]	115.95	92.27	68.58	44.90	21.22	-2.46	-26.14	-49.82	-73.51	-97.19

Table 4.5: Conditions of γ_a.

Condition	γ_a [deg]	Maximum distance [km]	refinment process
A	21.99	2573	○
B	16.83	2000	○
C	12.27	1500	○
D	7.50	1000	○
E	21.99	2573	-

Table 4.6: Results of the mission scheduling.

Condition	The number of the imageable cities	Distance [km]		
		Mean	Max	Min
A	180	1345	2573	500
B	153	1098	2000	500
C	147	955	1499	500
D	88	671	990	500
E	32	1451	2570	500

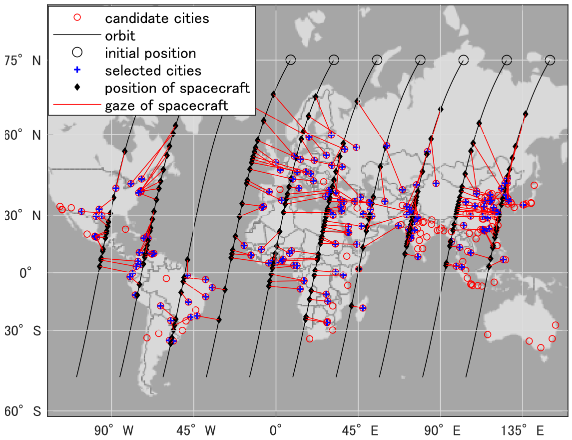

Figure 4.14: Mission scheduling result (Condition A).

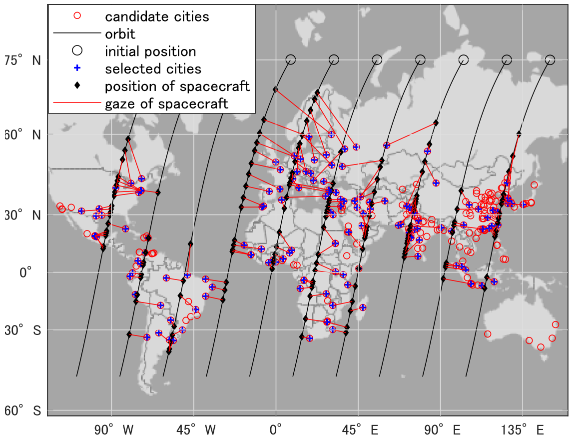

Figure 4.15: Mission scheduling result (Condition B).

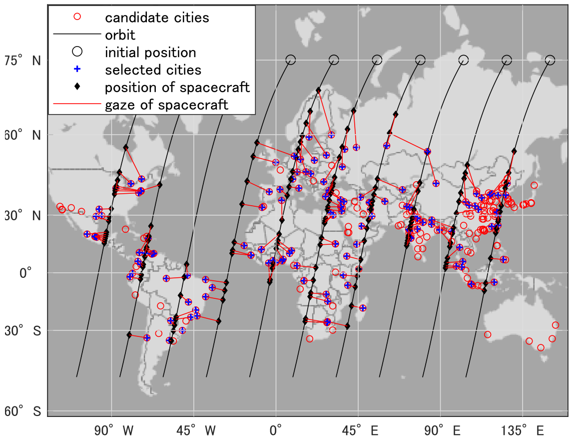

Figure 4.16: Mission scheduling result (Condition C).

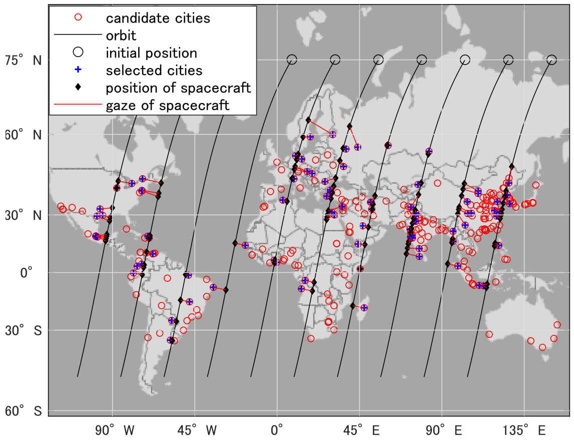

Figure 4.17: Mission scheduling result (Condition D).

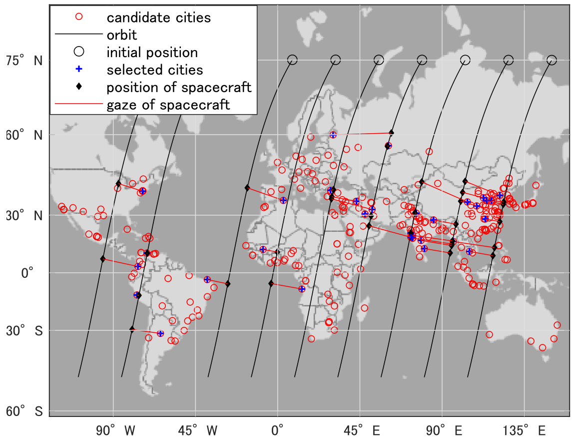

Figure 4.18: Mission scheduling result (Condition E).

Comparison of optimization results

From Fig. 4.6, the total number of imageable cities becomes smaller as the tolerance for position constraints becomes strict. Then, the distance between the satellite and the target cities when the target cities are observed also becomes small. The shorter distance improves the imaging accuracy. Thus, there is a trade-off relation between the number of imageable target cities and the observation accuracy. Since the distance between the city and the satellite increases when imaging with a forward or backward view, imaging with a nadir or sideways view is preferable to improve the imaging quality. Comparison of Figs 4.14 to 4.17 shows that the more rigorous the constraint conditions are, the more sideways views are taken and the fewer forward and backward views are taken. Therefore, it was confirmed that the strict constraint conditions contribute to improving the imaging accuracy. In addition,the comparison of the conditions A and E shows that the number of imageable cities in condition A is more than 5 times larger than those in condition E. When the refinement process is not executed, the number of candidate cities in each path becomes enormous. Accordingly, it becomes difficult to properly select the cities to be imaged in the optimization calculation process. That is why the number of imageable cities for each path in condition E is smaller than in condition A, and some paths did not find any imageable cities or time settings. These results indicate that the proposed method can be used to develop an imaging plan to image more cities while guaranteeing imaging accuracy.

4.3.3 Gimbal angle and attitude trajectory

Gimbal angle trajectories calculated from the proposed approximation method while flying the path with the highest number of imageable cities under condition A are shown in Fig. 4.19. In addition, the trajectories of the gimbal rate during the 5th attitude maneuver of Fig. 4.19 are shown in Fig. 4.20. Considering CMG3 as an example, the gimbal rate increases at a constant acceleration during the initial phase of the gimbal angle transition (498.8 to 499.0 seconds), and the gimbal angle changes linearly after the gimbal rate becomes constant (499.0 to 501.2 seconds). After that, the gimbal rate decreases to 0, and the gimbal angle change stops (501.4 to 501.6 seconds). Then, the gimbal angle is fixed at zero gimbal rate for a certain period (501.6 to 511.8 seconds). Finally, the gimbal angle is decreased by a gimbal rate trajectory symmetrical to the angle increase phase (511.8 to 514.6 seconds), and all gimbal angles become zero. After the attitude maneuver, the CMG is not driven for at least 2ε seconds, which is the imaging time, to maintain the same attitude, and the gimbal angle is driven for the next attitude maneuver.

Next, the practicality of the imaging plan designed by the proposed method in a real mission is shown, using the imaging mission in the path shown in Fig. 4.19 as an example. In the attitude maneuver time estimation method presented in Section 4.3.1, there are two assumptions: a certain upper bound of the gimbal rate and the isometric acceleration of the gimbal. If the assumptions are met during the maneuver, while the gimbal angle of the CMG is changing, the direction of the output angular momentum changes. Then, the direction of the angular velocity of the satellite is not constant. It causes the error between the target attitude and the real attitude after the maneuver. Figure 4.21 shows quaternion trajectories of the satellite when designed CMG gimbal angle trajectories are applied. There remains some attitude error after the maneuver. Therefore, the accurate gimbal angle trajectory to achieve the precise attitude maneuver is determined by modifying the target gimbal angles $\boldsymbol{\delta}_e = [\theta_1, \theta_2, \theta_3, \theta_4]$ using the interior-point method. The modified gimbal angle trajectories are shown in Fig. 4.22. The trajectories of the satellite attitude, when CMGs are driven along the modified gimbal angle trajectories, are shown in the solid line of Fig. 4.21 The dashed line represents the original target attitude obtained from the imaging plan. From Fig. 4.23, for all attitude maneuvers based on the modified gimbal angle trajectory, tracking to the target attitude and imaging can be achieved within the time obtained in the optimal imaging plan. Therefore, the optimal imaging plan obtained using the proposed method with approximation can be used in the actual mission. This result demonstrates the practicality of the proposed method.

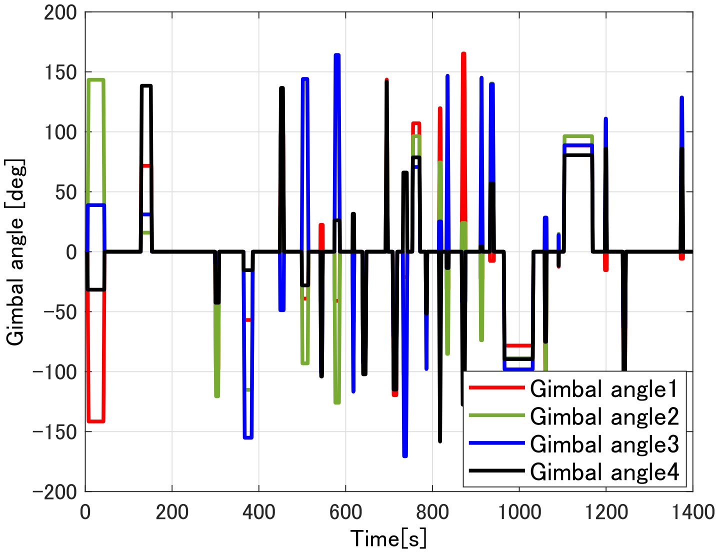

Figure 4.19: Gimbal angle trajectory of the CMGs (original).

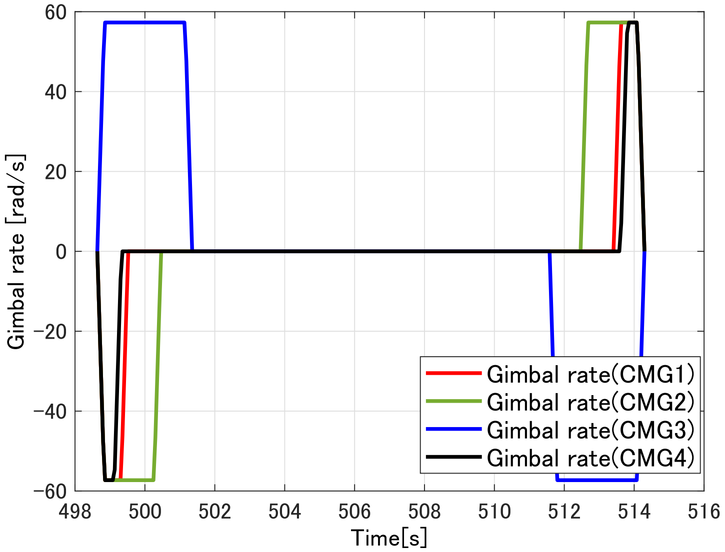

Figure 4.20: Trajectories of the CMG gimbal rate during the attitude maneuver.

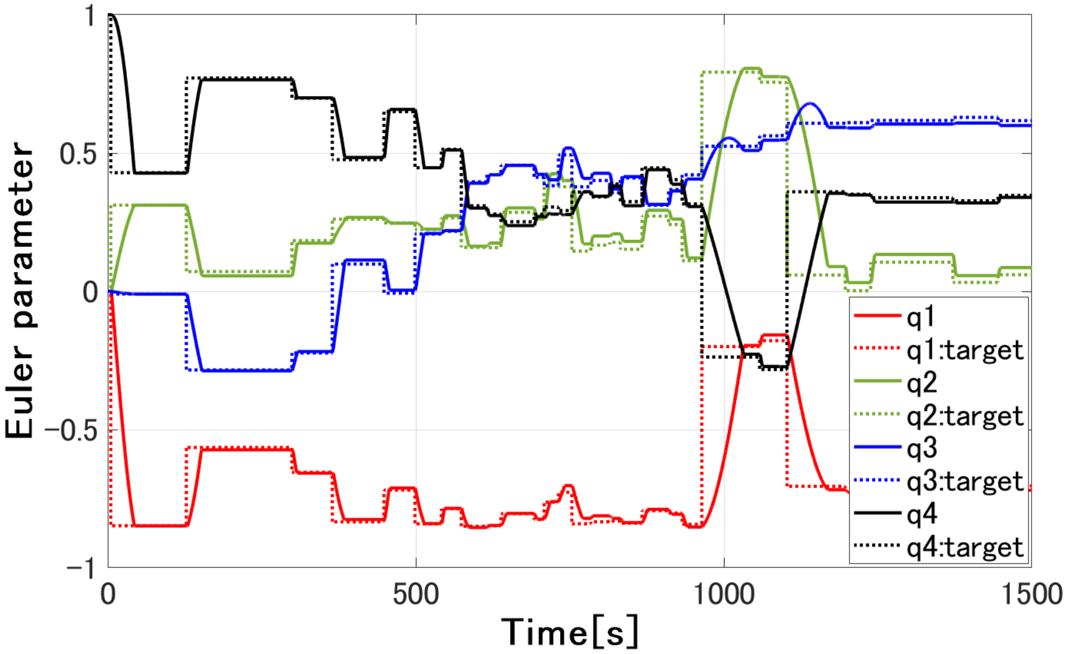

Figure 4.21: Attitude trajectories based on the original gimbal angle trajectory.

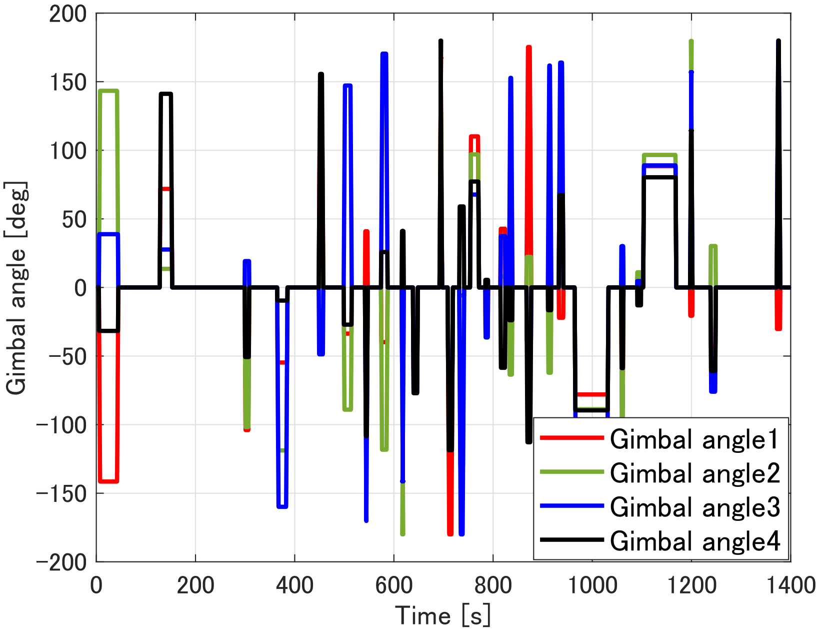

Figure 4.22: Gimbal angle trajectory of the CMGs (modified).

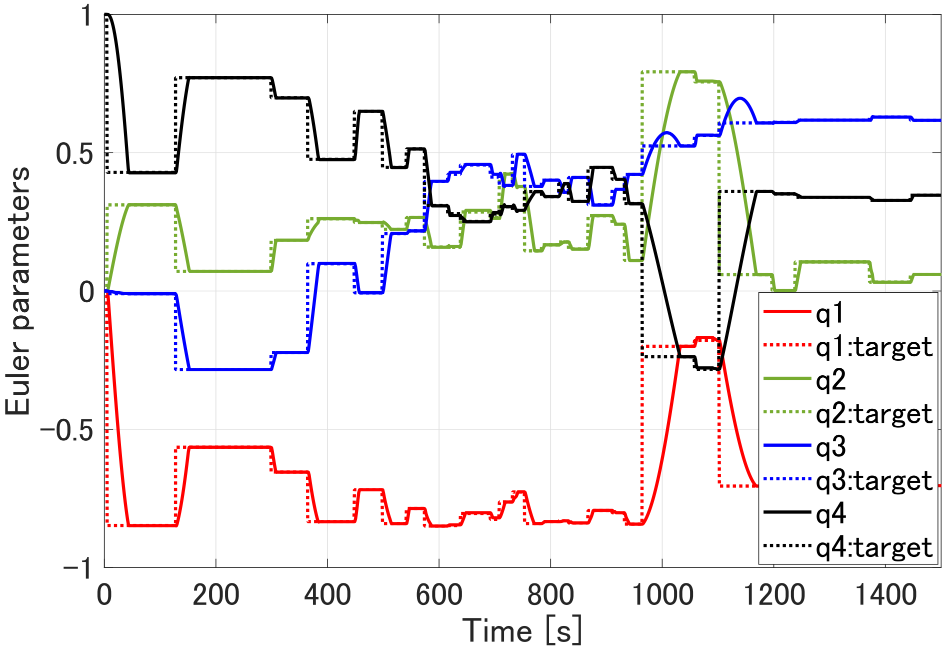

Figure 4.23: Attitude trajectories based on the modified gimbal angle trajectory.

4.4 Conclusion to Chapter 4

Considering the satellite with CMGs, the mission scheduling optimization method to image more candidate cities with higher accuracy has been proposed in this research. The mission scheduling problem has been formulated as a mixed-integer programming problem with an iterative loop structure. The number of the imaged cities and imaging time has been optimized for a given number of the cities to be imaged to shorten the satellite-target distance. By repeating the calculations while increasing the number of cities to be imaged in the path, we have designed a mission plan to observe more target cities more accurately. Position, time, and target selection constraints have been formulated as constraint conditions. In addition, we have developed a target refinement method to narrow down the candidates to make the calculation more efficient and obtain better solutions.

Moreover, to calculate the maneuver time rapidly in the optimization process, a new method to estimate the attitude maneuver time using CMGs at low computational cost has been developed. The proposed method has been compared with the previous maneuver calculation method using nonlinear optimization. The comparison has demonstrated that the proposed method can estimate the attitude maneuver time with a computation time of about 5 percent of the conventional method.

The optimization has been performed for multiple thresholds of the position constraint. Results have proved that there is a trade-off relation between the number of imageable cities and observation qualities. Then, the target gimbal angle has been modified to achieve precise attitude maneuvers without error by using the interior point method based on the estimated trajectories of the CMG gimbal angles. Simulation of the satellite attitude maneuver, when the modified gimbal angle transition was applied, has confirmed that the accuracy of the attitude maneuver was improved. Even in this situation, the attitude maneuver and observation time have been confirmed to be within the time interval designed in the proposed optimal scheduling method. This demonstrates the practicality of the proposed mission scheduling method.

Chapter 5

Conclusion and future work

5.1 Conclusion

This research has focused on the orbit design, initial operation, and actual mission operation of satellite constellations for Earth observation. Specifically, the following three main themes have been considered, and novel results have been obtained from each of them. These results contribute to solving the technical challenges in order to achieve a sustainable Earth management system.

First, an optimal constellation design method for Earth observation satellite constellation has been proposed as a mission scheduling phase before launch. Using the Kepler orbital elements, the orbit requirements to achieve InSAR observation, repeating Sun-synchronous orbit, have been formulated. Then, the constellation design problem has been constructed as a mixed integer programming problem, considering the mission requirements of InSAR observation. Through the meta-heuristic optimization method, optimal constellation configurations have been derived for multiple mission scenarios. The novelty of this research lies in its ability to design optimal solutions that adapt to complex mission-specific conditions, such as non-uniform target placement.

Second, an initial operation phase of the mission has been considered. A constellation deployment control method using atmospheric drag has been proposed to place launched satellites into the designated orbit. In this method, an analytical maneuver model for in-plane deployment has been proposed, and its accuracy has been verified. Furthermore, a new control method based on this model has been proposed. This method does not require complex optimization calculations or information from other satellites. Therefore, it is applicable to small satellites, which are mainly used in satellite constellations.

Finally, actual mission operations have been focused on. A new optimization method for efficient Earth observation scheduling has been proposed. The optimization problem has been formulated as the iterative mixed-integer programming problem to observe more targets more precisely. Also, a low-cost maneuver calculation method for CMG-equipped satellites has been proposed to consider the attitude maneuver time in the optimization process. The validity of the proposed maneuver calculation method has been verified through the numerical simulation. Using this method in the optimization process, highly accurate and reliable mission scheduling has been achieved.

These results provide a theoretical basis for solving technical issues in all phases of satellite constellation missions for Earth observation, from design to operation. This research is an essential step toward realizing sustainable Earth management with constellation systems.

5.2 Future work

This research consists of two aspects: dynamics and actual missions. From the dynamics perspective, the satellite's behavior has been mathematically modeled while considering the effects of the dominant external forces. These insights have been applied to control the satellite's attitude and orbit and to formulate the optimal design problem. From the mission perspective, methods for designing and operating large-scale space systems using nonlinear optimization have been discussed. Both of these perspectives have potential for future development as follows:

From the viewpoint of dynamics, it can be a research theme to elucidate the behavior of satellites under various environments and conditions that are not limited to low Earth orbit. The dynamics of satellites will be explored from various perspectives, including precise prediction of satellite motion by numerical simulation and analytical modeling with approximations to understand the characteristics of satellite behavior. Based on these results, it is also necessary to pursue control laws to control each satellite appropriately. From the viewpoint of actual missions, new research themes can include studying practical mission evaluation criteria that reflect requirements and constraints, formulating optimal mission design problems considering computational cost, and investigating appropriate optimization methods.

As an example of specific future research, this research can be extended to lunar constellations. In the lunar constellation, the influence of the Earth's gravitational potential should be assessed as the third body perturbation [63]. Therefore, when considering an orbit control of a constellation using external forces, as in Chapter 3, new mathematical models of the satellite motion must be formulated reflecting on the effects of the major external force terms. Control methods consistent with the environment and mission conditions should also be constructed using these models. They are future works from the viewpoint of dynamics. On the mission aspect, there is much room for development in mission design and observation scheduling optimization problems. For a lunar constellation, various factors must be considered that are different from those for an Earth observation constellation, such as the cost of orbital transfer from the Earth and more severe equipment constraints. Hence, it is necessary to formulate mission evaluation criteria to evaluate these factors quantitatively. The optimization problem should be constructed with these criteria considering the computational cost, and optimization tools to solve this problem should also be carefully examined. As these examples show, this research can be developed into various research for future space missions.

List of Publications

- 井本悠太, 小畑俊裕, 佐藤訓志, 莊司泰弘, 山田克彦, CMG を搭載した地球観測宇宙機の最適撮像計画, 航空宇宙技術, Vol. 20, 2021, pp. 37-46
- Yuta Imoto, Satoshi Satoh, Toshihiro Obata, and Katsuhiko Yamada, Optimal constellation design based on satellite ground tracks for Earth observation missions, Acta Astronautica, Vol. 207, 2023, pp. 1-9
- Yuta Imoto, Satoshi Satoh, and Katsuhiko Yamada, Orbit trajectory analysis and control of in-plane satellite constellation deployment using atmospheric drag, Acta Astronautica, Vol. xx, 20xx, pp. xx-xx (accepted for publication)

Acknowledgments

First and foremost, I would like to express my sincere appreciation to Professor Satoshi Satoh. As my supervisor, he gave me tremendous advice and passionate support for my research. In addition, after deciding to go on to the Doctoral course, he counseled me many times and taught me what I needed to learn and do in order to live as a researcher. Thanks to his genuine support, I was able to start my research career as a PhD student.

I would also like to extend my special gratitude to Emeritus Professor Katsuhiko Yamada. He was my first supervisor, and he introduced me to the fascination of spacecraft dynamics and the joys of research, even though I had no knowledge of aerospace engineering. Even after his retirement in 2021, he continued to hold regular research meetings and led my research in the right direction with a lot of advice and guidance. Without his guidance and persistent help, this research would not have been possible.

I am deeply grateful to Professor Koichi Osuka and Professor Masato Ishikawa for their careful review, valuable questions, and feedback on improving this research. I would like to express my deepest gratitude to Associate Professor Yasuhiro Shoji at Kanazawa University for his many valuable suggestions in writing Chapter 4. While he was at Osaka University, he also provided various kinds of support so that we students could have a comfortable life in the laboratory. Mr. Toshihiro Obata of synspective, Inc. gave us a lot of advice from both business and technical perspectives in writing chapters 2 and 4. Thanks to his advice, which was based on his experience in satellite development at a company, I could conduct highly practical research suited to actual missions. I would like to give my sincere thanks to him.

I deeply appreciate all students, past and present, of the Satoh Laboratory and the former Yamada Satoh Laboratory.

Finally, I sincerely thank my parents for allowing me to go to the doctoral course and supporting me until today.

Appendix

List of candidate cities

The list of the latitude, longitude, and the name of the target cities used in Chapter 2 and 3 is shown here. Cities with a ”◦” in ”Asia 99 cities” column are those used in the case where 99 Asian cities are observed. However, Yokohama and Hiroshima are included only in case of Asia and not included in case of the entire world.

Table 5.1: Candidate cities.

No.	city	latitude[deg]	longitude[deg]	region	Asia 99 cities
1	Algiers	36.73225	3.08746	Africa	
2	Rabat	34.01325	-6.83255	Africa	
3	Casablanca	33.58831	-7.61138	Africa	
4	Alexandria	31.20176	29.91582	Africa	
5	Cairo	30.06263	31.24967	Africa	
6	Giza	30.00808	31.21093	Africa	
7	Omdurman	15.64453	32.47773	Africa	
8	Khartoum	15.55177	32.53241	Africa	
9	Dakar	14.6937	-17.44406	Africa	
10	Bamako	12.65	-8	Africa	
11	Kano	12.00012	8.51672	Africa	
12	Kaduna	10.52641	7.43879	Africa	
13	Conakry	9.53795	-13.67729	Africa	
14	Camayenne	9.535	-13.68778	Africa	
15	Addis Ababa	9.02497	38.74689	Africa	
16	Ibadan	7.37756	3.90591	Africa	
17	Kumasi	6.68848	-1.62443	Africa	
18	Lagos	6.45407	3.39467	Africa	

Table 5.1: Candidate cities.

No.	city	latitude[deg]	longitude[deg]	region	Asia 99 cities
19	Accra	5.55602	-0.1969	Africa	
20	Abidjan	5.30966	-4.01266	Africa	
21	Douala	4.04827	9.70428	Africa	
22	Yaoundé	3.86667	11.51667	Africa	
23	Mogadishu	2.03711	45.34375	Africa	
24	Kampala	0.31628	32.58219	Africa	
25	Nairobi	-1.28333	36.81667	Africa	
26	Brazzaville	-4.26613	15.28318	Africa	
27	Kinshasa	-4.32758	15.31357	Africa	
28	Dar es Salaam	-6.82349	39.26951	Africa	
29	Luanda	-8.83682	13.23432	Africa	
30	Lubumbashi	-11.66089	27.47938	Africa	
31	Lusaka	-15.40669	28.28713	Africa	
32	Harare	-17.82772	31.05337	Africa	
33	Pretoria	-25.74486	28.18783	Africa	
34	Johannesburg	-26.20227	28.04363	Africa	
35	Soweto	-26.26781	27.85849	Africa	
36	Durban	-29.8579	31.0292	Africa	
37	Cape Town	-33.92584	18.42322	Africa	
38	Montreal	45.50884	-73.58781	America	
39	Toronto	43.70011	-79.4163	America	
40	Chicago	41.85003	-87.65005	America	
41	The Bronx	40.84985	-73.86641	America	
42	Manhattan	40.78343	-73.96625	America	
43	New York City	40.71427	-74.00597	America	
44	Queens	40.68149	-73.83652	America	
45	Brooklyn	40.6501	-73.94958	America	
46	Philadelphia	39.95233	-75.16379	America	
47	Los Angeles	34.05223	-118.24368	America	
48	Phoenix	33.44838	-112.07404	America	
49	Dallas	32.78306	-96.80667	America	
50	San Diego	32.71533	-117.15726	America	
51	Tijuana	32.5027	-117.00371	America	
52	Ciudad Juárez	31.72024	-106.46084	America	
53	Houston	29.76328	-95.36327	America	

Table 5.1: Candidate cities.

No.	city	latitude[deg]	longitude[deg]	region	Asia 99 cities
54	San Antonio	29.42412	-98.49363	America	
55	Havana	23.13302	-82.38304	America	
56	Guadalajara	20.66682	-103.39182	America	
57	Ecatepec	19.60492	-99.06064	America	
58	Santiago de los Caballeros	19.4517	-70.69703	America	
59	Mexico City	19.42847	-99.12766	America	
60	Ciudad Nezahualcoyotl	19.40061	-99.01483	America	
61	Iztapalapa	19.35529	-99.06224	America	
62	Puebla	19.03793	-98.20346	America	
63	Port-au-Prince	18.53917	-72.335	America	
64	Santo Domingo	18.50012	-69.98857	America	
65	House' s Joe Arroyo	10.98597	-74.82172	America	
66	Barranquilla	10.96854	-74.78132	America	
67	Maracaibo	10.66663	-71.61245	America	
68	Caracas	10.48801	-66.87919	America	
69	Maracay	10.23535	-67.59113	America	
70	Valencia	10.16202	-68.00765	America	
71	Medellín	6.25184	-75.56359	America	
72	Bogotá	4.60971	-74.08175	America	
73	Cali	3.43722	-76.5225	America	
74	Quito	-0.22985	-78.52495	America	
75	Belém	-1.45583	-48.50444	America	
76	Guayaquil	-2.20584	-79.90795	America	
77	Manaus	-3.10194	-60.025	America	
78	Fortaleza	-3.71722	-38.54306	America	
79	Recife	-8.05389	-34.88111	America	
80	Lima	-12.04318	-77.02824	America	
81	Salvador	-12.97111	-38.51083	America	
82	Brasilia	-15.77972	-47.92972	America	
83	Santa Cruz de la Sierra	-17.78629	-63.18117	America	
84	Belo Horizonte	-19.92083	-43.93778	America	
85	Rio de Janeiro	-22.90642	-43.18223	America	
86	São Paulo	-23.5475	-46.63611	America	
87	Asunción	-25.30066	-57.63591	America	
88	Curitiba	-25.42778	-49.27306	America	

Table 5.1: Candidate cities.

No.	city	latitude[deg]	longitude[deg]	region	Asia 99 cities
89	Porto Alegre	-30.03306	-51.23	America	
90	Córdoba	-31.4135	-64.18105	America	
91	Santiago	-33.45694	-70.64827	America	
92	Buenos Aires	-34.61315	-58.37723	America	
93	Montevideo	-34.90328	-56.18816	America	
94	Yekaterinburg	56.8519	60.6122	Asia	
95	Novosibirsk	55.0415	82.9346	Asia	
96	Harbin	45.75	126.65	Asia	
97	Changchun	43.88	125.32278	Asia	
98	Jilin	43.85083	126.56028	Asia	○
99	Ürümqi	43.80096	87.60046	Asia	○
100	Almaty	43.25667	76.92861	Asia	
101	Sapporo	43.06667	141.35	Asia	○
102	Fushun	41.88669	123.94363	Asia	○
103	Shenyang	41.79222	123.43278	Asia	○
104	Tashkent	41.26465	69.21627	Asia	
105	Baotou	40.65222	109.82222	Asia	○
106	Beijing	39.9075	116.39723	Asia	
107	Tangshan	39.63333	118.18333	Asia	
108	Ordos	39.6086	109.78157	Asia	○
109	Tianjin	39.14222	117.17667	Asia	○
110	Pyongyang	39.03385	125.75432	Asia	
111	Dalian	38.91222	121.60222	Asia	○
112	Tabriz	38.08	46.2919	Asia	○
113	Shijiazhuang	38.04139	114.47861	Asia	○
114	Taiyuan	37.86944	112.56028	Asia	
115	Seoul	37.566	126.9784	Asia	○
116	Incheon	37.45646	126.70515	Asia	○
117	Suwon	37.29111	127.00889	Asia	○
118	Zibo	36.79056	118.06333	Asia	○
119	Jinan	36.66833	116.99722	Asia	
120	Handan	36.60056	114.46778	Asia	○
121	Mosul	36.335	43.11889	Asia	○
122	Mosul	36.33271	43.10555	Asia	
123	Daejeon	36.32139	127.41972	Asia	

Table 5.1: Candidate cities.

No.	city	latitude[deg]	longitude[deg]	region	Asia 99 cities
124	Mashhad	36.31559	59.56796	Asia	○
125	Aleppo	36.20124	37.16117	Asia	
126	Tai ’ an	36.18528	117.12	Asia	○
127	Qingdao	36.06488	120.38042	Asia	
128	Lanzhou	36.05701	103.83987	Asia	○
129	Saitama	35.90807	139.65657	Asia	○
130	Daegu	35.87028	128.59111	Asia	○
131	Karaj	35.83266	50.99155	Asia	○
132	Tehran	35.69439	51.42151	Asia	
133	Tokyo	35.6895	139.69171	Asia	○
134	Kawasaki	35.52056	139.71722	Asia	○
135	Nagoya	35.18147	136.90641	Asia	○
136	Gwangju	35.15472	126.91556	Asia	○
137	Busan	35.10278	129.04028	Asia	
138	Kyoto	35.02107	135.75385	Asia	○
139	Zhengzhou	34.75778	113.64861	Asia	○
140	Osaka	34.69374	135.50218	Asia	○
141	Kobe	34.6913	135.183	Asia	○
142	Luoyang	34.68361	112.45361	Asia	○
143	Tianshui	34.57952	105.74238	Asia	
144	Kabul	34.52813	69.17233	Asia	○
145	Xi ’ an	34.25833	108.92861	Asia	○
146	Xuchang	34.03189	113.86299	Asia	
147	Peshawar	34.008	71.57849	Asia	
148	Beirut	33.9	35.48333	Asia	
149	Beirut	33.89332	35.50157	Asia	
150	Rawalpindi	33.6007	73.0679	Asia	
151	Fukuoka	33.6	130.41667	Asia	○
152	Damascus	33.5102	36.29128	Asia	
153	Huai ’ an	33.50389	119.14417	Asia	○
154	Baghdad	33.34058	44.40088	Asia	○
155	Isfahan	32.65246	51.67462	Asia	
156	Shiyan	32.6475	110.77806	Asia	○
157	Gujranwala	32.15567	74.18705	Asia	
158	Xinyang	32.12278	114.06556	Asia	

Table 5.1: Candidate cities.

No.	city	latitude[deg]	longitude[deg]	region	Asia 99 cities
159	Nanjing	32.06167	118.77778	Asia	○
160	Amman	31.95522	35.94503	Asia	
161	Hefei	31.86389	117.28083	Asia	○
162	Wuxi	31.56887	120.28857	Asia	○
163	Lahore	31.558	74.35071	Asia	○
164	Faisalabad	31.41554	73.08969	Asia	○
165	Kunshan	31.37762	120.95431	Asia	
166	Suzhou	31.30408	120.59538	Asia	○
167	Shanghai	31.22222	121.45806	Asia	○
168	Ludhiana	30.91204	75.85379	Asia	
169	Nanchong	30.79508	106.08473	Asia	○
170	Chengdu	30.66667	104.06667	Asia	○
171	Wuhan	30.58333	114.26667	Asia	○
172	Basrah	30.50852	47.7804	Asia	○
173	al-Basrah	30.50316	47.81507	Asia	○
174	Hangzhou	30.29365	120.16142	Asia	○
175	Multan	30.19679	71.47824	Asia	
176	Ningbo	29.87819	121.54945	Asia	○
177	Shiraz	29.61031	52.53113	Asia	
178	Chongqing	29.56278	106.55278	Asia	○
179	Puyang	29.45679	119.88872	Asia	○
180	Gorakhpur	29.44768	75.67206	Asia	
181	Yueyang	29.37455	113.09481	Asia	
182	Meerut	28.98002	77.70636	Asia	
183	Nanchang	28.68396	115.85306	Asia	○
184	Delhi	28.65195	77.23149	Asia	○
185	Faridabad	28.41124	77.31316	Asia	
186	Changsha	28.19874	112.97087	Asia	○
187	Guankou	28.15861	113.62709	Asia	
188	Kathmandu	27.70169	85.3206	Asia	
189	Agra	27.18333	78.01667	Asia	
190	Jaipur	26.91962	75.78781	Asia	○
191	Lucknow	26.83928	80.92313	Asia	○
192	Kanpur	26.46523	80.34975	Asia	○
193	Patna	25.59408	85.13563	Asia	

Table 5.1: Candidate cities.

No.	city	latitude[deg]	longitude[deg]	region	Asia 99 cities
194	Hyderabad	25.39242	68.37366	Asia	
195	Taipei	25.04776	121.53185	Asia	○
196	Kunming	25.03889	102.71833	Asia	○
197	Karachi	24.8608	67.0104	Asia	○
198	Riyadh	24.68773	46.72185	Asia	○
199	Xiamen	24.47979	118.08187	Asia	○
200	Medina	24.46861	39.61417	Asia	
201	Dhaka	23.7104	90.40744	Asia	○
202	Shantou	23.36814	116.71479	Asia	○
203	Bhopal	23.25469	77.40289	Asia	
204	Guangzhou	23.11667	113.25	Asia	○
205	Foshan	23.02677	113.13148	Asia	○
206	Ahmedabad	23.02579	72.58727	Asia	○
207	Dongguan	23.01797	113.74866	Asia	○
208	Yunfu	22.92833	112.03954	Asia	○
209	Khulna	22.80979	89.56439	Asia	
210	Indore	22.71792	75.8333	Asia	
211	Kaohsiung	22.61626	120.31333	Asia	
212	Kolkata	22.56263	88.36304	Asia	○
213	Shenzhen	22.54554	114.0683	Asia	○
214	Chittagong	22.3384	91.83168	Asia	○
215	Kowloon	22.31667	114.18333	Asia	○
216	Vadodara	22.29941	73.20812	Asia	
217	Hong Kong	22.27832	114.17469	Asia	○
218	Mandalay	21.97473	96.08359	Asia	
219	Jeddah	21.54238	39.19797	Asia	○
220	Mecca	21.42664	39.82563	Asia	
221	Zhongshan	21.31992	110.5723	Asia	○
222	Surat	21.19594	72.83023	Asia	○
223	Nagpur	21.14631	79.08491	Asia	○
224	Hanoi	21.0245	105.84117	Asia	
225	Nashik	19.99727	73.79096	Asia	
226	Kalyan-Dombivali	19.2437	73.13554	Asia	
227	Nowrangapur	19.23114	82.54826	Asia	
228	Thane	19.19704	72.96355	Asia	

Table 5.1: Candidate cities.

No.	city	latitude[deg]	longitude[deg]	region	Asia 99 cities
229	Mumbai	19.07283	72.88261	Asia	○
230	Navi Mumbai	19.03681	73.01582	Asia	○
231	Pimpri	18.62292	73.80696	Asia	
232	Pune	18.51957	73.85535	Asia	○
233	Dadonghai	18.22056	109.51028	Asia	○
234	Hyderabad	17.38405	78.45636	Asia	○
235	Yangon	16.80528	96.15611	Asia	○
236	Sanaa	15.35472	44.20667	Asia	
237	Caloocan City	14.64953	120.96788	Asia	
238	Quezon City	14.6488	121.0509	Asia	○
239	Manila	14.6042	120.9822	Asia	
240	Bangkok	13.75398	100.50144	Asia	○
241	Chennai	13.08784	80.27847	Asia	○
242	Bengaluru	12.97194	77.59369	Asia	○
243	Phnom Penh	11.56245	104.91601	Asia	
244	Ho Chi Minh City	10.82302	106.62965	Asia	○
245	Tirunelveli	8.72742	77.6838	Asia	
246	Budta	7.20417	124.43972	Asia	
247	Davao	7.07306	125.61278	Asia	
248	Kota Bharu	6.13328	102.2386	Asia	
249	Medan	3.58333	98.66667	Asia	
250	Kuala Lumpur	3.1412	101.68653	Asia	
251	Singapore	1.28967	103.85007	Asia	○
252	Palembang	-2.91673	104.7458	Asia	
253	Makassar	-5.14861	119.43194	Asia	
254	Tangerang	-6.17806	106.63	Asia	
255	Jakarta	-6.21462	106.84513	Asia	○
256	Bekasi	-6.2349	106.9896	Asia	
257	South Tangerang	-6.28862	106.71789	Asia	
258	Bandung	-6.92222	107.60694	Asia	
259	Semarang	-6.99306	110.42083	Asia	
260	Surabaya	-7.24917	112.75083	Asia	○
261	Brisbane	-27.46794	153.02809	Australia	
262	Perth	-31.95224	115.8614	Australia	
263	Sydney	-33.86785	151.20732	Australia	

Table 5.1: Candidate cities.

No.	city	latitude[deg]	longitude[deg]	region	Asia 99 cities
264	Adelaide	-34.92866	138.59863	Australia	
265	Melbourne	-37.814	144.96332	Australia	
266	Saint Petersburg	59.93863	30.31413	Europe	
267	Stockholm	59.33258	18.0649	Europe	
268	Nizhniy Novgorod	56.32867	44.00205	Europe	
269	Moscow	55.75222	37.61556	Europe	
270	Minsk	53.9	27.56667	Europe	
271	Hamburg	53.57532	10.01534	Europe	
272	Berlin	52.52437	13.41053	Europe	
273	Warsaw	52.22977	21.01178	Europe	
274	London	51.50853	-0.12574	Europe	
275	Kyiv	50.45466	30.5238	Europe	
276	Kharkiv	49.98081	36.25272	Europe	
277	Paris	48.85341	2.3488	Europe	
278	Vienna	48.20849	16.37208	Europe	
279	Munich	48.13743	11.57549	Europe	
280	Budapest	47.49801	19.03991	Europe	
281	Milan	45.46427	9.18951	Europe	
282	Belgrade	44.80401	20.46513	Europe	
283	Bucharest	44.43225	26.10626	Europe	
284	Rome	41.89193	12.51133	Europe	
285	Barcelona	41.38879	2.15899	Europe	
286	Istanbul	41.01384	28.94966	Europe	
287	Madrid	40.4165	-3.70256	Europe	
288	Bursa	40.19559	29.06013	Europe	
289	Ankara	39.91987	32.85427	Europe	
290	İzmir	38.41273	27.13838	Europe	
291	Adana	37.00167	35.32889	Europe	
292	Antananarivo	-18.91368	47.53613	Indian	
293	Yokohama	35.43333	139.65	Asia	○(not applicable in World)
294	Hiroshima	34.4	132.45	Asia	○(not applicable in World)

Gimbal angle calculation using inverse kinmeatics

In this section, the calculation method of CMGs' target gimbal angles $\boldsymbol{\delta}_e = (\theta_1, \theta_2, \theta_3, \theta_4)$ to obtain the desired angular momentum $\boldsymbol{h}_c$ is introduced. By setting one gimbal angle among four, the remaining three gimbal angles of $\boldsymbol{\delta}_e$ can be obtained [60]. Here, the gimbal angles θ_1, θ_2, and θ_3 for given θ_4 in the range of $[-\pi, \pi]$ are considered. Using gimbal angles θ_1 - θ_4, parameters h_1, h_2, and h_3 are defined in the following manner:

$$\frac{1}{h_w}\boldsymbol{h}_c = \begin{bmatrix} h_1 \\ h_2 \\ h_3 \end{bmatrix} = \begin{bmatrix} -\sin\theta_1\cos\beta - \cos\theta_2 + \sin\theta_3\cos\beta + \cos\theta_4 \\ \cos\theta_1 - \sin\theta_2\cos\beta - \cos\theta_3 + \sin\theta_4\cos\beta \\ \sin\theta_1\sin\beta + \sin\theta_2\sin\beta + \sin\theta_3\sin\beta + \sin\theta_4\sin\beta \end{bmatrix}. \tag{5.1}$$

Eq. (5.1) can be rewritten as follows:

$$\begin{aligned} \cos\theta_1 - \cos\theta_3 &= h_{20}, && (5.2) \\ \sin\theta_1 + \sin\theta_3 &= \frac{1}{\sin\beta}h_{30}, && (5.3) \\ \sin\theta_1 - \sin\theta_3 &= -\frac{1}{\cos\beta}h_{10}, && (5.4) \end{aligned}$$

where h_{10}, h_{20}, and h_{30} are defined as shown in Eqs. (5.5) - (5.7):

$$\begin{aligned} h_{10} &= h_1 + \cos\theta_2 - \cos\theta_4, && (5.5) \\ h_{20} &= h_2 + \cos\beta(\sin\theta_2 - \sin\theta_4), && (5.6) \\ h_{30} &= h_3 - \sin\beta(\sin\theta_2 + \sin\theta_4). && (5.7) \end{aligned}$$

Here, for arbitrary angles ϕ_1 and ϕ_2, the following relation holds:

$$\begin{aligned} &[(\cos\phi_1 - \cos\phi_2)^2 + (\sin\phi_1 + \sin\phi_2)^2][(\cos\phi_1 - \cos\phi_2)^2 + (\sin\phi_1 - \sin\phi_2)^2] \\ &\qquad = 4(\cos\phi_1 - \cos\phi_2)^2. \end{aligned} \tag{5.8}$$

Substituting θ_1 and θ_3 into ϕ_1 and ϕ_2 in Eq. (5.8) and using Eqs. (5.2) - (5.4), the following relation can be obtained:

$$\left(h_{20}^2 + \frac{h_{30}^2}{\sin^2\beta}\right)\left(h_{20}^2 + \frac{h_{10}^2}{\cos^2\beta}\right) = 4h_{20}^2. \tag{5.9}$$

When θ_4 is fixed, Eq. (5.9) is a quadratic polynominal with respect to $\cos\theta_2$ and quaternary polynomial with respect to $\sin\theta_2$. Then, Eq. (5.9) can be transformed as follows to eliminate the second-order term for $\cos\theta_2$:

$$\left(h_{20}^2 + \frac{h_{30}^2}{\sin^2\beta}\right) \frac{2(h_1 - \cos\theta_4)\cos\theta_2}{\cos^2\beta} = 4h_{20}^2 - \left(h_{20}^2 + \frac{h_{30}^2}{\sin^2\beta}\right) \times \left(h_{20}^2 + \frac{(h_1 - \cos\theta_4)^2 + 1 - \sin^2\theta_2}{\cos^2\beta}\right). \tag{5.10}$$

Eq. (5.10) is the fourth-order polynomial with respect to $\sin\theta_2$ and first-order polynomial with respect to $\cos\theta_2$. Squaring both sides, Eq. (5.10) can be transformed into the eighth-order polynomial with respect to $\sin\theta_2$ as shown in Eq. (5.11):

$$\left(h_{20}^2 + \frac{h_{30}^2}{\sin^2\beta}\right)^2 \frac{4(h_1 - \cos\theta_4)^2(1 - \sin^2\theta_2)}{\cos^4\beta} = \left[4h_{20}^2 - \left(h_{20}^2 + \frac{h_{30}^2}{\sin^2\beta}\right) \times \left(h_{20}^2 + \frac{(h_1 - \cos\theta_4)^2 + 1 - \sin^2\theta_2}{\cos^2\beta}\right)\right]^2. \tag{5.11}$$

Based on Eq. (5.11), gimbal angles θ_1, θ_2, and θ_3 can be obtained in a following manner:

1. Solve the equation Eq. (5.11), and let real solutions whose absolute value is smaller than 1 be candidates of $\sin\theta_2$
2. $\cos\theta_2 = \pm\sqrt{1 - \sin^2\theta_2}$ is calculated for each candidate of $\sin\theta_2$, and candidates of θ_2 are obtained
3. From the candidates of θ_2, choose the θ_2 that satisfies Eq. (5.10).
4. Using the chosen θ_2 and Eqs. (5.3) and (5.4), candidates of $\sin\theta_1$ and $\sin\theta_3$ are obtained as follows:

$$\begin{aligned} \sin\theta_1 &= -\frac{1}{2\cos\beta}h_{10} + \frac{1}{2\sin\beta}h_{30}, && (5.12) \\ \sin\theta_3 &= \frac{1}{2\cos\beta}h_{10} + \frac{1}{2\sin\beta}h_{30}. && (5.13) \end{aligned}$$

5. Among the candidates, find $(\theta_1, \theta_2, \theta_3)$ that satisfies Eq. (5.2) and the absolute value of the right side of Eqs. (5.12) and (5.13) is smaller than 1
6. If multiple solutions of $(\theta_1,\ \theta_2,\ \theta_3,\ \theta_4)$ are obtained, the solution with the smallest maximum value of $(\theta_1,\ \theta_2,\ \theta_3)$ is adopted.

Golden section search

In Section 4.2, the golden section search is used to search the proper value of the angular momentum h_c that minimizes the attitude maneuver time. Golden section search is a numerical calculation method to find the extreme value of a function [61]. In this section, the algorithm of the golden section search is introduced. When $f(x)$ is known to have a minimum in the search area $[a, b]$, the minimum value is found by the following procedure:

1. Let x_1 be the point that separate the area $[a, b]$ into $1 : \phi$, where golden ratio $\phi = (1 + \sqrt{5})/2$.
2. Let x_2 be the point that separate the area $[a, b]$ into $\phi : 1$.
3. When $f(x_1) > f(x_2)$, the area smaller than x_1 is removed and let x_1 be the left end a' of the new search area $[a', b]$. Previous x_2 can be reused as x_1 in the new search area.
4. When $f(x_1) < f(x_2)$, the area larger than x_2 is removed and let x_2 be the right end b' of the new search area $[a, b']$. Previous x_1 can be reused as x_2 in the new search area.
5. The same operation is executed for the new search area $[a', b]$ or $[a, b']$.
6. Repeat the abobe processes until the updated search area $[a, b]$ becomes sufficiently small.
7. For sufficiently small $a - b$, let $y = f((a + b)/2)$ be the minimum value.

The flow of the golden section search is shown in Fig. 5.1. The length of the search area $b - a$ becomes $\phi/(1 + \phi) = 0.618$ times longer in one iteration. Therefore, in ten iterations, the search area becomes $0.618^{10} = 0.00813$ times longer, which is less than 1 % of the initial search area length. In this case, $f(x_1)$ and $f(x_2)$ are compared, and the outer region of the larger one is excluded in order to find the minimum value. On the contrary, in the case of finding the maximum value, the outer region of the smaller one is excluded. A similar method is the ternary search, which divides the search area into 1 : 2 or 2 : 1. A feature of golden section search is that either x_1 or x_2 can be reused in the next step. Therefore, the computational cost of the golden section search is lower than that of the ternary search.

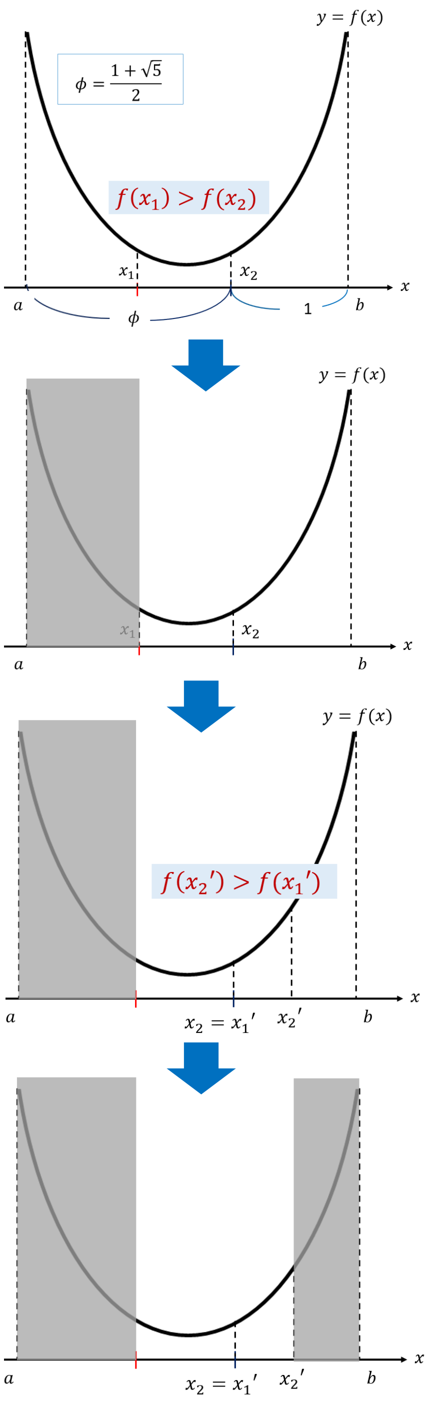

Figure 5.1: Flow of the golden section search.

Bibliography

[1] Marcuccio, S., Ullo, S., Carminati, M., and Kanoun, O.: Smaller Satellites, Larger Constellations: Trends and Design Issues for Earth Observation Systems, *IEEE Aerospace and Electronic Systems Magazine*, **34**, 10(2019), pp. 50–59.

[2] Foster, C., Mason, J., Vittaldev, V., Leung, L., Beukelaers, V., Stepan, L., and Zimmermann, R.: Constellation Phasing with Differential Drag on Planet Labs Satellites, *Journal of Spacecraft and Rockets*, **55**, 2(2018), pp. 473–483.

[3] Fu, X., Wu, M., and Tang, Y.: Design and Maintenance of Low-Earth Repeat-Groundtrack Successive-Coverage Orbits, *Journal of Guidance, Control, and Dynamics*, **35**, 2(2012), pp. 686–691.

[4] Casanova, D., and Mortani, D.: Necklace Theory on Flower Constellations, Proceedings of AAS/AIAA Space Flight Mechanics Meeting Conference, 2011.

[5] Arnas, D., Casanova, D., and Tresaco, E.: 2D Necklace Flower Constellations Applied to Earth Observation Missions, *Acta Astronautica*, **178**(2021), pp. 203–215.

[6] Ortore, E., Cinelli, M., and Circi, C.: A Ground Track-Based Approach to Design Satellite Constellations, *Aerospace Science and Technology*, **69**(2017), pp. 458–464.

[7] Luo, X., Wang, M., Dai, G., and Song, Z.: Constellation Design for Earth Observation Based on the Characteristics of the Satellite Ground Track, *Advances in Space Research*, **59**(2017), pp. 1740–1750.

[8] Ge, H., Li, B., Nie, L., Ge, M., and Schuh, H.: LEO Constellation Optimization for LEO Enhanced Global Navigation Satellite System (LeGNSS), *Advances in Space Research*, **66**(2020), pp. 520–532.

[9] Huang, S., Colombo, C., and Bernelli-Zazzera, F.: Multi-Criteria Design of Continuous Global Coverage Walker and Street-of-Coverage Constellations Through Property Assessment, *Acta Astronautica*, **188**(2021), pp. 151–170.

[10] Zhang, Y., Li, Z., Li, R., wang, Z., Yuan, H., and Song, J.: Orbital design of LEO navigation constellations and assessment of their augmentation to BDS, *Advances in Space Research*, **66**, 8(2020), pp. 1911–1923.

[11] Zhang, T.-J., Shen, H.-X., Li, Z., Qie, H., Cao, J., Li, H.-N., and Yang, Y.-K.: Restricted constellation design for regional navigation augmentation, *Acta Astronautica*, **150**(2018), pp. 231–239.

[12] Li, Y., Zhao, S., and Wu, J.: A General Evaluation Criterion for the Coverage Performance of LEO Constellations, *Aerospace Science and Technology*, **48**(2016), pp. 94–101.

[13] Han, C., Bai, S., Zhag, S., Wang, X., and Wang, X.: Visibility Optimization of Satellite Constellations Using a Hybrid Method, *Acta Astronautica*, **163**(2019), pp. 250–263.

[14] Razoumny, Y. N.: Fundamentals of the route theory for satellite constellation design for Earth discontinuous coverage. Part1: Analytic emulation of the Earth coverage, *Acta Astronautica*, **128**(2016), pp. 722–740.

[15] Razoumny, Y. N.: Fundamentals of the route theory for satellite constellation design for Earth discontinuous coverage. Part2: Synthesis of satellite orbits and constellations, *Acta Astronautica*, **128**(2016), pp. 741–758.

[16] Razoumny, Y. N.: Fundamentals of the route theory for satellite constellation design for Earth discontinuous coverage. Part3: Low-cost Earth observation with minimal satellite swath, *Acta Astronautica*, **129**(2016), pp. 447–458.

[17] Razoumny, Y. N.: Fundamentals of the route theory for satellite constellation design for Earth discontinuous coverage. Part4: Compound satellite structures on orbits with synchronized nodal regression, *Acta Astronautica*, **129**(2016), pp. 459–465.

[18] Razoumny, Y. N.: Route Satellite Constellations for Earth Discontinuous Coverage and Optimal Solution Peculiarities, *Journal of Spacecraft and Rockets*, **54**, 3(2017), pp. 572–581.

[19] Kamali, M. E., Abuelgasim, A., Papoutsis, I., Loupasakis, C., and Kontoes, C.: A reasoned bibliography on SAR interferometry applications and outlook on big interferometric data processing, *Remote Sensing Applications: Society and Environment*, **19**(2020).

[20] Fujiwara, S., Tobita, M., and Murakami, M.: Detecting Crustal Deformation and Generating Digital Elevation Model Using Interferometric Synthetic Aperture Radar, *Journal of the Japan Society of Photogrammetry*, **36**, 3(1997), pp. 71–76 (in Japanese).

[21] Qingjun, Z., Yangte, G., Wenjun, G., Jiaoshan, L., and Ke, L.: 3D Orbit Selection for Regional Observation GEO SAR, *Neurocomputing*, **151**(2015), pp. 692–699.

[22] Liu, S., Meng, T., Jin, Z., and Song, R.: Optimal Deployment of Heterogeneous Microsatellite Constellation Based on Kuhn-Munkres and Simulated Annealing Algorithms, *Journal of Aerospace Engineering*, **35**, 6(2022), p. 04022090.

[23] Pasquale, G. D., Sanjurjo-Rivo, M., and Grande, D. P.: Optimization of constellation deployment using on-board propulsion and Earth nodal regression, *Advances in Space Research*, **70**, 11(2022), pp. 3281–3300.

[24] Crisp, N., Smith, K., and Hollingsworth, P. M.: An integrated design methodology for the deployment of constellations of small satellite, *The Aeronautical Journal*, **123**, 1266(2019), pp. 1193–1215.

[25] Leonard, C. L., Hollister, W. M., and Bergmann, E. V.: Orbital formationkeeping with differential drag, *Journal of Guidance, Control, and Dynamics*, **12**, 1(1989), pp. 108–113.

[26] Kumar, B. S., Ng, A., Yoshihara, K., and Ruiter, A. D.: Differential Drag as a Means of Spacecraft Formation Control, 2007 IEEE Aerospace Conference, 2007, pp. 1–9.

[27] Li, A. S., and Mason, J.: Optimal Utility of Satellite Constellation Separation with Differential Drag, AIAA/AAS Astrodynamics Specialist Conference, 2014.

[28] Sin, E., Arcak, M., and Packard, A.: Small Satellite Constellation Separation using Linear Programming based Differential Drag Commands, 2018 Annual American Control Conference (ACC), 2018, pp. 4951–4956.

[29] Pontani, M., and Teofilatto, P.: Deployment strategies of a satellite constellation for polar ice monitoring, *Acta Astronautica*, **193**(2022), pp. 346–356.

[30] Pontani, M., Pustorino, M., and Teofilatto, P.: Mars Constellation Design and Low-Thrust Deployment Using Nonlinear Orbit Control, *Journal of the Astronautical Sciences*, **69**(2022), pp. 1691–1725.

[31] Shang, H., Wang, S., and Wu, W.: Design and optimization of low-thrust orbital phasing maneuver, *Aerospace Science and Technology*, **42**(2015), pp. 365–375.

[32] Imoto, Y., Satoh, S., and Yamada, K.: In-plane deployment analysis of satellite constellation using atmospheric drag, Proc. 34th Int. Symp. Space Technology and Science, 2023.

[33] Liu, X., Bai, B., Chen, Y., and Yao, F.: Multi satellites scheduling algorithm based on task merging mechanism, *Applied Mathematics and Computation*, **230**(2014), pp. 687–700.

[34] Vasquez, M., and Hao, J.: A Logic-Constrained Knapsack Formulation and a Tabu Algorithm for the Daily Photograph Scheduling of an Earth Observation Satellite, *Computational Optimization and Applications*, **20**(2001), pp. 137–157.

[35] Yao, F., Li, J., Bai, B., and He, R.: Earth Observation Satellites Scheduling Based on Decomposition Optimization Algorithm, *International Journal of Image, Graphics and Signal Processing*, **2**(2010), pp. 1–18.

[36] Spangelo, S., Cutler, J., Gilson, K., and Cohn, A.: Optimization-based scheduling for the single-satellite, multi-ground station communication problem, *Computers & Operations Research*, **57**(2015), pp. 1–16.

[37] Abbas, A., Meselhy, K., Moughith, W., and Omer, A.: Agile mission optimization for a constellation of earth observation satellites, 18th International Conference on Aerospace Sciences & Aviation Technology, 2019.

[38] Wang, S., Zhao, L., Cheng, J., Zhou, J., and Wang, Y.: Task scheduling and attitude planning for agile earth observation satellite with intensive tasks, *Aerospace Science and Technology*, **90**(2019), pp. 23–33.

[39] Kim, H., and Chang, Y. K.: Mission scheduling optimization of SAR satellite constellation for minimizing system response time, *Aerospace Science and Technology*, **20**(2015), pp. 17–32.

[40] Lemaitre, M., Verfaillie, G., Jouhaud, F., Lachiver, J.-M., and Bataille, N.: Selecting and scheduling observations of agile satellites, *Aerospace Science and Technology*, **6**, 5(2002), pp. 367–381.

[41] Cui, K., Ziang, J., and Zhang, Y.: Mission planning optimization of video satellite for ground multi-object staring imaging, *Advances in Space Research*, **61**(2018), pp. 1476–1489.

[42] Kobayashi, H., Shoji, Y., and Yamada, K.: Optimal Attitude Trajectory of Spacecraft with Pyramid-Type CMGs Using a Pseudo-Spectral Method (in Japanese), *Aerospace technology Japan*, **16**(2017), pp. 55–63.

[43] Kawajiri, S., and Matunaga, S.: A low-complexity attitude control method for large-angle agile maneuvers of a spacecraft with control moment gyros, *Acta Astronautica*, **139**(2017), pp. 486–493.

[44] Schaub, H., and Junkins, J. L.: *Analytical Mechanics of Space Systems*, AIAA, 2003, pp. 522.

[45] Dittberner, G., and McKnight, D. S.: Collision Risk in Sun Synchronous Low Earth Orbit, *Advances in Space Research*, **13**, 8(1993), pp. 187–190.

[46] Zhu, X., Zhang, C., Sun, R., Chen, J., and Wan, X.: Orbit Determination for Fuel Station in Multiple SSO Spacecraft Refueling Considering the J2 Perturbation, *Aerospace Science and Technology*, **105**(2020).

[47] Ma, D.-M., and Zhai, S.-Y.: Sun-synchronous Satellite Orbit Determination, *Acta Astronautica*, **54**, 4(2004), pp. 245–251.

[48] Paek, S. W., Balasubramanian, S., Kim, S., and Weck, de O.: Small-Satellite Synthetic Aperture Radar for Continuous Global Biospheric Monitoring: A Review, *Remote Sensing*, **12**, 16(2020).

[49] Vallado, D. A.: *Fundamentals of Astrodynamics and Applications*, Space Technology Library, 2007.

[50] Dorigo, M., Birattari, M., and Stutzle, T.: Ant Colony Optimization, *IEEE computational Intelligence Magazine*, **1**(2006), pp. 28–39.

[51] McGrath, C. N., and Macdonald, M.: General Perturbation Method for Satellite Constellation Reconfiguration Using Low-Thrust Maneuvers, *Journal of Guidance, Control, and Dynamics*, **42**, 8(2019), pp. 1676–1692.

[52] McGrath, C. N., and Macdonald, M.: General Perturbation Method for Satellite Constellation Deployment Using Nodal Precession, *Journal of Guidance, Control, and Dynamics*, **43**, 4(2020), pp. 814–824.

[53] Enright, P. J., and Conway, B. A.: Optimal finite-thrust spacecraft trajectories using collocation and nonlinear programming, *Journal of Guidance, Control, and Dynamics*, **14**, 5(1991), pp. 981–985.

[54] Rao, A. V.: A survey of numerical methods for optimal control, *Advances in the Astronautical Sciences*, **135**(2009).

[55] Imoto, Y., Satoh, S., Obata, T., and Yamada, K.: Optimal Constellation Design for Earth Observation Satellites, Proc. 33rd Int. Symp. Space Technology and Science, 2022.

[56] NASA Technical Memorandum, : *U.S. STANDARD ATMOSPHERE, 1976*, 1976.

[57] McShane, K. A., Monma, C. L., and Shanno, D.: An Implementation of a Primal-Dual Interior Point Method for Linear Programming, *ORSA Journal on Computing*, **1**, 2(1989), pp. 70–83.

[58] Lafontaine, de J., and Hughes, P.: An Analytic Version of Jacchia's 1977 Model Atmosphere, *Celestial Mechanics*, **29**, 1(1983), pp. 3–26.

[59] Kim, C.-K., Lee, J.-S., Chae, J.-S., and Park, S.-O.: A Modified Stripmap SAR Processing for Vector Velocity Compensation Using the Cross-Correlation Estimation Method, *Journal of Electromagnetic Engineering and Science*, **19**, 3(2019), pp. 159–165.

[60] Yamada, K., Asai, T., and Jikuya, I.: Inverse Kinematics in Pyramid-Type Single-Gimbal Control Moment Gyro System, *Journal of Guidance, Control, and Dynamics*, **39**, 8(2017), pp. 1893–1903.

[61] Kiefer, J.: Sequential Minimax Search for a Maximum, *Proceedings of the American Mathematical Society*, **4**, 3(1953), pp. 502–506.

[62] Kasai, S., Kojima, H., and Satoh, M.: Spacecraft attitude maneuver using two single-gimbal control moment gyros, *Acta Astronautica*, **84**(2013), pp. 88–98.

[63] Pereira, F., and Selva, D.: Exploring the Design Space of Lunar GNSS in Frozen Orbit Conditions, 2020 IEEE/ION Position, Location and Navigation Symposium (PLANS), 2020.